Quantum Optics with Cold Atoms — Nonlinear Spectroscopy and Road toward Single-Atom Trap

Thesis by

Zhen Hu

In Partial Fulfillment of the Requirements

for the Degree of

Doctor of Philosophy

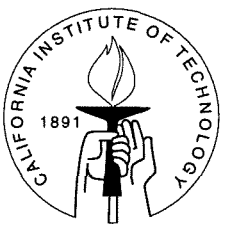

California Institute of Technology

Pasadena, California

1995

(Submitted June 5, 1995)

To my parents

Acknowledgements

First of all, I want to express my deepest gratitude to my advisor, Dr. H. Jeff Kimble, for his constant support, guidance and encouragement during the entire course of this work. Throughout the years that I have worked in his group, I have been a direct beneficiary of his style of involving a student in independent research even in the early stages of graduate studies; and his philosophy that a researcher should be given minimum restriction, but maximum expectation from his advisor. This kind of atmosphere has also nurtured numerous other young scientists, many of whom already play an active role in their field. Among them I want to especially mention Jose W. R. Tabosa and Mike P. Winters, who have provided me with hands-on guidance at early stages of my research. Thanks are also due to Robert J. Thompson, who, in addition to being a great roommate, also introduced me to the field of Quantum Optics. Other members of the Quantum Optics group at Caltech, including Prof. Ken G. Libbrecht and Phil A. Willems, as well as other graduate students and postdocs such as Quentin, Hideo, Nikos, Wolfgang, Jeff, Silvania, and Olivier, have provided useful discussions throughout the course of this thesis work.

This thesis is dedicated to my parents, without their unconditional love and support none of my achievements would be possible. They have introduced me to science and provided all the necessities for me to indulge in the joy of science, which was a luxury during the difficult years when I was growing up. For making my adult life more colorful, I want to thank Jun, whose love is often the motivation behind all the hardships I have endured.

Finally, without mentioning their names, I would like to give credit to all the friends I have made here during my graduate studies, for making Caltech such a wonderful place to live, and so hard to leave. For those among this group who have not yet completed their mission at Caltech, I wish them good luck.

Abstract

Investigations of optical processes for laser cooled and trapped atoms are described. Fluorescence from Cs atoms in a magneto-optical trap is detected under conditions of very low atomic density. Discrete steps are observed in the fluorescent signal versus time and are associated with the arrival and departure of individual trapped atoms. Histograms of the frequency of occurrence of a given level of fluorescence exhibit a series of uniformly spaced peaks that are attributed to the presence of $N = 0, 1, 2$ atoms in the trap.

In addition, numerical absorption and emission spectra for three-level Λ, Ξ, and V systems under intense radiations are calculated. Absorption spectra for a Λ system is used to explain the probe-wave amplification and absorption spectra recorded for Cs atoms cooled and confined in a magneto-optical trap, in which novel spectral features of narrow frequency widths with single-pass gain exceeding 20% are observed. The consequence of the optical gain is demonstrated to lead to negative radiation pressure, which is investigated together with other mechanical forces in the trap. Various alternative trapping schemes in three-level and two-level atoms are proposed as possible means to compress an atomic sample and demonstrated for a two-level magneto-optical trap.

Contents

List of Figures

List of Tables

Chapter 1 General Introduction

The past several years have witnessed a phenomenal pace of achievement in the field of laser cooling and trapping of atoms,[1] with the powerful techniques that have been developed now finding a variety of scientific applications in high-resolution spectroscopy, precision measurement, atomic frequency standards, lithography, as well as in medical and biological sciences. Among the numerous opportunities this technique created, two are of particular interest for the field of Quantum Optics, which are the main constituents of this thesis.

The first of these concerns the capabilities for producing optically dense samples of cold atoms with number densities greater than $10^8/\text{cm}^3$ and temperatures below 100 μK.[1–5] Despite the substantial development in atomic beam technology, where laser beams intersect well-collimated atomic beams in a perpendicular direction and with Doppler broadening (in the longitudinal direction) thus reduced to a minimum, the second-order Doppler broadening (or, time dilation, which is due to the relativistic Doppler effect) and transit broadening (time-of-flight broadening) still hamper spectroscopists in reaching ultra-high resolution. These effects can be eliminated or greatly reduced in an atomic trap because of their small residual thermal velocity (12 cm/s for Cs atoms at 120 μK) and virtually infinite confinement times compared to the transit time of atomic beams.

The second topic concerns the possibility of isolating a single atom that is spatially localized with small kinetic energy. Trapping of a single ion was first reported in 1980.[6] A variety of fundamental phenomena have since then been observed in this system, such as quantum jumps[7], photon anti-bunching[8], and cooling to zero point energy.[9] Beyond this work with ions, single localized molecules have also been studied optically by matrix isolation[10] and by near-field microscopy.[11] But isolation of a single neutral atom has not been, to the best of our knowledge, accomplished before

this work[1] because the interaction of the electromagnetic field with neutral atoms is usually much smaller than that with charged ions. Hence our effort in this thesis to isolate a single atom[13] represents an important extension of the work on single ion and molecule to neutral atom regime.

Although seemingly distant, these two topics are not unrelated. Our focus here is to study quantum phenomena in a sample consisting of only a single atom. This includes excitation of a single atom by non-classical light and producing non-classical states and light sources from the single atom itself. The detailed characterization of a multi-atom trap should prepare us well for this ultimate goal. For example, in the spectroscopic experiment described in this thesis, which employs coherent light to probe a trap containing more than 10^6 atoms,[14] we have found narrow dispersive resonances which are below the natural linewidth of the trapping transition. This suggests that instead of a two-level system, the atoms should be treated as multi-level systems under presence of complex Zeeman splittings and light shifts in the ground and excited states. Of course, such a treatment is also required for a trap containing only one atom. Our subsequent theoretical study of absorption and emission properties of a three-level atom represents an initial attempt to provide such a treatment, albeit in a (maybe over)simplified manner. There has also been a serious attempt in our progress toward a single-atom trap to adopt a multi-level excitation scheme ($6S_{1/2} \rightarrow 6P_{3/2} \rightarrow 8S_{1/2}$ in Cs) in which the wavelength of fluorescence detection [$(8S_{1/2} \rightarrow)7P_{3/2} \rightarrow 6S_{1/2}$] is separated from that of excitation. This approach would overcome the problem associated with the background scattering of the excitation laser which is difficult to eliminate if the same transition is used for both detection and excitation. More closely related to our exploration of non-classical light and single-atom trap, later in this chapter we will see an example involving a three-level atom in a high-finesse optical cavity. This system exhibits a variety of interesting phenomena, (which are decidedly non-classical,) including the possibility to build a "single-atom laser" with sub-Poissonian photon statistics.

[1] At the writing of this thesis, single-atom trap is also reported in cryotraps, see Ref. [12].

Our motivation to study the interaction of non-classical light with a single atom comes from the tremendous progress on both theoretical and experimental fronts in the understanding of the generation and application of non-classical light in recent years. On the experimental front, recent progress in cavity quantum electrodynamics and non-linear optics has made it possible to provide the non-classical light sources for our exploration.[15] For example, in a related research project, a frequency tunable squeezed light with continuous tunability over a range of 2 GHz has been developed and employed for spectroscopic measurements of Cs atoms for sensitivity beyond the vacuum-state limit.[16] In another related program, non-classical light which exhibits both photon antibunching and sub-Poissonian photon statistics has been produced in a beam transmitted through a collection of Cs atoms strongly coupled to a high-finesse optical cavity.[17] Since this is a well collimated Gaussian beam, it is suitable for a variety of spectroscopic experiments. On the theoretical front, research indicates that the properties of fundamental radiative processes of an atom, such as photon statistics and width of fluorescent spectrum, can be altered by coupling to a non-classical field. It is well known that an optical cavity can change the characteristics of atomic radiation by modifying the atoms' external environment, and thus restricting the reservoir modes the atoms emit into. Two examples observed are photon antibunching and normal mode splitting.[17, 18] For an atom in free space, Gardiner has considered the case in which the atom is embedded in a squeezed vacuum. In his landmark paper,[19] Gardiner pointed out that the spontaneous emission from this atom is characterized by *two* transverse decay rates instead of one for ordinary vacuum. They reflect the enhanced and diminished fluctuations of a squeezed state relative to the vacuum field. The resulting sub- and super- natural linewidths have subsequently made ubiquitous appearances in diverse problems of optical physics. There also appear to be exciting possibilities for spectroscopy with other kinds of non-classical fields, although the theoretical literature is not as extensive in this case. For example, Vyas and coworkers[20] have revisited the problem of resonance fluorescence from a single atom where now the atomic excitation is provided by antibunched light (albeit generated from a squeezed source). She showed that both the fluorescence spectrum and photon statis-

tics of the atom are significantly modified in contrast to coherent excitation. The spectrum of the scattered light can be narrower or broader as compared to that of coherent light excitation depending on the bandwidth of the squeezing. Though the fluorescent light still exhibits anti-bunching for short delays, for large delays, however, they can exhibit strong bunching. More generally, one might expect a variety of multiple photon process to be sensitive to the (non-classical) photon statistics of the excitation source.

Of course, all these experimental prospects rely heavily on the strong coupling of the atom to the non-classical field. For example, to observe resonance fluorescence excited by squeezed light, it is essential that the coupling of an atom to the squeezed field dominates that of the atom to the ordinary vacuum. Because the field distribution $\boldsymbol{\Psi}(\mathbf{r})$ for a radiating atomic dipole covers a large fraction of the total 4π steredians solid angle, there is a basic mismatch between $\boldsymbol{\Psi}(\mathbf{r})$ and the well-collimated Gaussian filed $\mathbf{u}(\mathbf{r})$ generated by a typical source of squeezed light. Yet it is precisely the shape $\boldsymbol{\Psi}(\mathbf{r})$ which must be filled with squeezed light converging into the atom if there are to be significant modifications of radiative processes below the vacuum-state limit.[15] One approach to overcome this experimental difficulty is to illuminate the atom by squeezed light in a beam of large numerical aperture. But since this scheme inevitably involves strong focusing of the beam, preferably to the diffraction limit where the waist of the beam is comparable to the wavelength of the laser, the atom needs also to be localized to better than the optical wavelength. Although this "Lamb-Dicke" regime is not likely to be reached in the magneto-optical single-atom trap described in this thesis, it is possible to combine this work with the technique of far-off-resonance trap[21] to achieve a better localization (Section 3.6). Besides this "brute-force" approach, other ways to achieve strong coupling in the atom-field system involve subjecting the atom to a restricted space by placing either a finite (as in the case of optical cavity) or infinite (as in the case of a plane boundary[15]) boundary near the atom.

Apart from the atom as an optical sample to be passively probed by non-classical light, it can also serve as an active media to generate non-classical sources, as for

example, in the construction of a "single-atom laser," which consists of a single atom interacting with a single mode of an optical cavity. While at first glance this may seem to be a beautiful toy from the playground of a quantum optics theorist and just another example of a *gedanken* experiment, such a system does exist in the microwave regime for highly excited Rydberg atoms,[22] and sub-Poissonian photon statistics have been observed in this "single-atom maser." In the optical regime, a series of advances in the area of cavity quantum electrodynamics have propelled us into a domain of strong coupling between a single atom and a single mode of electromagnetic field,[23, 24, 17, 18] but these investigations are hampered by fluctuations in the number of intracavity atoms provided by a conventional atomic beam. To compensate for this shortcoming, our single-atom trap can be modified to overcome the unfavorable geometry associated with the small volume of the optical cavity, either by reducing the number of trapping beams ([25], [26], and Section 2.5) or by "launching" the atom into the cavity via an "atomic fountain" technique.[27]. One recent proposal for realizing the single-atom laser in the optical domain involves a three-level Λ transition in a Cs atom.[28] This laser operates similar in principle to the Raman laser in Rb atoms reported in Ref. [29]. The laser is pumped by the two-photon transition of wavelength 883 nm between the ground state $6S_{1/2}$ and common excited state $6D_{5/2}$. Laser transmission occurs at 918 nm between $6D_{5/2}$ and the other low lying state $6P_{3/2}$. Theoretical study has shown that the intensity fluctuation of this laser should drop well below the shot noise level even for a pump light with Poisson statistics.[30] Of course, this effect can also be observed in multi-atom Raman lasers, but the single-atom laser offers the possibility to generate photon number eigenstates (Fock states) which are the platform for many *gedanken* experiments concerning fundamental concepts of quantum measurement theory. Another beauty of the single-atom laser is that the gain from one atom is enough to build up the laser field, this provides the opportunity to directly observe the switching on and off of the laser when the atom enters and leaves the cavity. Of course, the coupling of the atom to the cavity is again essential in all these discussions, which severely complicates the implementation of the proposed experiment.

In addition to the single-atom laser, there are also opportunities for the study of the quantized motion of the trapped atom itself. From this perspective, the atom is viewed as a mechanical oscillator whose center of mass motion can be approximately described by a damped harmonic oscillator in the trapping potential. In the regime of strong underdamping, the quantized motion in the trap could in principle be resolved, leading to exciting possibilities for manipulating of the atomic dynamics at the level of the wave function for the center of mass motion. A variety of fundamental experiments would then be possible, including the generation of squeezed states for the mechanical oscillator[31, 32] and quantum nondemolition measurements of its motion.[33] For a squeezed state, the uncertainty in position (or momentum) drops below the value set by the zero point fluctuations of the oscillator. While squeezed states have been produced for the electromagnetic field,[34] no such state has been achieved for any other quantized system, including a mechanical oscillator. Indeed, only in the work of Diedrich *et al.*[9] has it been possible to cool a bound mass (in this case, a single Hg ion) to the ground state of the trapping potential (excluding of course molecular systems, where notions of squeezing also apply.) It is also possible to make quantum nondemolition detection (QND) measurements of the oscillator's motion.[33] For example, one might attempt to extract the precise energy eigenstate of the oscillator without disrupting the energy itself but with an unavoidable back-action which perturbs the oscillator's phase. In more general terms, our investigation would be directed toward the synthesis and measurement of novel quantum states for the oscillator's motion. Potential applications of this work would be in measurement science and metrology.

Compared to these attractive future experimental perspectives, what follows is a relatively humble initial attempt which hopefully would serve as a useful preparatory work for future research. As previously stated, this work is part of and closely related to a broad research program aimed at the study of quantum optics in non-classical systems.[15–18, 23, 24, 35, 36] Following the two topics discussed above, this thesis is divided into two principal parts. After introduction to some background information on laser cooling and trapping (Chapter 2), the first part of this thesis (Chapter 3)

deals with the trapping of a single Cs atom. We will show that the discrete steps observed in the fluorescence signal from the trap are associated with the arrival and departure of individual trapped atoms. In the second part (Chapters 4 and 5), we will describe our spectroscopic experiment performed on a sample of Cs atoms contained in a magneto-optical trap. Independent of its connections with our aim to observe non-classical phenomena in single-atom systems, our work on trap spectroscopy has its own importance. For example, the narrow gain identified in the probe spectrum is the basis to construct a "cold-atom laser."[37] Moreover, detailed spectroscopic characterizations of the cold atoms can provide important new information about the dynamics of the trap itself and can suggest new avenues for improved trapping and cooling. The surprising result in the probe absorption spectrum prompted us to develop more complex models for our trap. The simplest such model, based on three-level Λ, Ξ, and V systems, is presented in Chapter 5. The calculation of the three-level absorption and emission spectrum also enables us to study the collective behavior of the trapped atoms, and propose a trapping scheme in which the role of radiation pressure is reversed. And finally, Chapter 6 is a summary for the whole thesis.

Chapter 2 Theoretical and Experimental Background

Laser cooling was first proposed by Hänsch and Schawlow [38] for free atoms and independently by Wineland and Dehmelt[39] for trapped ions. The physical mechanism that underlies these proposals is the Doppler effect, and this kind of laser cooling is often called Doppler cooling, whose theoretical limit for the lowest attainable temperature T_{Doppler} is called the Doppler limit and given by $k_B T_{\text{Doppler}} = \hbar\gamma_\perp$,[40–42] where $2\gamma_\perp$ is the natural linewidth of the transition. Doppler cooling was first demonstrated for trapped ions in 1978.[43, 44] Since then there has been a virtual explosion in the field, beginning with the observation of optical molasses[45] and continuing with magnetic[46] and optical[47] traps for neutral atoms. In 1987 a trap based on the spontaneous light force resulting from the interaction of the atom and near resonant optical field[2] emerged and quickly proved itself to be a powerful and convenient means to cool and trap neutral atoms, especially since the demonstration that such a trap can be realized in a vapor cell using inexpensive laser diodes.[3] Such a magneto-optical trap (MOT)[4, 5] is the instrument for our exploration of nonlinear spectroscopy and isolation of a single atom.

A variety of review articles are available for atomic cooling and trapping.[1] In this chapter, we will first attempt to give a brief overview of the principle of magneto-optical trap (Section 2.1), and then describe the general experimental setup that we employed for our MOT. As mentioned in Chapter 1, the two parts of this thesis describe two different experiments, thus different apparatuses and setups are used. Nevertheless, these two different experiments share a wide range of common ingredients, such as the Ti:sapphire laser (Section 2.2), the technique for laser frequency stabilization (Section 2.3), the anti-Helmholtz coils to generate a quadrupole magnetic field (Section 2.4), and other experimental instruments (Section 2.5). Finally,

at the end of this chapter (Section 2.6), we will give a brief description of the general properties for the atom we used for our experiment, namely the Cs atom, and the reason we choose this particular type of atom.

2.1 Introduction to the Magneto-Optical Trap

We begin by analyzing the force exerted on a two-level atom at rest by a laser beam having intensity I and tuned to an amount Δ below the atomic transition frequency [Fig. 2.1(a)]. It is well known that the absorption or emission of a photon by an atom imparts momentum to the atom. Upon absorption, the atom receives a kick of momentum equal to $\hbar\mathbf{k}$ in the direction of the laser's propagation. Upon emission, there is an additional momentum kick of equal magnitude, but this occurs in a random direction (for spontaneous emission), and so this contribution will average to zero after many scattering events. (But the variance of this contribution, however, does not average to zero and gives rise to the diffusion of the atom discussed below.) The total force on the atom $\mathbf{F}$ will then be $\hbar\mathbf{k}$ times the scattering rate Γ:

$$\mathbf{F} = -\frac{\mathrm{d}\mathbf{p}}{\mathrm{d}t} = \hbar\mathbf{k}\Gamma. \tag{2.1}$$

For a two-level atom having natural linewidth $2\gamma_\perp$, the scattering rate has a maximum of $\gamma_\perp$ for a laser with strong enough intensity such that the atom is highly saturated. However, if the intensity is low ($I \ll I_s$, where I_s is the saturation intensity) and the atom is at rest, the scattering rate has the form [Fig. 2.1(b)]

$$\Gamma = \gamma_\perp \frac{I/I_s}{1 + (\Delta/\gamma_\perp)^2}. \tag{2.2}$$

Next if we consider that the atom is moving with velocity v against the direction of propagation of the laser (which is tuned below the atomic resonance), the atom will see the laser Doppler shifted into resonance, and hence will undergo more scattering events and experience a larger force. Quantitatively, the detuning seen by the atom

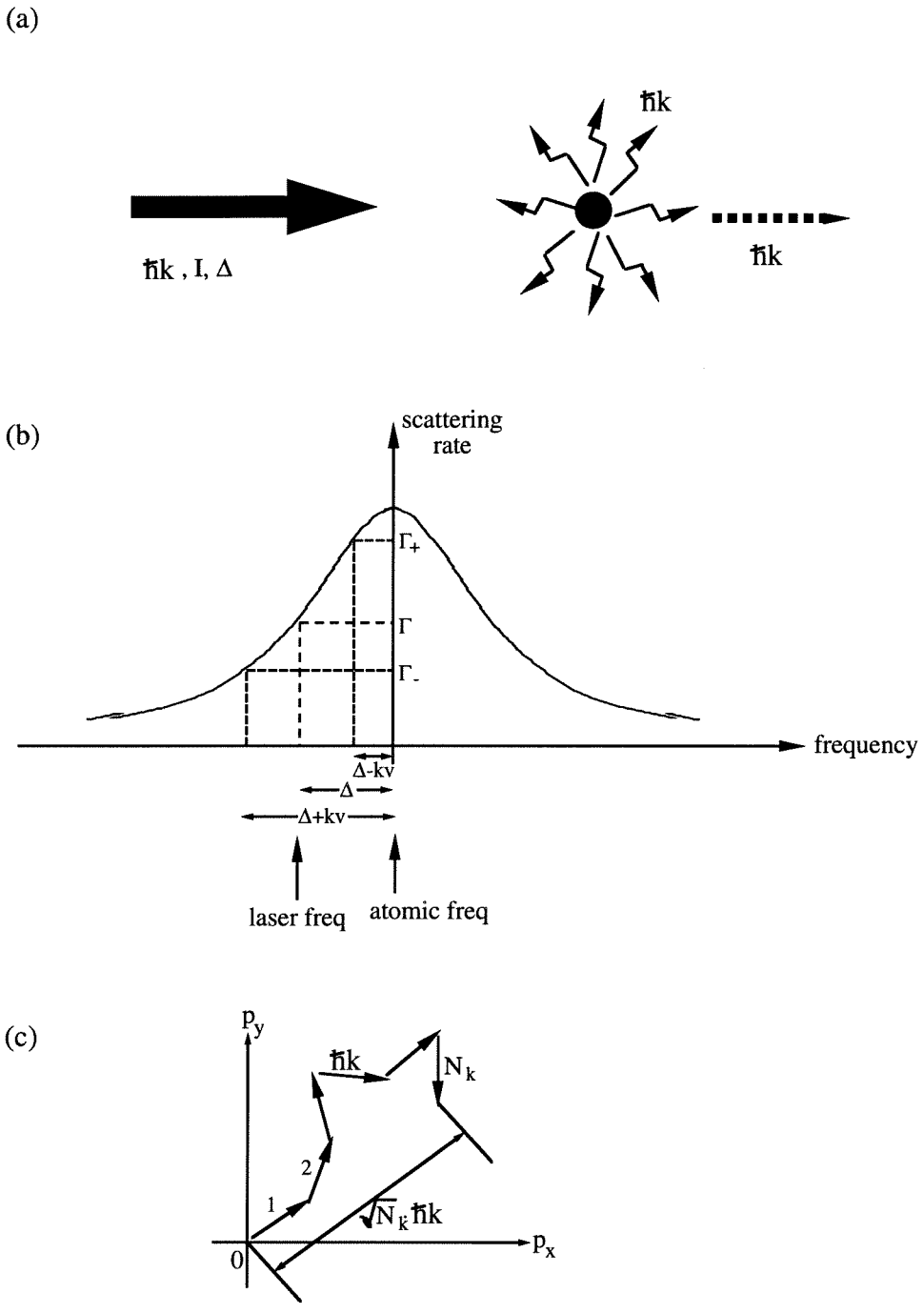

Figure 2.1: Doppler cooling. (a) An atom at rest illuminated by a laser beam having intensity I and detuning Δ. (b) The scattering rate for an atom at rest and a moving atom. (c) The (two-dimensional) random walk in momentum space caused by the spontaneous emission. The text discussed the random walk in one dimension.

is changed to $\Delta - kv$ from Δ, and hence [Fig. 2.1(b)]

$$\Gamma_+ = \gamma_\perp \frac{I/I_s}{1 + \left[(\Delta - kv)/\gamma_\perp\right]^2}. \tag{2.3}$$

Similar arguments hold for an atom moving along the direction of the laser beam, in that case, the detuning seen by the atom is $\Delta + kv$, and

$$\Gamma_- = \gamma_\perp \frac{I/I_s}{1 + \left[(\Delta + kv)/\gamma_\perp\right]^2}. \tag{2.4}$$

If we now consider an atom under the presence of two counter-propagating lasers, each having intensity I and detuning Δ below the atomic resonance, the total force F will then be the sum of the two individual forces along opposite directions, $F = \hbar k(\Gamma_- - \Gamma_+)$. Under the limit of low velocity, i.e., $kv \ll \Delta$, F is a damping force proportional to the velocity, $F = -\alpha v$, with damping coefficient α,

$$\alpha = 4\hbar k^2 \frac{I}{I_s} \frac{\Delta/\gamma_\perp}{\left[1 + (\Delta/\gamma_\perp)^2\right]^2}. \tag{2.5}$$

The rate of cooling is then:

$$\left\langle \frac{dE}{dt} \right\rangle_{\text{cool}} = \mathbf{v} \cdot \mathbf{F} = -\alpha v^2. \tag{2.6}$$

The heating comes from the fluctuations in the damping force whose origin can be traced to the spontaneous emission. We can consider the problem as a random walk in momentum space [Fig. 2.1(c)], with each step corresponding to a single absorption or emission event. Assume our atom started with zero velocity, it is equally likely to absorb a photon from the positive or negative traveling waves. As a result, each absorption represents a step of size $\hbar\mathbf{k}$ in a random walk of the momentum of the atom. In the same way, each spontaneous emission represents another random-walk step, so that each cycle of absorption followed by spontaneous emission represent two random-walk steps. After a time t, the variance in momentum will then be given by the product of the number of steps $N_{\mathbf{k}}$ ($= 2 \cdot 2\Gamma t$, with the first factor of 2 coming from

two random walks associated with a single scattering event; and the second factor of 2 coming from the summation of the two counter-propagating beams) and the square of the step size $(\hbar k)^2$:

$$\langle \mathbf{p}^2 \rangle = 2 \cdot 2\Gamma t \cdot (\hbar k)^2 = 2D_p t \tag{2.7}$$

where D_p is the momentum diffusion constant. Thus, the rate of heating is

$$\left\langle \frac{\mathrm{d}E}{\mathrm{d}t} \right\rangle_{\text{heat}} = \frac{\mathrm{d}}{\mathrm{d}t} \left\langle \frac{p^2}{2m} \right\rangle = \frac{D_p}{m} = \frac{2\Gamma (\hbar k)^2}{m}. \tag{2.8}$$

The minimum temperature is achieved when the cooling rate and heating rate is balanced. From Eq. (2.6) and (2.8), we obtain an expression for the velocity and hence the temperature:

$$\frac{mv^2}{2} = \frac{k_B T}{2} = \frac{D_p}{2\alpha} = \frac{\hbar\gamma_\perp}{4} \frac{1 + (\Delta/\gamma_\perp)^2}{\Delta/\gamma_\perp}. \tag{2.9}$$

This temperature will have a minimum value T_{Doppler} when $\Delta = \gamma_\perp$ and this is called the Doppler temperature:

$$k_B T_{\text{Doppler}} = \hbar\gamma_\perp. \tag{2.10}$$

For Na atom, $T_{\text{Doppler}} = 240\ \mu$K and for Cs atom, $T_{\text{Doppler}} = 120\ \mu$K.

The above arguments can be extended into three dimensions where three sets of counter-propagating laser beams are employed to provide a viscous damping force in all directions. Atom clouds cooled by this technique are called the optical molasses.[45] But Doppler cooling only provides us a method of cooling the atoms, in order to "trap" them, we need a restoring force to keep the atoms within a particular region. A simple yet powerful method for providing this restoring force is to use the Zeeman shift. Such a trap is called a Zeeman-Shift Optical Trap (ZOT) and sometimes also a MOT (Magneto-Optical Trap).

In this trap [Fig. 2.2(a)] a spatially varying magnetic field, usually a quadrupole field with constant gradients along the axes is employed along with three pairs of counter-propagating laser beams with σ^+ and σ^- polarization tuned below the atomic

(a)

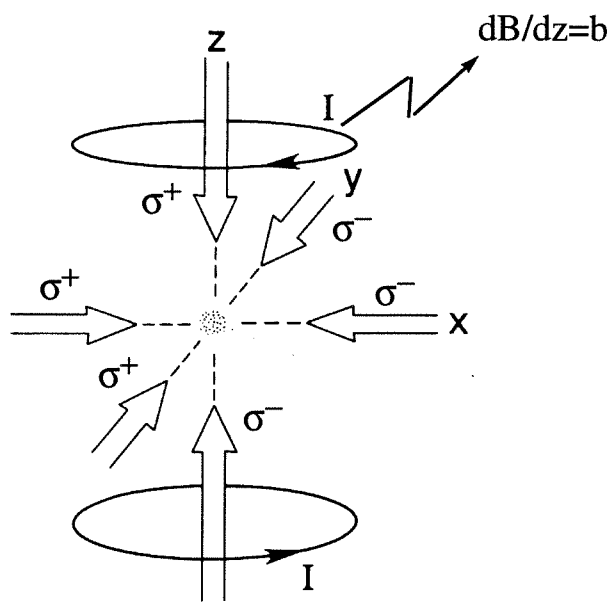

(b)

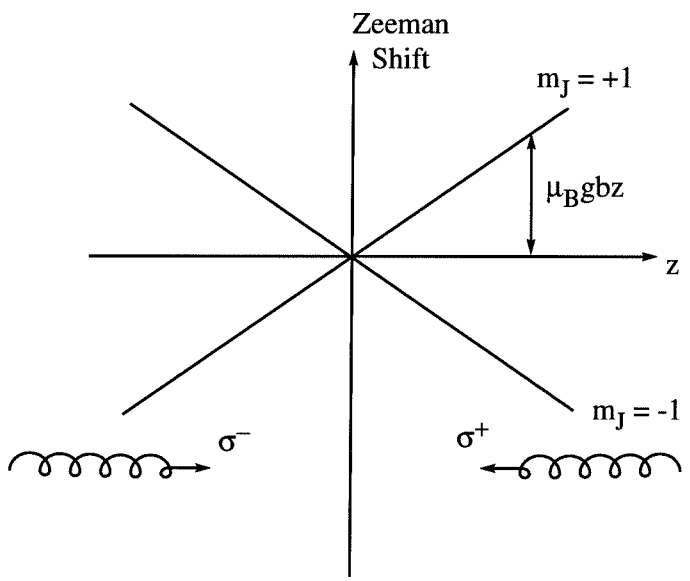

Figure 2.2: The magneto-optical trap. (a) A MOT consists of three pairs of counterpropagating laser beams with σ^+ and σ^- polarization tuned below the atomic resonance frequency. (b) Zeeman shift of a hypothetical one-dimensional atom having total angular momentum $J = 0$ ground state and $J = 1$ excited state, immersed in a magnetic field $B = bz$.

resonance. The restoring force is provided by the spatially varying Zeeman shift, e.g., if we again consider the case of one dimension, in which the magnetic field has the form $B = bz$, an hypothetical atom with total angular momentum $J = 0$ in the ground state and $J = 1$ in the excited state will experience a Zeeman shift $m_J \mu_B g b z$, proportional to its distance z from the center, where $m_J = 0, \pm 1$ is the quantum number for the z component of the excited state angular momentum, μ_B is the Bohr magneton, and g the Lande g-factor. This will nudge the $\Delta m_J = +1$ transition closer to resonance, and the $\Delta m_J = -1$ further away, resulting in a differential absorption of the σ^+ and σ^- beams. Quantitatively, the trapping force is the sum of the forces for the two transition, having different effective detunings $\Delta + \mu_B g b z/\hbar$ and $\Delta - \mu_B g b z/\hbar$, which gives rise to a restoring force $F = -k_z z$ with spring constant k_z:

$$k_z = 4k\mu_B g b \frac{I}{I_s} \frac{\Delta/\gamma_\perp}{\left(1 + (\Delta/\gamma_\perp)^2\right)^2}. \tag{2.11}$$

Combining the cooling and trapping forces, the total force on the atom is then

$$\begin{aligned} F &= -k_z z - \alpha \dot{z} + \text{Langevin Force} \\ &= -m\omega_{\text{trap}}^2 z - m/\tau_{\text{damp}} \dot{z} + \text{Langevin Force}, \end{aligned} \tag{2.12}$$

which is a damped harmonic oscillator with natural frequency ω_{trap}, driven by the Langevin force caused by the diffusive effect of spontaneous emission. We have also defined $\tau_{\text{damp}}^{-1} = \alpha/m$ as the time constant for damping.

For typical experimental conditions, the atom is usually strongly saturated, e.g., $I = 10$ mW/cm^2 $= 10 I_{\text{sat}}$ is typical value of the total trapping intensity. The low intensity limit is thus not satisfied. Nevertheless, the above result can approximately be adapted to take into account the saturation effect. For example, for a trapping laser detuning of $\Delta/2\pi = 5$ MHz and magnetic field gradient $b = 7$ Gs/cm, the natural frequency of the trap ω_{trap} has the value $\omega_{\text{trap}}/2\pi = 300$ Hz, and the damping time constant τ_{damp} has the value $\tau_{\text{damp}}^{-1} = 4.2 \times 10^3$ s^{-1}, making the trap overdamped

since

$$2\omega_{\text{trap}}\tau_{\text{damp}} = 0.9. \tag{2.13}$$

Beyond the Doppler cooling and magneto-optical trapping we have discussed, other cooling and trapping schemes are also employed to manipulate atoms. For example, the theory of polarization gradient cooling[48] was invented to explain some experimental results in which temperatures below the Doppler limit were reached.[49] The new limit for the lowest achievable temperature of this technique approaches the single photon recoil limit: $k_B T_{\text{rec}} = \hbar^2 k^2/2m$, which has a value of 0.1 μK for Cs and 1.2 μK for Na atom. Even temperatures lower than the recoil limit have been achieved in one dimension for Na atoms by using Raman cooling techniques,[50] as well as in three dimensions for spin polarized Hydrogen atoms by employing evaporative cooling and magnetic trapping techniques. In the latter experiment,[51] a density of 8×10^{13} cm^{-3} and a temperature of 100 μK are reported, a factor of 3.5 above the critical temperature of the Bose-Einstein condensation phase transition at this density and well below the 1.3 mK recoil limit for H atom. Microwave traps and acoustic frequency AC magnetic traps are proposed and demonstrated as promising strategies to cross the boundary of the Bose-Einstein condensation limit in both H[52, 53] and Cs[54, 55] atoms.

Even the MOT itself is undergoing dramatic improvements. By using larger laser intensities and 4-cm-diameter beams, it is demonstrated that 3.6×10^{10} Cs atoms can be directly loaded into a MOT, a nearly 300-fold increase in the number of trapped atoms compared to previous researches.[56] A group at MIT have constructed a dark spontaneous-force optical trap ("dark SPOT" trap), in which the atoms are mainly confined in a "dark" hyperfine ground state which does not interact with the trapping light. In such a trap, limitations on the density of the trap due to the excited state collisions[57] and radiation pressure[58] have been overcome and more than 10^{10} Na atoms have been confined to densities approaching 10^{12} atoms/cm^3.[59] Another variation to the usual MOT configuration are traps with less than six trapping beams. For example, Ne atoms are demonstrated to have been trapped in a MOT using only

four laser beams in a tetrahedral configuration, free of standing waves.[25] Even two-beam traps are possible by employing focused Gaussian beams.[26] In our experiment, we sometimes use a five-beam trap to overcome the striation effect[60] due to the standing waves (Section 2.5).

2.2 The Ti:Sapphire Laser

We will now turn to the discussion of the experimental apparatus employed in our laser cooling and trapping experiments.

The laser used in the majority of our experiments is shown in Fig. 2.3. It is based on a Schwartz Electro-Optics Inc. Titan CWBB Ti:sapphire laser[61] pumped by an Argon ion laser (Spectra Physics 2020-05S), and is modified to meet our requirement for frequency stabilization. The heart of the laser is the Ti:sapphire ($Ti:Al_2O_3$) crystal, which has a broad gain curve over a wide range of wavelength regions from red to near IR (700 nm - 1000 nm). This range is covered by three sets of mirrors coated for their respective regions. Within each region, the wavelength can be tuned continuously by rotating the birefringent filter (BRF), e.g., the midband containing 852 nm is continuously tunable from 780 nm to 900 nm. The crystal is cut at Brewster's angle to avoid the reflection losses over a wide tuning range.

The laser can operate both in standing wave and ring configurations by changing the direction of the optical coupler (OC) and the tweeter mirror (TM). When operating in ring configuration, (which is the case for our experiment,) an optical diode (OD) selects the correct circulation direction and the resulting single-frequency beam has a linewidth of > 1 MHz and a drift of ~ 40 MHz/min when free running.

In addition to the above equipment of a standard Titan CWBB, a pair of Brewster plates (BP) and a thick etalon (THKE, free spectral range (FSR) 30 GHz) and a thin etalon (THNE, FSR 100 GHz) are added into the cavity for frequency stabilization. The Brewster plates are mounted on galvanometers and can be swept synchronously to prevent beam-walking. A part of the sweeping signal is fed forward into the thick etalon so that its peak transmission roughly tracks the scanning laser. All these are

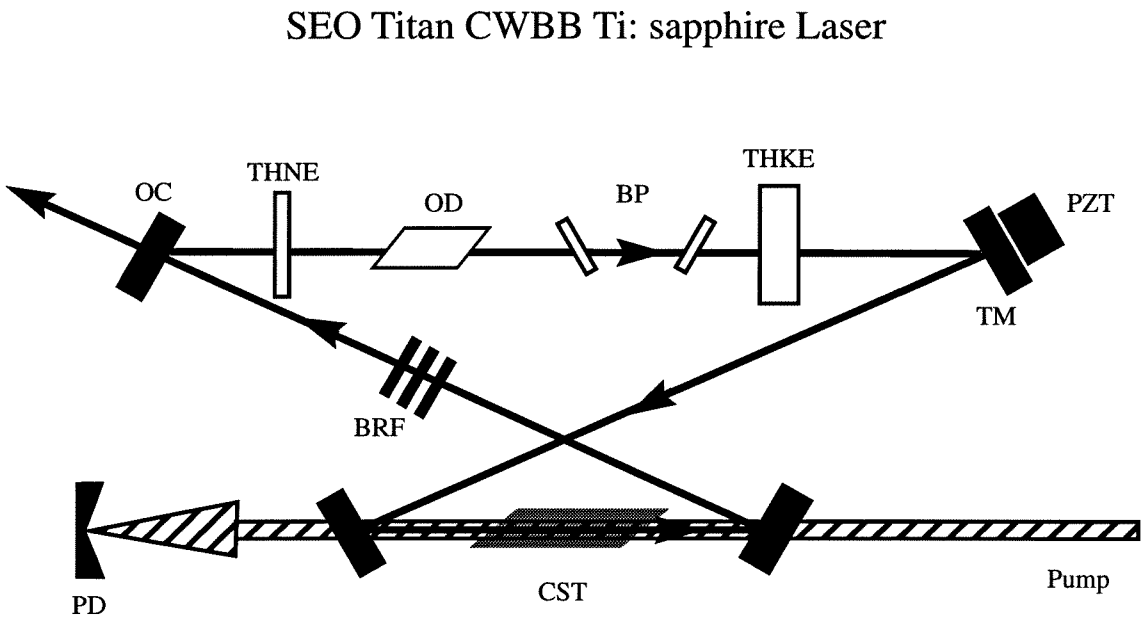

Figure 2.3: Schematic of the Ti:sapphire laser: BP: Brewster plate; BRF: birefringent filter; CST: Ti:Al_2O_3 crystal; OD: optical diode; PD: pump dumper; PZT: piezoelectric transducer; THKE: thick etalon; TNKE: thin etalon; TM: tweeter mirror; Pump: Spectra Physics 2020-05S Ar ion laser.

controlled by a home-made control box containing all the electronics necessary to drive the galvanometers. With these arrangements, the laser is able to scan 3 GHz without mode hopping. The tweeter mirror is mounted on a piezoelectric transducer (PZT) and can be actively locked according to the error signal provided by saturation spectroscopy described in the next section. The entire laser is enclosed within a plexiglass box, which has been covered in lead foam to provide for isolation from external vibration. Because of the large walk-off loss of the thick etalon and other lossy optical components we introduced, the output power dropped from 500 mW to $\sim$ 300 mW at a pump power of 5 W.

2.3 FM Saturation Spectroscopy

The frequency of our laser is locked at a fixed frequency relative to the $6S_{1/2}, F = 4 \rightarrow 6P_{3/2}, F' = 5$ hyperfine transition in Cs by means of FM saturation spectroscopy. Developed in early 1980's, the application of these elegant and powerful spectroscopic techniques to laser frequency stabilization has now become widespread in practice in the field of atomic, molecular, and optical physics and beyond.[62–64]

The schematic of our frequency locking technique is shown in Fig. 2.4. At BS2, a portion of the main laser is split into two beams, hereby referred to as the pump (the transmitted beam) and the probe (the reflected beam) beam.

The probe beam passes through an electro-optic modulator (EOM), whose driving signal at 15 MHz is derived from the output of a function generator (HP 8116A), which is split (Mini Circuit ZDC-10-1 directional coupler) and amplified (ENI Model 403 LA, 37 dB) before finally reaching the desired power level for the EOM. The split portion of the RF signal at the output port of the coupler is later used as a reference for demodulating the detected FM signal. By adjusting the optical axis of a half-wave plate (HW) before the EOM, the polarization of the probe beam can be aligned along the optical axis of the EOM crystal to eliminate undesired amplitude modulation. The output light, which is a phase-modulated beam having FM sidebands symmetrically placed about the carrier, is subsequently passed through a Cs cell and focused onto

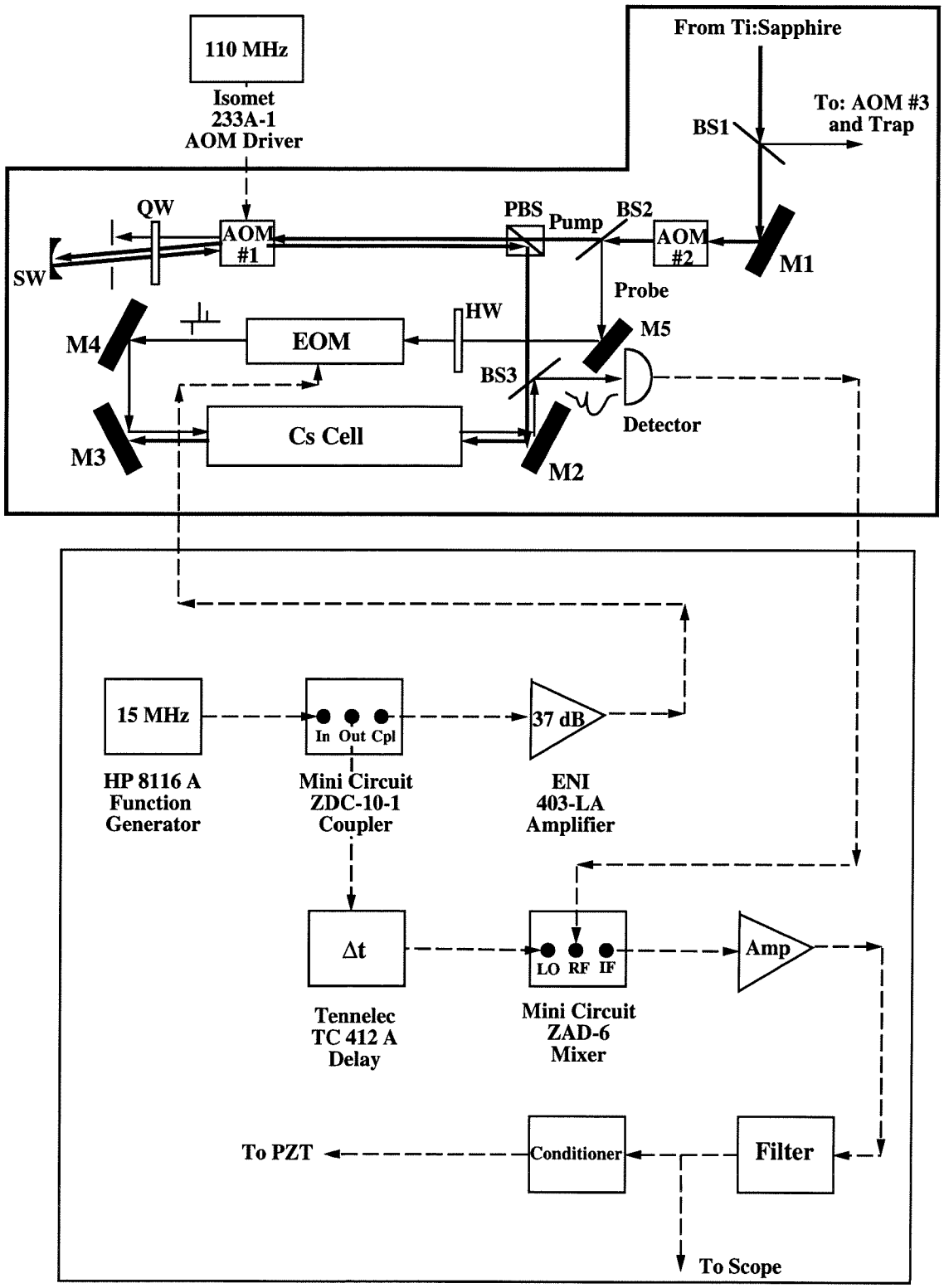

Figure 2.4: FM saturation spectroscopy schematic. The upper box denotes optical components, while the lower box shows electronic configurations. See text for description.

a fast photodiode.

If there were no absorptive medium (like the Cs cell) in the path of the probe beam, the output of the photodiode would be a DC level since the sidebands are exactly π radians out of phase for pure phase modulation and the beat notes they produce with the carrier exactly cancel. However, due to the absorption and dispersion of the Cs atoms in the beam path, the two sidebands are attenuated differently near a resonant transition, and such an exact cancellation disappears, producing a net signal at the sideband frequency (15 MHz). If we demodulate this signal using suitably delayed reference to look at the quadrature phase, we will obtain dispersive lineshape suitable for use as an error signal. This is the principle behind FM spectroscopy.[62, 63]

Next consider the transmitted beam from BS2. It is double passed through an acousto-optic modulator (AOM #1, Isomet 1206C-1) whose single pass frequency shift ω_{AOM1} is near the center frequency 110 MHz of the RF driver (Isomet 233A-1). The doubly-shifted output beam emerges from the reflection of the polarizing beamsplitter (PBS), and has a power of roughly 50% of the input beam and frequency $2\omega_{\text{AOM1}}$ below the probe beam for down-shifted beam. Note that the incident beam has "p" polarization and passes through the PBS, while the output beam, whose polarization is rotated by the quarter-wave plate (QW) after retroreflected by the spherical mirror SM, has "s" polarization and is reflected by the PBS. This arrangement enhances the overall efficiency by eliminating the loss of the beamsplitter. The pump beam is further bounced off mirror M2 and enters the Cs cell, where it overlaps with the probe beam, but propagates in the opposite direction.

The saturation spectroscopy is a technique for obtaining Doppler-free resolution using the phenomenon of "spectral hole burning" caused by the strong pump beam. Without the pump beam, as we scan the laser, the photodetector will simply record a Doppler profile probed by the probe beam. The effect of the pump beam is to saturate those atoms with velocity v towards the pump such that

$$\omega_{\text{pump}} + kv = \omega_{4\to F'}, \tag{2.14}$$

where $F' = 3, 4, 5$, and $\omega_{4\to F'}$ is the resonant frequency for the hyperfine transition $F = 4 \to F' = 3, 4, 5$ (Refer to Fig. 2.5(a) for the Cs D_2 line), so that there is a minimum in absorption for these atoms. If the probe frequency seen by these atoms $(\omega_{\text{probe}} - kv)$ coincides with the same or a different hyperfine transition, i.e.,

$$\omega_{\text{probe}} - kv = \omega_{4\to F''}, \tag{2.15}$$

a dip (hole) will be superimposed on the broad Doppler profile.

Combining Eqs. (2.14) and (2.15), and using the relationship $\omega_{\text{pump}} = \omega_{\text{probe}} - 2\omega_{\text{AOM1}}$ for down-shifted pump beam, we get,

$$\omega_{\text{probe}} = \omega_{\text{AOM1}} + \frac{\omega_{4\to F'} + \omega_{4\to F''}}{2}. \tag{2.16}$$

So there are a total of six resonances, three of which for $F' = F''$, corresponding to pump and probe resonant with the same hyperfine transition and three of which for crossover resonances, where $F' \neq F''$, and pump and probe resonant with different hyperfine transitions.

The fast output of the photodiode, containing information about the saturated Doppler profile and FM sideband spectroscopy of the probe beam, is sent to the RF input of a mixer (Mini Circuit ZAD-6), whose LO input comes from the split portion of the RF signal for driving the EOM, passed through a variable delay (Tennelec TC412A). The error signal shown in Fig. 2.5(b) is obtained by amplifying and filtering the demodulated signal at the IF output of the mixer, where only narrow hyperfine and crossover resonances are left over because of the demodulation. The error signal is further sent through a conditioner to the piezoelectric transducer (PZT) driving the tweeter mirror in the laser cavity, completing the servo loop. The result of this stabilization scheme is a laser linewidth of less than 100 KHz.

Throughout the course of our experiment, to meet different requirements such as to switch or sweep the frequency of the trapping laser, we have used different configurations to lock our laser to different detunings from the $F = 4 \to F' = 5$

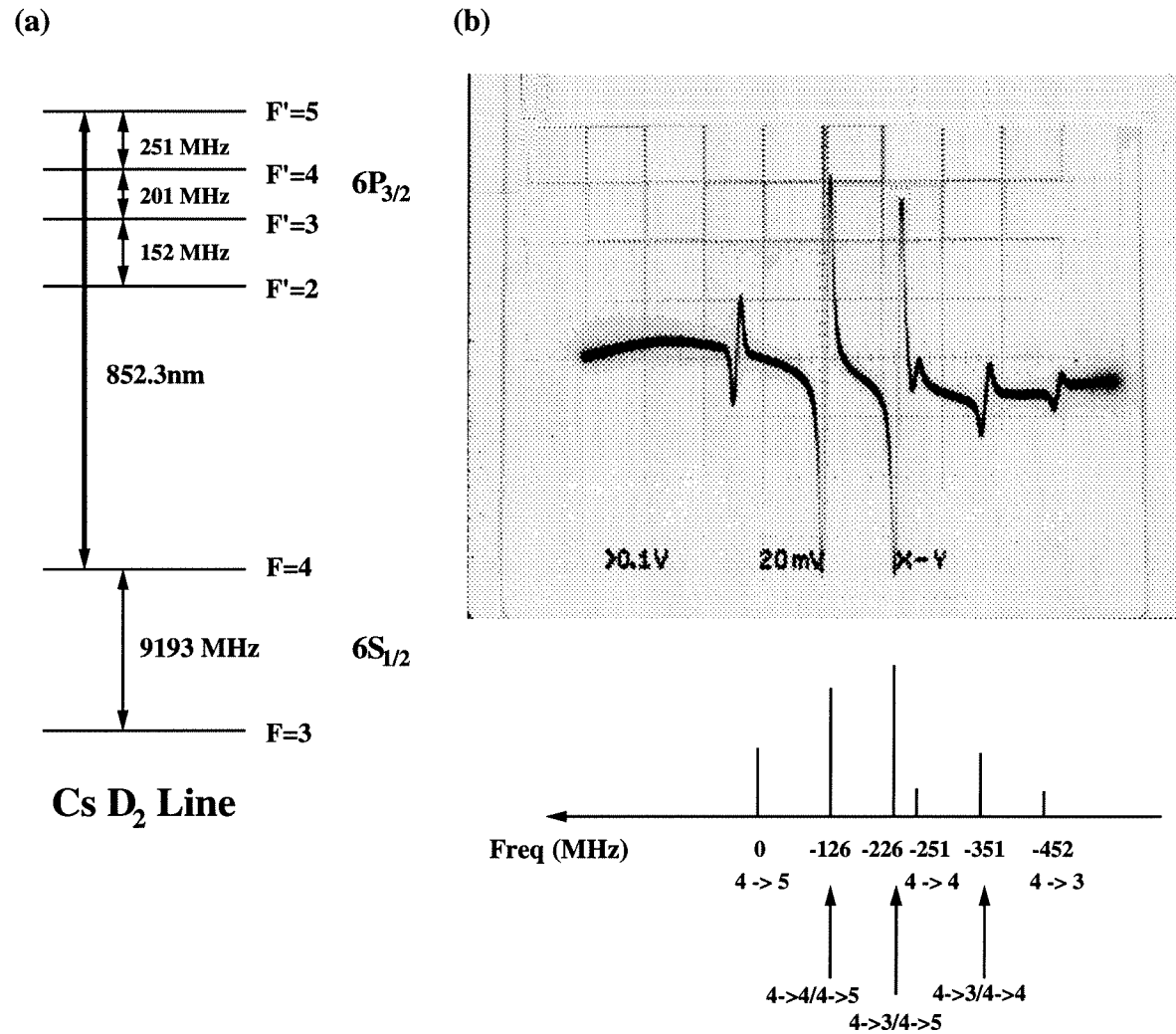

Figure 2.5: The error signal for saturation spectroscopy. (a) The Cs D_2 line. (b) The error signal of saturation spectroscopy on D_2 line. A total of six resonances, three corresponding to the hyperfine transition $F = 4 \rightarrow F' = 3, 4, 5$, and three corresponding to the crossover resonances, are evident.

No	Description of Experiment	AOM #1 ω_{AOM1}(MHz) -2 order	AOM #2 ω_{AOM2}(MHz) $+1$ order	Lock Freq ω_{Lock} (MHz)	Laser Frequency ω_{Laser}(MHz) $(\omega_{\mathrm{Lock}} + \omega_{\mathrm{AOM1}} - \omega_{\mathrm{AOM2}})$
1	single atom/ spectroscopy for switching	110	110	-226 $4 \rightarrow 3/4 \rightarrow 5$	-226
2	spectroscopy prototype #1	not used	not used	-226 $4 \rightarrow 3/4 \rightarrow 5$	-226
3	single atom prototype #1	101	not used	0 $4 \rightarrow 5$	$+101$
4	spectroscopy prototype #2	110	not used	-226 $4 \rightarrow 3/4 \rightarrow 5$	-116
5	Ref. [65]/ spectroscopy prototype #3	$126 - \delta$	not used	-126 $4 \rightarrow 3/4 \rightarrow 4$	$-\delta$

Table 2.1: Locking schemes used in various experiments. The lasers are further shifted by AOM #3 (not shown) to reach the desired frequency before finally used for trapping.

transition, sometimes introducing additional AOMs to offset the laser frequency. For example, in our single-atom experiment, two extra AOMs are used, one in the arm for frequency stabilization (AOM #2 in Fig. 2.4) and another in the arm for trapping (AOM #3 in Fig. 3.8). These configurations are documented in Table 2.1. Note that the laser frequency ω_{Laser} is usually further shifted (or double-shifted) by AOM #3 in the trapping beam path to meet the frequency requirements for various experiments.

2.4 The Magnetic Field Gradient

The magnetic field gradient is provided by the quadrupole field generated by a pair of anti-Helmholtz coils carrying opposite electric currents. Calculating the magnetic field distribution for a particular current configuration is the subject of magnetostatics, an ancient topic which has found widespread application in magnetic confinement of plasmas and neutron traps. Recently the field has received renewed interest primarily

due to the possibility of magnetostatic trapping of neutral atoms. For example, more exotic configurations, such as the spherical hexapole field and the "baseball" field, are studied in Ref. [66].

To begin with, we derive the expression for the magnetic field B along the axis z of two coils carrying a single turn of current I and having equal radius R, located at $z = \pm A$, respectively (Fig. 2.6). The integration of Biot-Savart's law gives:

$$B_z(z, \rho = 0) = \frac{\mu_0 I R^2}{2} \left\{ \frac{1}{\left[(A-z)^2 + R^2\right]^{3/2}} - \frac{1}{\left[(A+z)^2 + R^2\right]^{3/2}} \right\}, \quad (2.17)$$

$$B_\rho(z, \rho = 0) = 0. \quad (2.18)$$

This is a field along the z axis which vanishes at the origin ($B_z(0) = 0$). Near the center ($z \ll A$), it can be expanded into polynomial series of z,

$$B_z(z) = bz + cz^3 + \cdots, \quad (2.19)$$

where

$$b = \frac{\mu_0 I R^2}{2} \frac{6A}{(A^2 + R^2)^{5/2}}, \quad (2.20)$$

$$c = \frac{5(4A^2 - 3R^2)}{6(A^2 + R^2)^2} b, \quad (2.21)$$

and all z^{2n} terms vanish because $B_z(z)$ is an odd function of z.

From Eq. (2.21) we see that the optimum geometry for the most homogeneous gradient near the center is $A = 0.87R$, so that the cubic term cz^3 also vanishes. In our experiments we have used two sets of coils, one for the glass cell (used for the spectroscopic experiment), where $A = R = 1.8$ cm; and one for the stainless steel chamber (used in the single-atom experiment), where $A = 3.2$ cm and $R = 8.4$ cm. For both coils, the cubic term is negligible compared to the linear term, e.g., for our spectroscopic coils, $(cz^3)/(bz) = 2.5 \times 10^{-3}$ at $z = 1$ mm, approximately the size of the trap.

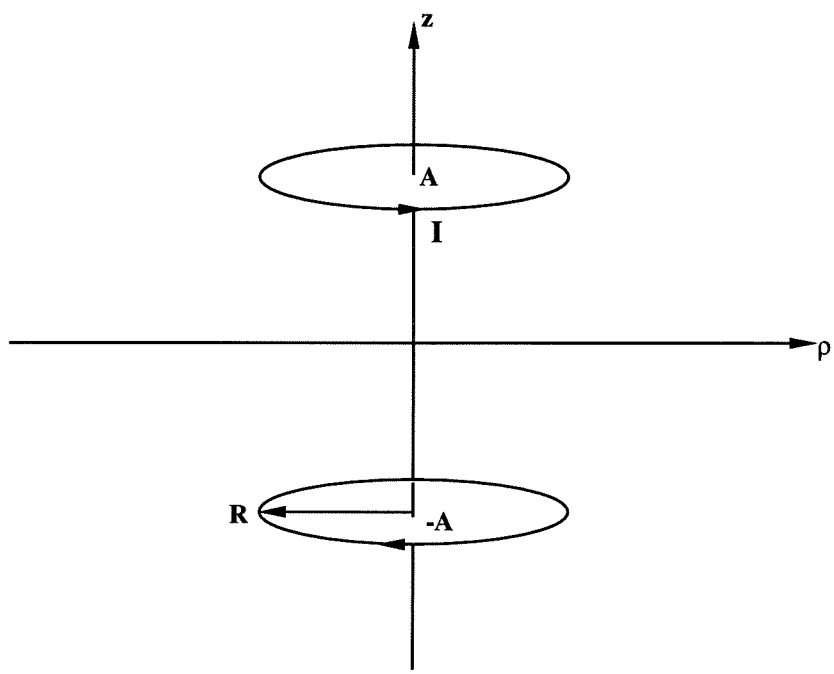

Figure 2.6: Anti-Helmholtz coils consisting of a pair of coils with radius R carrying current I in opposite directions located at $z = \pm A$.

Because of symmetry, the field in the plane $z = 0$ only has transverse components B_x and B_y. Furthermore, the gradient of these components near the origin should be related to $\partial B_z/\partial z = b$ by the Gauss's law for magnetic field, $\nabla \cdot \mathbf{B} = 0$, i.e.,

$$\frac{\partial B_x}{\partial x} = \frac{\partial B_y}{\partial y} = -\frac{1}{2}\frac{\partial B_z}{\partial z} = -\frac{1}{2}b. \tag{2.22}$$

Therefore, the magnetic field of the anti-Helmholtz coil is zero at the center and arises linearly from that point, twice as fast in the z direction than in the x and y direction.

To obtain a numerical value for the field gradient, we must take into account that any practical coil consists of many turns of currents, e.g., our coil for single-atom experiment has six layers, each consisting of twenty turns of 20 AWG wires carrying 4 A of currents. After summing over the contribution of all 120 turns of currents, we get the result $b = 7$ G/cm for our single-atom coil and $b = 10$ G/cm for our spectroscopic coil having 13 turns of wires carrying a current of 4 A. This is not significantly different than calculated from Eq. (2.20) replacing I with NI, where N is the total number of turns.

The resistance of the coils, while readily calculated from the conductivity of the particular wire chosen, is easier measured by digital multimeters. For example, for our single-atom coil, the resistance is about 2.5 Ω each. This implies a total power dissipation of 80 W at 4 A current. The heat generated this way typically raises the surface temperature of the vacuum chamber 30 - 40 °C above room temperature and is sometimes used to bake our chamber. The inductance of the coil can also be measured by a L-C-R meter, and the result is $L = 0.8$ mH for our single-atom coil. The L-R time constant for a single coil is thus 0.3 ms.

We will now turn to a related problem of designing a pair of Helmholtz coils carrying current in the same direction to balance the residual magnetic field. By flipping a sign in Eq. (2.17), one can get the polynomial expansion for the field of Helmholtz coils at the origin,

$$B_z = B_0 + az^2 + \cdots, \tag{2.23}$$

where

$$B_0 = \frac{\mu_0 I R^2}{(R^2 + A^2)^{3/2}}, \tag{2.24}$$

$$a = \frac{3(4A^2 - R^2)}{2(R^2 + A^2)^2} B. \tag{2.25}$$

For optimum uniformity, the spacing of the coils must be equal to the radius, $R = 2A$. But again for trap size of 1 mm the nonuniformity is usually negligible. The Helmholtz coils are only used in the single-atom experiment, where the magnetic field zero is crucial for a well-aligned trap. Two types of coils are used for the z (the big coils) and x, y axis (the small coils). The big coils have $R = 8$ cm and $A = 5$ cm, with 12 turns of wires, thus $B_0 = 1.1$ G/A. For the small coils, $R = 4$ cm, $A = 9.5$ cm, with 20 turns of wires, we have $B_0 = 0.37$ G/A.

The coils are mounted conveniently on the flanges for the vacuum windows and driven by a home-made current source having three outputs able to sink a maximum current of 2 A each. By adjusting the trimpots on the front panel of the current source box, the currents can be varied individually until the earth's magnetic field and other stray fields at the center of the vacuum chamber, measured by a Hall-effect gaussmeter (Bell 640), are canceled by the field generated by the Helmholtz coils. The residual magnetic field, within 1 cm of the center of the chamber, is less than 10 mG.

2.5 Other Experimental Instruments

Besides the magnetic field coils, the laser, and its locking schemes, another important part of the experimental apparatus is the vacuum vessel, so important that we later devote a whole section (Section 3.3.3) to this topic. Other instruments include the beam expanding optics, the repumping laser and the beam splitting optics.

The beam expanding optics are relatively simple: Two convex lenses with focal length f_1 and f_2 are arranged in a telescope configuration where the focus of one lens

overlaps with the focus of another. The waist of the output beam is then a factor f_2/f_1 larger than that of the input beam. For example, in our single-atom experiment a $10\times$ beam expansion is achieved by using lenses of $f_1 = 3.8$ cm (L2 in Fig. 3.8, Newport KPX 079) and $f_2 = 40.0$ cm (L3 in Fig. 3.8, KPX 115). Sometimes a pinhole is placed at the common focal point to spatially filter the beam.

The purpose of the repumping laser is to recirculate population lost to $6S_{1/2}, F = 3$ back to $F = 4$. This is accomplished by an independent semiconductor laser diode tuned to the transition $6S_{1/2}, F = 3 \rightarrow 6P_{3/2}, F' = 2, 3, 4$ by regulating the temperature of the laser head. Later it is replaced by an external-cavity diode laser[67] capable of saturation locking to the $6S_{1/2}, F = 3 \rightarrow 6P_{3/2}, F' = 4$ hyperfine transition, as described in Section 2.3.

The rest of the optics is for splitting the laser into five or six beams and converting it into σ^+ and σ^- polarizations. As from our own experience and numerous documented and undocumented anecdotes, the trap will sometimes develop patterns of alternating bright and dark lines in its image. The detail of the pattern and its periodicity depend on the alignment. Typically between one and ten such striations are observable across the trap. Ref. [60] attributes this "channeling" effect to the interference pattern of optical standing waves. The large length scale (hundreds of wavelengths) is due to the slight angle α of the two counterpropagating lasers when the two beams are not exactly antiparallel to each other. Such a misalignment will give rise to a length scale of λ/α which could be much larger than the wavelength λ itself. To avoid such effects, we have developed a five beam trap in which only one standing wave is present in the z direction. In the x-y plane, three beams are used, two along the x and y axis, the other (v-beam) intercepts the x and y axis with 45° (Refer to Fig. 3.8). Our experience confirms that this arrangement indeed helps to reduce the striation effect. A complete solution would perhaps require eliminating the standing waves all together, like the 4-beam tetrahedron trap described in Ref. [25]. But such a trap is difficult to realize in our vacuum chamber because of the unfavorable geometry.

The complete setups for our different experiments are shown in Fig. 3.8 for the

single-atom experiment and Fig. 4.1 for the spectroscopy experiment and are discussed when this work is described in detail.

2.6 The Properties of Cs Atoms

Although we have used different setups for two different experiments, only one type of interaction medium is used, i.e., the Cs atom. Before the invention of Ti:sapphire laser, Na was widely used in atomic physics experiments because it is within the tuning range of the dye laser. But with the introduction and commercialization of solid-state lasers and semiconductor diode lasers, more and more laboratories have shifted to Cs atoms because its D_2 line at 852 nm is conveniently accessible by Ti:sapphire lasers or GaAlAs laser diodes. These sources are replacing the dye lasers because of their stability and user-friendliness.

The Cs atom is the heaviest non-radioactive alkali element. Alkali atoms (mainly Li, Na, and Cs) are used in atomic physics experiment because they have only one single electron in their outermost shell. Such a simple electronic configuration is easy to handle both theoretically and experimentally. The ground state hyperfine splitting of 9.1 GHz of the Cs atom is the most precisely measured frequency and is used in atomic clock for time standard. Some relevant properties of Cs atom are listed below:

- atomic weight $A = 133$, atomic number $Z = 55$.
- ground state configuration $6\,^2S_{1/2}$, nuclear isospin $I = 7/2$.
- energy level diagram, see Fig. 2.7.
- melting point, 28 °C (at 1 atm); boiling point, 669 °C (at 1 atm).
- vapor pressure, see Fig. 3.6.
- natural linewidth for D_2 line, $2\gamma_\perp/2\pi = 5$ MHz; excited state lifetime, $1/2\gamma_\perp = 32$ ns.

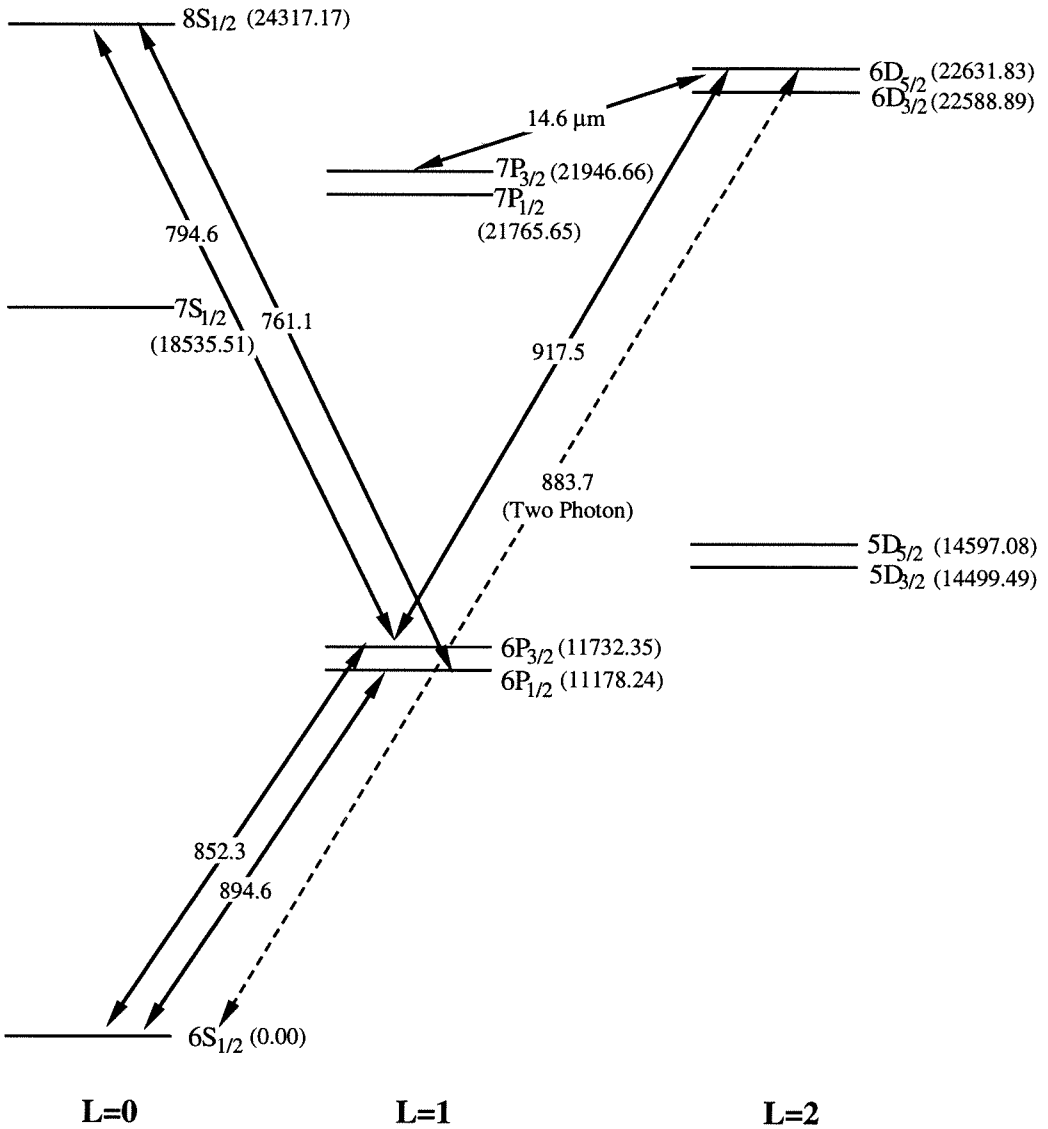

Figure 2.7: Cs energy level diagram relevant to this thesis, after Ref. [68]. The energy levels (in parenthesis) are in cm^{-1}, and the wavelengths of the transitions are in nm, unless otherwise indicated.

- Doppler limit $T_{\text{Doppler}} = \hbar\gamma_\perp/k_B = 120\ \mu$K; recoil limit $T_{\text{rec}} = \hbar^2k^2/2mk_B = 0.1\ \mu$K.

- thermal velocity at 300 °K, $v_{\text{Th}} = (2k_BT/m)^{1/2} = 194$ m/s; thermal velocity at Doppler limit $v_{\text{Doppler}} = (2\hbar\gamma_\perp/m)^{1/2} = 12$ cm/s; thermal velocity at recoil limit $v_{\text{rec}} = \hbar k/m = 3.5$ mm/s; thermal velocity to Doppler shift a natural linewidth of D_2 line $v_{\text{lw}} = \gamma_\perp\lambda/\pi = 4.3$ m/s.

- photon scattering rate $\Gamma = \gamma_\perp(I/I_s)/(1 + I/I_s + (\Delta/\gamma_\perp)^2)$.

- saturation intensity for $6S_{1/2}, F = 4, m_F = 4 \rightarrow 6P_{3/2}, F' = 5, m_{F'} = 5$, $I_s = 1$ mW/cm^2.

- Clebsch-Gordon coefficients for D_2 transition, see Fig. 3.4.

- ground state hyperfine transition frequency $(6S_{1/2}, F = 3 \leftrightarrow 6S_{1/2}, F' = 4)$, 9, 192, 631, 770 Hz.

Chapter 3 Trapping of a Single Atom

3.1 Introduction

In this chapter, we will turn to the topic of constructing and observing the fluorescence from a magneto-optical trap containing only a single atom. The fluctuations of the number of atoms in the trap n_{ss} obey Poisson statistics, $\sigma_{n_{ss}} = 1/\sqrt{n_{ss}}$. The fluorescence count from the trapped atoms C_{trap} is the product of n_{ss} and the fluorescence from an individual atom N_1, which is also a Poisson variable. Then, the square of the relative variance of C_{trap} should be the sum of the square of the relative variance $\sigma_{n_{ss}}/n_{ss}$ and σ_{N_1}/N_1:

$$\left(\frac{\sigma_{C_{\text{trap}}}}{C_{\text{trap}}}\right)^2 = \left(\frac{\sigma_{n_{ss}}}{n_{ss}}\right)^2 + \left(\frac{\sigma_{N_1}}{N_1}\right)^2. \tag{3.1}$$

In a normal trap, which typically contains more than 10^6 atoms, the relative variance of n_{ss} is negligible compared to the relative variance in N_1 ($\sigma_{n_{ss}}/n_{ss} \ll \sigma_{N_1}/N_1$), and the relative variance of C_{trap} is primarily due to the fluctuation in N_1:

$$\frac{\sigma_{C_{\text{trap}}}}{C_{\text{trap}}} = \frac{\sigma_{N_1}}{N_1} = \frac{1}{\sqrt{N_1}}, \qquad \text{for } n_{ss} \gg N_1, \tag{3.2}$$

which is a constant independent of the number of atoms n_{ss}. If, on the other hand, we enter the regime $n_{ss} \ll N_1$, then the relative variance in C_{trap} will mainly come from $\sigma_{n_{ss}}$,

$$\frac{\sigma_{C_{\text{trap}}}}{C_{\text{trap}}} = \frac{\sigma_{n_{ss}}}{n_{ss}} = \frac{1}{\sqrt{n_{ss}}} = \sqrt{\frac{N_1}{C_{\text{trap}}}}, \qquad \text{for } n_{ss} \ll N_1, \tag{3.3}$$

which is proportional to $1/\sqrt{C_{\text{trap}}}$ as we vary the number of atoms in the trap. Next if the number of the atoms in the trap n_{ss} is further decreased, the fluctuation in n_{ss} becomes so large that discrete steps of equal magnitude, associated with the random arrival and departure of individual trapped atom, are observable [Fig. 3.1(a)]. And

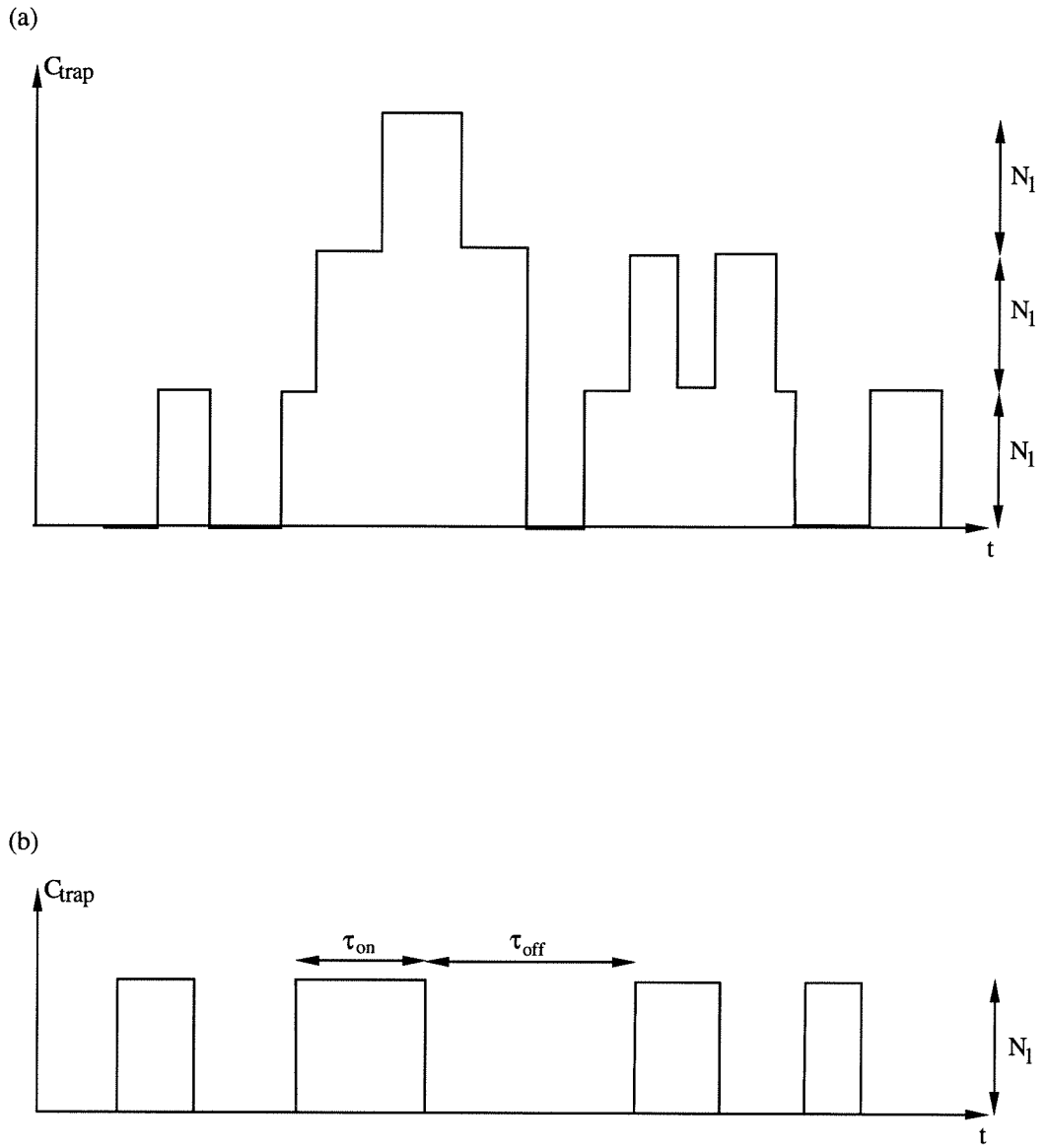

Figure 3.1: The fluorescent light from a trap containing (a) only a few atoms (b) a single atom. The jumps in fluorescent light are due to the atoms entering and leaving the trap. In theses figures, the fluorescence from a single atom N_1 is assumed to be constant without fluctuations.

finally, when the single-atom trapping condition is reached, the fluorescence from the trap will look much like those shown in Fig. 3.1(b), in which the signal jumps to the level N_1 for a time period τ_{on} (the "on" state), and then falls back to zero (the "off" state) and remains there for a time period τ_{off} before jumping up again. This kind of behavior, similar to the "quantum jumps" described in Ref. [69], is a signature for systems containing only one quantum and provides us a means to detect and confirm the trapping of a single atom.

Compared to the detection, the construction of the single-atom trap itself is relatively straightforward. Beginning with a MOT containing about $10^6 - 10^7$ atoms, our approach for reducing the number of atoms n_{ss} is to directly adjust the experimental parameters that would affect n_{ss}, until the condition for single-atom trapping is reached. In practice, however, such an adjustment sometimes means a change in experimental setup or an upgrade in experimental apparatus. And the final condition for single-atom trapping is only reached after many trials and errors.

Following this strategy, the organization of this chapter is as follows. In Section 3.2 we will describe the simple theoretical model that guides us in the design of the experiment. This includes simple rate equations for the number of atoms in the trap n_{ss}, the distribution and duration of the on- and off- times (τ_{on} and τ_{off}) for the fluorescence jumps, and the actual magnitude of the jumps N_1. All these parameters are already introduced previously in this section. In Section 3.3 we will discuss, step by step, the implication of this model to the design of the experiment. We will attempt to justify our choice of the particular experimental apparatus based on a compromise between the available technology and funding, and will also outline possible future improvements based on the performance of such a design in the actual experiment. Section 3.4 contains a brief description of the experiment, whose results are discussed in Section 3.5. The applications of our single-atom trap to quantum optics research and other future developments to this end are discussed in Section 3.6.

3.2 Theoretical Model

The number of atoms contained in the trap is determined by the balance between two competing rates: the capture rate into the trap and the loss rate from the trap. The loss rate L is primarily due to the collisions of trapped Cs atoms with atoms in the background Cs as well as other gas vapors and can be thus taken as:

$$L = (n_{\mathrm{BG}} + n_{\mathrm{Cs}})\sigma u, \tag{3.4}$$

where n_{BG} is the density for the residual background gas and n_{Cs} is the density for background Cs vapor; σ is the average cross section for an atom in the trap to be ejected by a collision, and u is the approximate thermal velocity appropriate to the collision.

Likewise, the capture rate R can also be derived from simple statistical mechanics: assuming that any atom entering the volume enclosed by the trapping laser beams with velocity v below a certain capture velocity v_c is slowed and eventually trapped (Fig. 3.2), the capture rate can then be determined by the integral:

$$R = n_{\mathrm{Cs}} A \int_{v=0}^{v_c} \int_{\theta=0}^{\pi/2} \int_{\phi=0}^{2\pi} (v\cos\theta) f(v)\, dv \frac{d\Omega}{4\pi}, \tag{3.5}$$

where

$$f(v) = 4\pi \left(\frac{m}{2\pi k_B T}\right)^{3/2} v^2 \exp\left(-mv^2/2k_B T\right) \tag{3.6}$$

is the Maxwell-Boltzmann distribution for Cs atoms with atomic mass m at temperature T, and A is the effective total area presented by the trapping laser beams to the atomic flux, which we simply take as $A = 6 \times \pi d^2/4$ for six laser beams with uniform circular cross section of diameter d. In the limit where the capture velocity v_c is much less compared to the thermal velocity $v_{\mathrm{Th}} = (2k_B T/m)^{3/2}$, (a fact we shall prove later in Section 3.3.3), the integral takes a simple form:

$$R = \frac{1}{4} n_{\mathrm{Cs}} v_{\mathrm{Th}} \frac{1}{\sqrt{\pi}} \left(\frac{v_c}{v_{\mathrm{Th}}}\right)^4 \left(\frac{3}{2}\pi d^2\right), \tag{3.7}$$

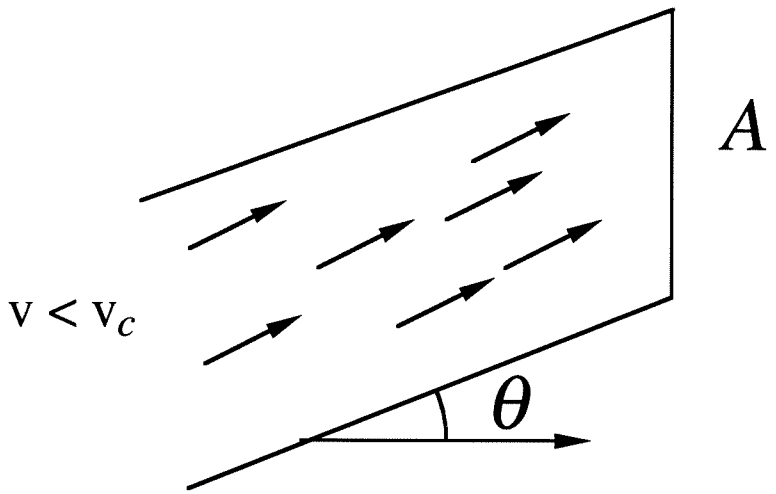

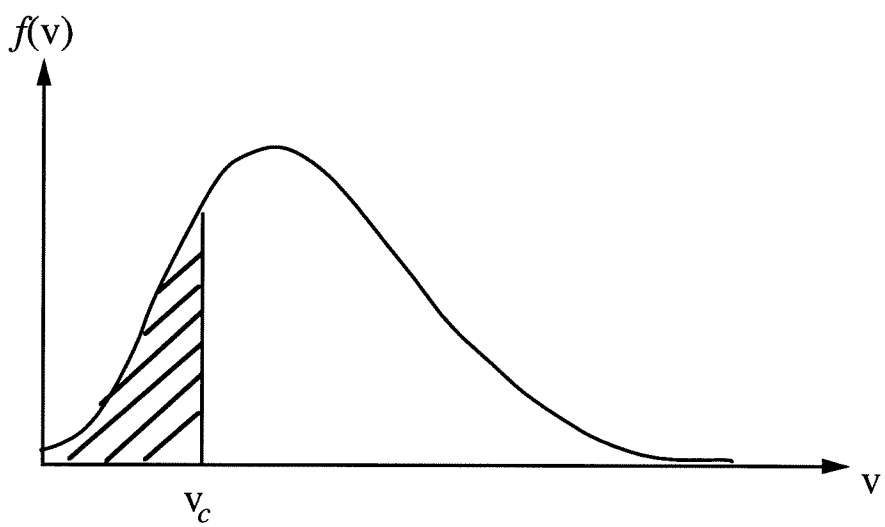

Figure 3.2: The capture rate of the trap is determined by the number of atoms entering the volume enclosed by the trapping laser beams with velocity below a certain capture velocity v_c.

where one can recognize $(1/4)n_{\mathrm{Cs}}v_{\mathrm{Th}}$ as the total number of atoms entering a unit area in a unit time, and $(v_c/v_{\mathrm{Th}})^4$ arises from our requirement that the initial velocity be less than v_c.

From the requirement that an atom having velocity v_c be stopped within distance d — the diameter of the trapping laser beams, one finds that:

$$v_c^2 \approx 2v_{\mathrm{rec}}\Gamma d, \tag{3.8}$$

where $v_{\mathrm{rec}} = \hbar k/m$ is the recoil velocity or the slowdown in velocity caused by each scatter with a photon in the trapping laser. The total scattering rate Γ is given in Section 2.6 as $\Gamma = \gamma_\perp(I/I_s)/[1 + I/I_s + (\Delta/\gamma_\perp)^2]$.

Given the loss and capture rates, the number of atoms in the trap, n, is then obtained by solving the simple rate equation:

$$\frac{dn}{dt} = R - Ln. \tag{3.9}$$

Assuming the initial condition $n(t = 0) = 0$, we obtain:

$$n(t) = n_{ss}\left(1 - e^{-Lt}\right), \tag{3.10}$$

where n_{ss} is the number of atoms in the trap in steady state and is given by

$$n_{ss} = \frac{R}{L}. \tag{3.11}$$

Eq. (3.10) implies that when the trap is turned on the number of atoms in the trap increases exponentially with a time constant $\tau_{\mathrm{on}} = 1/L$. Not surprisingly, this is also the same decay time constant when the trap is turned off. Thus the loss rate is the inverse of the time constant for the trap to turn on and off.

However, for Eq. (3.9) to be valid the steady-state number of atoms in the trap n_{ss} needs to be much larger than one, i.e., $n_{ss} \gg 1$. In the case where $n_{ss} \sim 1$, a different approach can be employed where one tracks down the time each atom enters

and leaves the trap. For simplicity, we consider the situation $n_{ss} \ll 1$ [Fig. 3.1(b)], which implies that there is at most one atom in the trap at any given time. After the atom enters the trap, the duration it remains inside the trap, τ_{on}, is decided by the time when the next collision occurs. Thus τ_{on} should be exponentially distributed whose average is the mean free time of the atom in the trap:

$$\tau_{\text{on}} = 1/L. \tag{3.12}$$

Similarly, the duration of off-intervals in Fig. 3.1(b) is also exponentially distributed with its mean being the filling rate:

$$\tau_{\text{off}} = 1/R, \tag{3.13}$$

thus the average number of atoms is again:

$$n_{ss} = \frac{\tau_{\text{on}}}{\tau_{\text{off}}} = \frac{R}{L}. \tag{3.14}$$

We shall conclude this section with a discussion of the actual magnitude N_1 of the jumps in fluorescence associated with a single trapped atom (cf. Fig. 3.1). The total number of photons an atom emits under resonant light of intensity I and detuning Δ is given by the total scattering rate Γ,

$$\Gamma = \gamma_{\perp} \frac{I/I_s}{1 + I/I_s + (\Delta/\gamma_{\perp})^2}. \tag{3.15}$$

Our detection system captures only a fraction f of the total 4π solid angle the atom emits into, and has a transmission coefficient T_0 and quantum efficiency α. Thus, the number of counts one expects in a counting interval Δt is,

$$N_1 = \Gamma f T_0 \alpha \Delta t. \tag{3.16}$$

3.3 Design Considerations

Having understood the physics behind single-atom trapping, one is confronted with the task of designing and constructing the appropriate experimental apparatus, as well as adopting a feasible measurement scheme to observe the relevant phenomenon, i.e., the discrete steps in Fig. 3.1. Our analysis here focuses on three key quantities discussed in the last section, namely, the duration of the steps (on-time) $\tau_{\rm on}$, the expected counting rate N_1, and the steady-state number of atoms in the trap n_{ss}. A logical approach, then, is to start from the simplest quantity and determine in turn each experimental devices and parameters. Such an approach is adopted and presented here. In practice, however, the factors controlling these quantities are often entangled and sometimes even conflict with each other. One is forced to consider the experiment as a whole and make compromises required by the various parts of the experiment.

3.3.1 The Duration of the Steps $\tau_{\rm on}$

The duration of the steps [the on-time in Fig. 3.1(b)] depends solely on the vacuum and is the simplest observable quantity to start with. According to Eq. (3.4) and Eq. (3.12), $\tau_{\rm on}$ is inversely proportional to the sum of the residual background pressure $p_{\rm BG}$ and the background Cs pressure $p_{\rm Cs}$. For reasons that shall become clear later in Section 3.3.3, $p_{\rm BG}$ is usually much larger than $p_{\rm Cs}$ under conditions of single-atom trapping, thus $\tau_{\rm on}$ is determined only by the residual vapor pressure and thus on the quality of the vacuum system.

A detailed discussion about the vacuum system is presented in Section 3.3.3. The typical pressure in the main chamber is about $p_{\rm BG} \approx 6 \times 10^{-9}$ torr after reaching a steady state. Using values in Ref. [3] for the collision cross section σ, i.e., $\sigma \sim 2 \times 10^{-13}$ cm^2, and thermal velocity of N_2 at 300 K ($\sim$ 400 m/s) for the value of u, we find that,

$$\tau_{\rm on} = 1/L \sim 0.6 \text{ s}. \tag{3.17}$$

While this might not be considered to be long according to human perception, it is long enough for a variety of experiments, such as cavity QED experiments, in which the transit times of the atomic beam across a laser beam waist are often measured in microseconds.[24]

3.3.2 The Expected Count Rate N_1

Once the duration of the steps is determined, we are able to choose a reasonable time interval [Δt in Eq. (3.16)] during which to detect the fluorescence emitted from the trap: Δt should be short enough to resolve the individual steps, yet as long as possible so that we have enough integration time, i.e., $\Delta t \lesssim \tau_{\rm on}$. In most of our experiments, Δt is chosen to be:

$$\Delta t = 0.1 \text{ s}. \tag{3.18}$$

Another important factor in determining the expected number of counts is the quantum efficiency (QE) of the detector. The detector we choose is a RCA model SPCM-100-PQ photon counting module based on an avalanche photodiode (APD). At dark counts of only about 6 counts/0.1 s, it provides a QE of about 25%, which is relatively high at this wavelength (852 nm). Since the signal level we are detecting is about 400 counts/0.1 s whereas the noise level itself is more than 4,000 counts/0.1 s, it is a convenient alternative to the use of photomultiplier tubes, making the photon counting module the detector of choice before low light-level CCD and intensified CCD cameras became commercially feasible. However, a drawback of using the APD system is that it is essentially a single pixel device, providing no imaging capability. To tackle this problem, an intensified CCD camera system (Xybion Electronics System, model ISG-350 low light-level video camera) was purchased recently and has the capability of detecting light level as low as 10^{-7} fc, which is equivalent to a sensitivity of about 1 photon/sec/pixel. The intensified CCD camera would presumably also solve another problem associated with the APD: the effective detection area of this device is only about 150 μm $\times$ 150 μm, making it relatively difficult to design an imaging system to match such a small imaging area.

Unfortunately, the collection solid angle $4\pi f$ is also an important factor in determining N_1. To achieve small f-number and low aberration at the same time presents a major challenge to the design of the imaging system. Moreover, there is added complexity that one cannot place the imaging optics too close to the trap without incurring substantial scattering by the imaging lens itself. Such a restriction would exclude some well-developed schemes such as microscope objectives. This, combined with the fact that part of the imaging system needs to be placed inside the vacuum chamber to achieve maximum collection solid angle, makes it difficult to find a commercial off-the-shelf product to meet all these requirements.

A modest approach we adopted is shown in Fig. 3.3(a). An assembly consisting of a meniscus lens (L4) of focal length 100 mm (Melles Griot 01-LMP-001) and a plano-convex lens (L5) of focal length 70 mm (Melles Griot 01-LPX-137) is positioned about 3.3 cm from the trap in the vacuum chamber to collimate the light emitted from the trap. Our ray-tracing program indicates that the combined system has a focal length of about 4.2 cm and collimates light emitted from its focal point to better than 0.2°. A refocusing lens, a TV lens of focal length 35 mm is placed about 12 inches outside the chamber and refocuses the light to the APD. Since no detailed data for the surface of the TV camera is available, we cannot simulate the whole imaging system on the computer. However, we have simulated a similar, albeit inferior system by replacing the refocusing TV lens with the collimating lens assembly working backwards [Fig. 3.3(b)]. For this system, we find that for the light emitted from a point source at its focal point to spread into a circle of less than 150 μm in diameter at its imaging plane, the half angle θ for the incident light cone must be: $\theta \lesssim 11.5°$. Thus, the collection efficiency is:

$$f = \frac{\Delta\Omega}{4\pi} = \frac{\int_0^{\theta}\int_0^{2\pi}\sin\theta d\theta d\phi}{4\pi} = 1\%. \tag{3.19}$$

The choice of the imaging system also determines the total transmission T_0 of the collection optics. Since the TV lens used for refocusing the light is not optimized for 852 nm, it has a transmission of only 80%. Together with the four glass surfaces

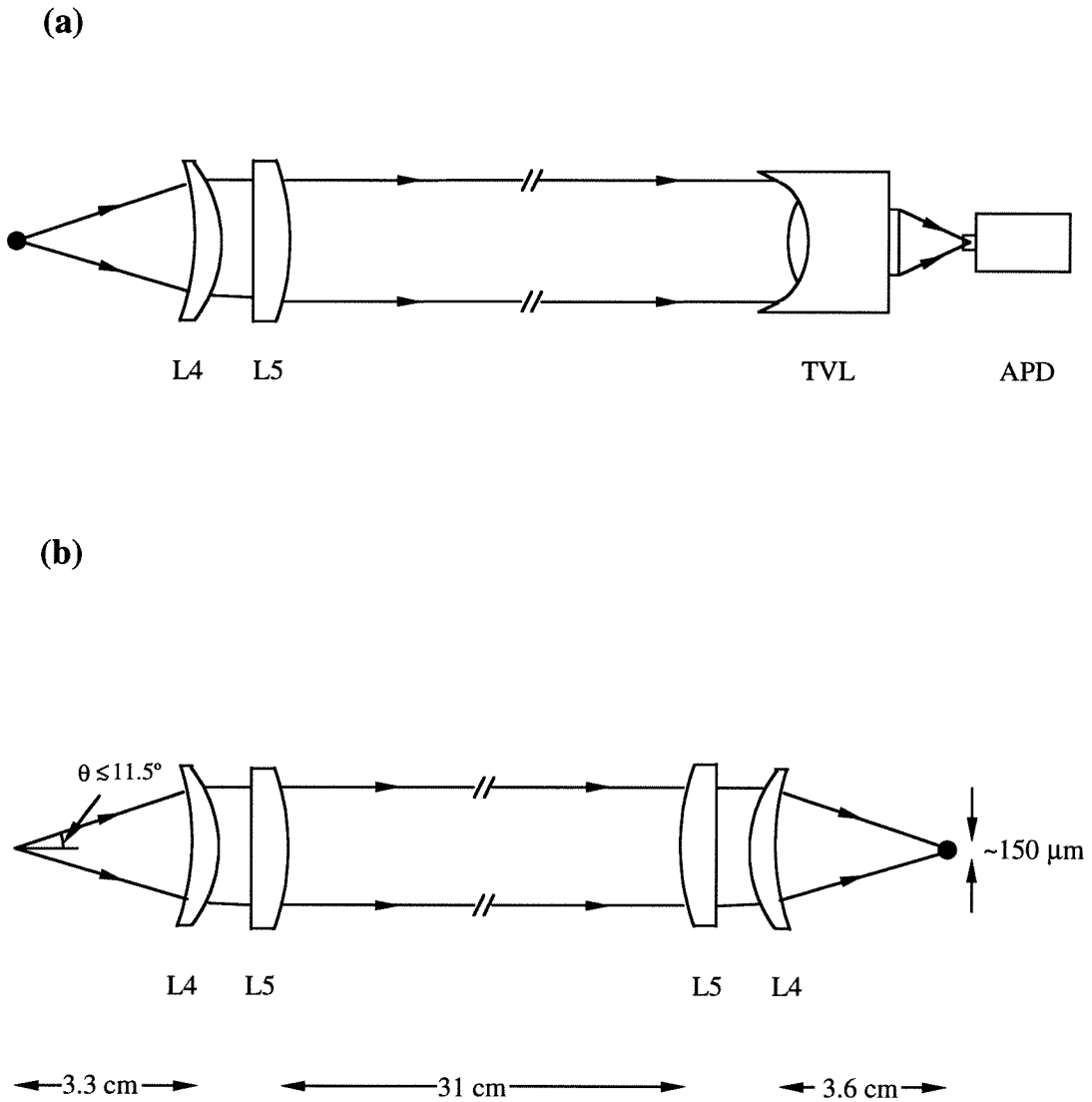

Figure 3.3: The imaging system for the single-atom experiment. (a) imaging system used to observe fluorescence from single-atom trap. (b) Imaging system used for ray-tracing. L4: meniscus lens (Melles Griot 01-LMP-001), $f = 100$ mm; L5: plano-convex lens (Melles Griot 01-LPX-137), $f = 70$ mm; TVL: TV lens, $f = 35$ mm.

of the collimating lens assembly and two quartz surfaces of the vacuum window, we estimated the total transmission of our optical system to be:

$$T_0 \approx 70\%. \tag{3.20}$$

The last factor in Eq. (3.16) is Γ — the scattering rate. Unlike other parameters in this equation, the scattering rate is already fixed by the constraints imposed by other parts of the experiment. According to Eq. (3.15), the scattering rate depends on the total trapping intensity I and the detuning Δ. Δ is usually determined empirically by optimizing the trap at a relatively high number of atoms and has a value of about $2\pi\times 6$ MHz. The scattering rate Γ saturates at an intensity $I \gg I_s$, with I_s being the saturation intensity. There is further complication about the saturation intensity I_s because there are different Zeeman sublevels in the presence of a magnetic field. The widely quoted value of $I_s = 1$ mW/cm^2 is for the transition $F = 4, m_F = 4 \rightarrow F' = 5, m_{F'} = 5$. In the presence of a magnetic field, the atoms could be distributed over all the Zeeman sublevels and we need to average over these sublevels much like the process illustrated in Ref. [65]:

$$I_s = I_{4\rightarrow 5} \times \frac{\sum_{m_F=-4}^{+4} 1}{\sum_{m_F=-4}^{+4} |\langle F=4, m_F | F'=5, m_F+1\rangle|^2} = 2.5 \text{ mW/cm}^2, \tag{3.21}$$

with $\langle F, m_F | F', m_{F'}\rangle$ being the Clebsch-Gordan coefficient shown in Fig. 3.4.

With these values for the saturation intensity, and the total intensity in the trapping beams $I = 10$ mW/cm^2, also dictated by the optimization of the trap, we have:

$$5 \times 10^6/\text{s} \lesssim \Gamma \lesssim 9 \times 10^6/\text{s}. \tag{3.22}$$

We are finally able to make a numerical estimate for the value N_1 — the expected number of counts in time Δt: with counting interval $\Delta t = 0.1$ s, quantum efficiency

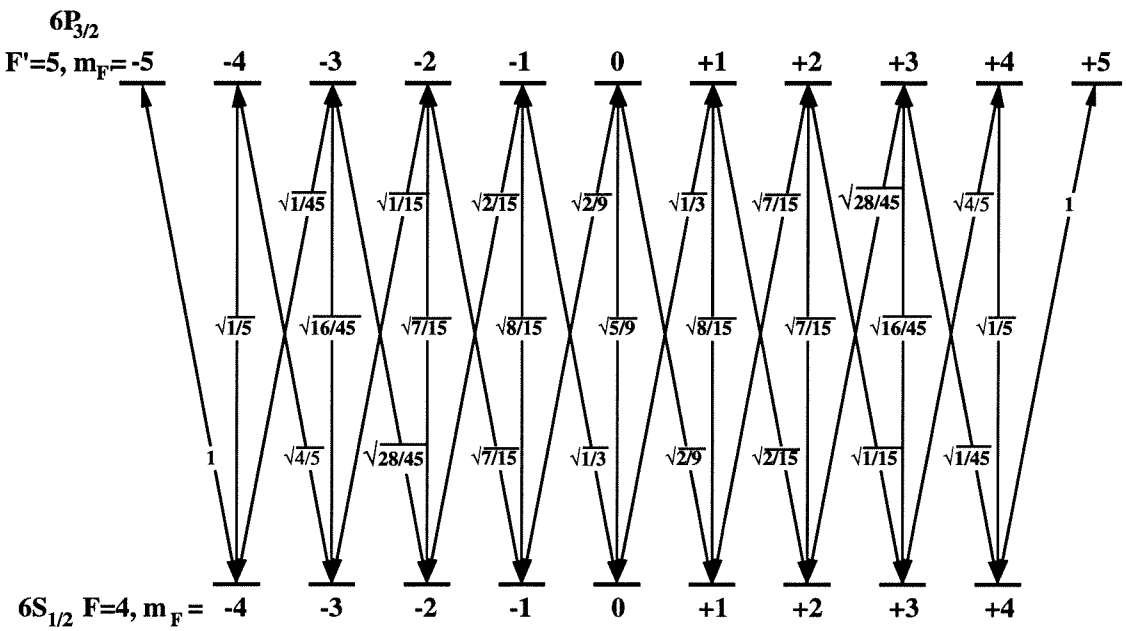

Figure 3.4: The Clebsch-Gordan coefficients $\langle F, m_F | F', m_{F'} \rangle$ for the transition $6S_{1/2}, F = 4 \rightarrow 6P_{3/2}, F' = 5$ in Cs atom.

$\alpha = 25\%$, total transmission $T_0 = 70\%$ and collection efficiency $f = 1\%$, we have:

$$0.9 \times 10^3 \lesssim N_1 \lesssim 1.6 \times 10^3. \tag{3.23}$$

While this is considerably larger than the lowest detectable limit of the APD module (the absolute dark count is about 6 counts/0.1 s), one still needs to take special caution in order to distinguish the signal from any spurious noise counts. The noise comes mainly from three sources: the stray room light, the fluorescence caused by Cs background vapor not captured by the trap, and the scattered light from the vacuum window and other components close to the trap. The noise from room light can usually be reduced to less than 100 counts/0.1 s by carefully shielding the detector with black paperboards and clothes. The background fluorescence depends on the Cs background pressure and is of little concern under the condition of single-atom trapping. An overwhelming portion of the background noise comes from the scatter of the trapping laser and repumping laser by the vacuum windows and nearby optical components. In fact, this kind of noise is one of the evil villains we are constantly battling with. With the presence of the strong trapping beams with a flux totaling 2.6×10^{14} photons/0.1 s (0.6 mW), even a scatter of one in a billion is going to cause devastating consequence for our experiment. This is one of the major reasons why we upgraded from the simple glass cell to the stainless steel chamber, which allows us to put AR coated windows (Larson VQZ-400-F6 and VQZ-150-F2, coated by Thin Film Devices, Inc., Anaheim, CA) far away from the trap, minimizing the chance of scattering by the optical components close to the trap (cf. Section 3.3.3). But even with these arrangements, the total noise level is still over 4,000 counts/0.1 s, causing serious difficulty in measurement. Improvements to this end involve pushing the vacuum window further away from the trap and placing light absorbing baffles inside the chamber to reduce scattering.

3.3.3 The Number of Atoms in the Trap n_{ss}

We will now turn to the most important quantity in the single-atom trapping experiment — the steady-state number of atoms in the trap n_{ss}.

According to Eq. (3.14), Eq. (3.4), Eq. (3.7) and Eq. (3.8),

$$n_{ss} = \frac{3\sqrt{\pi}}{2} \frac{v_{\text{rec}}^2 \Gamma^2}{\sigma u v_{\text{Th}}^3} \left(\frac{p_{\text{Cs}}}{p_{\text{BG}} + p_{\text{Cs}}} \right) d^4. \tag{3.24}$$

Most factors in this equation, like σ, u, and Γ are discussed in previous sections, while others, like v_{Th} and v_{rec} are fixed by the particular choice of the atom used (Cs for this experiment). However, there are two important parameters worth noting here, the first of which being d, the beam diameter. According to Eq. (3.24), the number of atoms in the trap is proportional to the fourth power of d, making it an attractive candidate to control the number of atoms in the trap. Ref. [56] demonstrates that it is possible to achieve traps containing 3.6×10^{10} atoms at a density of 3.6×10^{10} atoms/cm^3 using large beams of 4 cm in diameter. To the other extreme, it is tempting to use the same method to reduce the number of atoms in the trap by using smaller beams. However, a more careful investigation by Ref. [70] shows that under a certain threshold value for d, the number of atoms in the trap decreases dramatically with the decrease of beam size, thus making it very difficult to obtain a trap in the first place. Our experience with the aligning of the trap confirms this result. Thus, to exploit the maximum potential of this method, we have put an aperture (APT in Fig. 3.8) in the path of the main beam before it is split into five trapping beams. This way we can conveniently control the size of all five trapping beams without significantly misaligning the trap. In the experiment (Section 3.4), before the measuring apparatus is switched over from the video camera to the photon counting module, we close down the aperture as much as we can, realigning the beams slightly if necessary to optimize the trap. This way we can reduce the beam diameter to a minimum of about 2 mm, i.e.,

$$d = 2 \text{ mm}. \tag{3.25}$$

This is measured by the FWHM of the beam at the position of the trap. It is of reasonably smooth shape despite the clipping of the aperture to the original Gaussian beam (of waist ~ 6 mm).

Before going on to discuss the next factor in Eq. (3.24), we will briefly note here that we are now in a position to make a numerical estimate for the capture velocity v_c. Using Eq. (3.23) for Γ, we obtain from Eq. (3.8) that $v_c \approx 10$ m/s. this is much less compared to the thermal velocity of Cs atoms at room temperature $v_{\rm Th} = (2k_BT/m)^{1/2} = 194$ m/s, and thus our approximation (that $v_c \ll v_{\rm Th}$) in deriving Eq. (3.7) is justified.

The last but perhaps most important term in Eq. (3.24) is $p_{\rm Cs}/(p_{\rm BG}+p_{\rm Cs})$, which states that if the background Cs pressure is much larger compared to the background pressure from other vapors, i.e., $p_{\rm Cs} \gg p_{\rm BG}$, then the number of atoms in the trap is independent of the background Cs pressure and is inversely proportional to the background vapor pressure $p_{\rm BG}$. This is the case in most other conventional experiments where changing the Cs pressure does not significantly influence the number of atoms in the trap.[3] In the single-atom trapping experiment, however, our goal is to reduce the Cs pressure so that it falls below the background vapor pressure $p_{\rm BG}$, at which point the number of atoms n_{ss} starts to decrease linearly with the decrease of the background Cs pressure $p_{\rm Cs}$.

To get into that regime, however, requires careful design of the vacuum system and Cs source. Fig. 3.5 shows the final version of our vacuum apparatus when the data is taken. The Cs source [Fig. 3.5(b)] is a glass ampule containing the Cs atoms. It is connected to a metal flange by means of glass-to-metal seal. A copper sleeve, cooled by two thermal-electric-coolers (Peltier coolers) in series, makes thermal contact to the glass ampule and is surrounded by a foam cup, which is used to insulate the air and thus prevents water from freezing on the cold finger. For the same purpose, dry N_2 gas is introduced into the compartment surrounded by the cup to blow out the water vapor. Such a humble system works surprisingly well and is capable of cooling the ampule down to about -34 °C, measured by a thermistor attached to the copper sleeve.

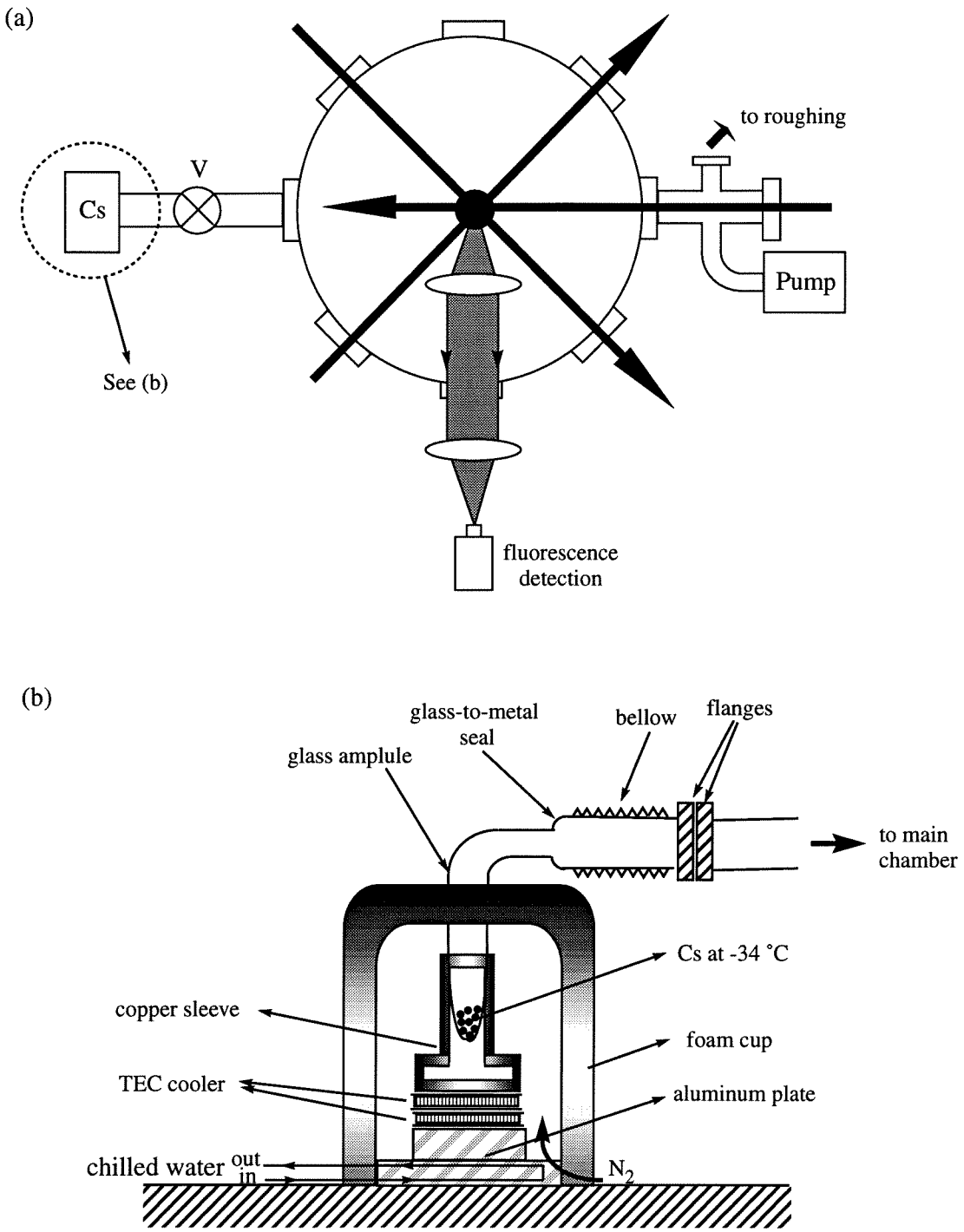

Figure 3.5: The vacuum chamber and Cs source for the single-atom experiment. (a) The vacuum chamber. (b) The details of the Cs source and cold finger.

Standard textbook theory assumes that the background Cs pressure in the chamber, the all important p_{Cs}, is determined by the vapor pressure of Cs at the cold finger temperature. But this is true only when the system is clean and free of adsorption by Cs atoms on the surface, a condition achieved only after a thorough baking or at system startup. Shortly after that, the adsorbed Cs atoms on the surface becomes a secondary source which is not negligible because such atoms are at room temperature and the vapor pressure of Cs at room temperature is three orders of magnitude larger than the vapor pressure at -34 °C (Fig. 3.6). This is also evidenced in Fig. 3.7, where the fluorescence light emitted from Cs atoms from a fixed volume of the background Cs vapor after a thorough baking of the glass cell is measured by the photon counting module described in Section 3.3.2 and plotted on the y-axis versus time after baking. In Fig. 3.7 the pressure on the right is calculated from an extrapolation of the fluorescence count data obtained after the system reaches equilibrium state and calibrated against the vapor pressure of Cs atoms at room temperature. During the course of the measurement, we have raised the temperature of the cold finger several times, and the vapor pressures at the corresponding temperatures are plotted in dashed line. This is also the expected counting rates if the Cs pressure in the cell closely followed the vapor pressure. From Fig. 3.7 one can see that the measured Cs pressure already departs from the vapor pressure only several hours after the baking. In the glass cell there is nothing preventing such a trend, making it necessary to bake the system every few days. It is also clear from Fig. 3.7 that the lowest Cs pressure one can reach in the cell is not less than 5×10^{-10} torr, not enough to achieve single-atom condition according to Eq. (3.24). These and other reasons prompted us to upgrade the vacuum system from the simple glass cell to an all metal stainless steel chamber, as shown in Fig. 3.5(a). It is a custom-made feed-through collar manufactured by Nor-Cal Products, Inc. Its six-inch diameter makes it possible to place imaging optics inside the chamber to achieve higher collection solid angle; yet the chamber is still small enough to fit comfortably on the tabletop. The larger size also pushed back the nearest scattering component — the vacuum window — to more than three inches away from the trap, compared to less than a centimeter in the case of the cell.

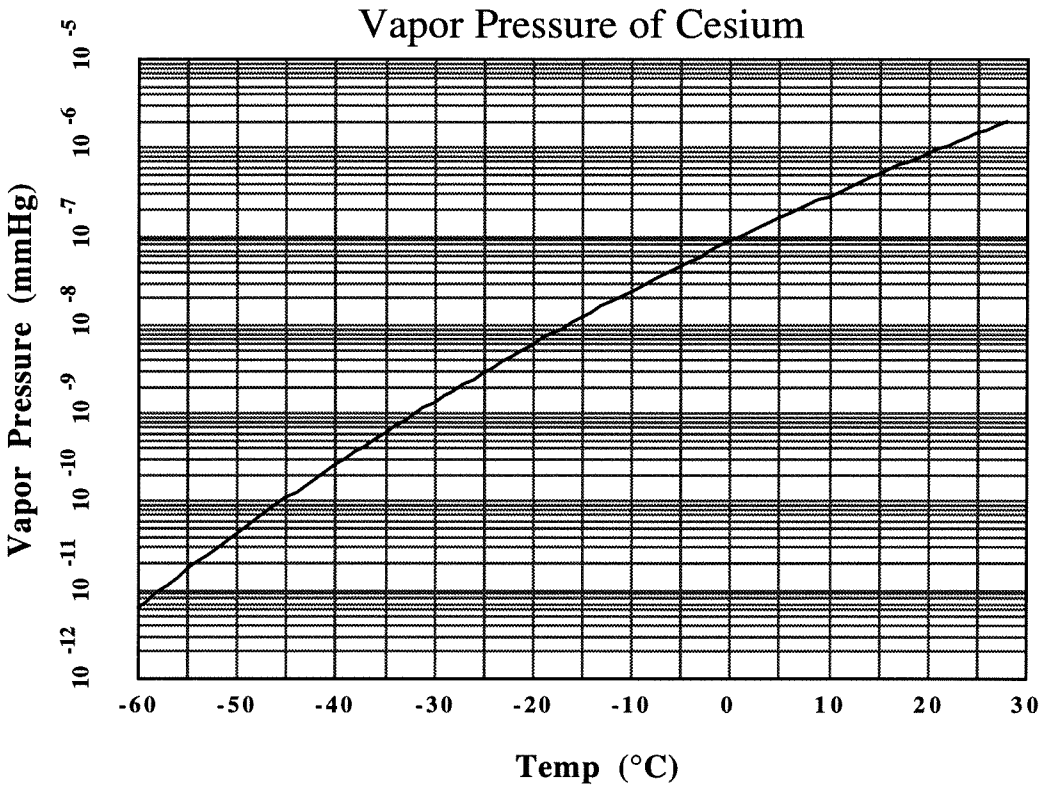

Figure 3.6: Vapor pressure of Cs, $\ln p = -4120/T - 1.0 \ln T + 10.46$, ($p$ in torr, T in Kelvin), after Ref. [71]. The melting point of Cs is 28 °C at 1 atm, making it almost a liquid at room temperature.

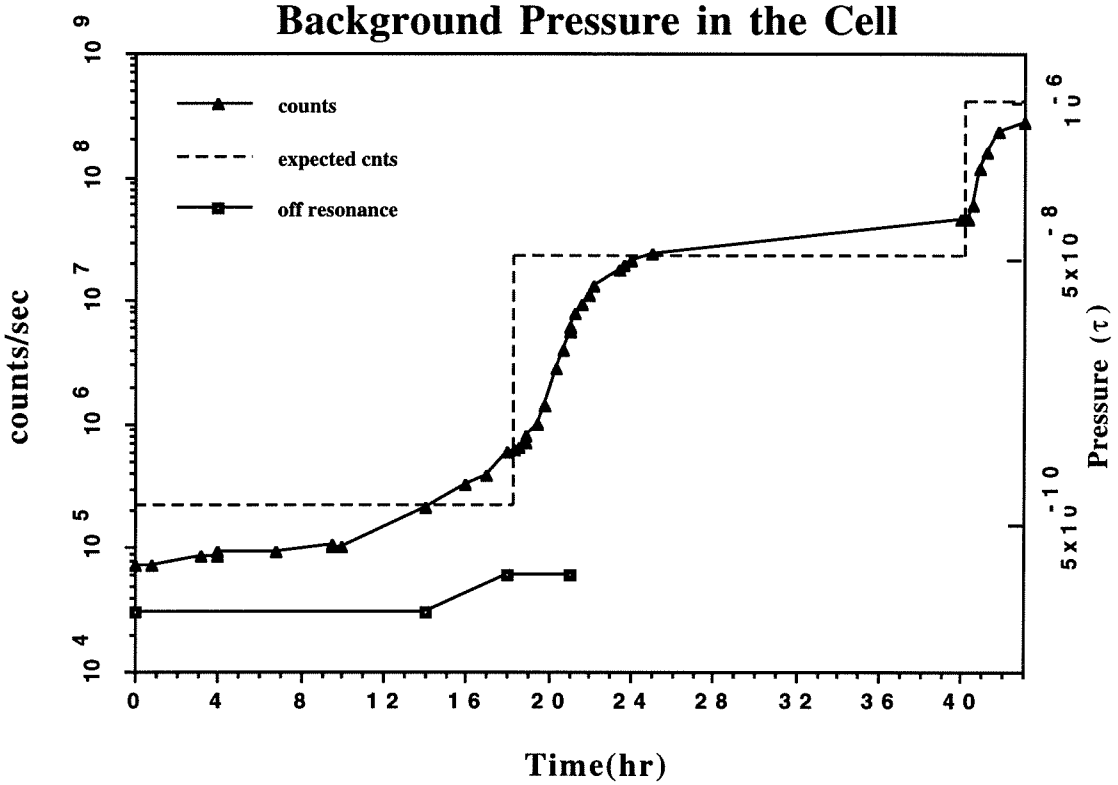

Figure 3.7: The fluorescence counts from a fixed volume of the background Cs vapor in the glass cell versus time after a thorough baking. The pressure and expected counts are calculated from an extrapolation of the fluorescence count data obtained after the system reaches equilibrium state and calibrated against the vapor pressure of Cs at room temperature.

The scattering is further reduced by the AR coated window, compared to relatively low quality glass from which the cell is constructed. The vacuum is also improved because of the low outgassing rate of stainless steel compared to glass. Our system is pumped first by a turbo-molecular pumping station (Varian 4400-MSP-SPL) from atmosphere to about 10^{-6} torr, then the valve to this roughing pump is closed, and an ion pump is turned on. The Varian model 911-5005 pump provides a pumping speed of 8 l/s which matches roughly the conductance of 12 l/s that we are able to achieve through the elbow. This model is chosen because it has very little stray magnetic field, causing less than 20 mG of magnetic inductance at the trap only one foot away. The pressure is deduced from the electric current read by the ion pump controller (Varian 921-2001). Despite the fact that there are optical components held by aluminum holders in the main chamber, we still managed to get a pressure of about 6×10^{-9} torr at the center of the chamber, taking into account the finite conductance and pumping speed of the pump, i.e.,

$$p_{\mathrm{BG}} = 6 \times 10^{-9} \quad \text{torr.} \tag{3.26}$$

But the greatest advantage of the stainless steel chamber comes from the possibility to add an isolation valve V to control the Cs flow into the chamber. At evening or weekend when the experiment is not running, this valve is closed to prevent Cs atoms from contaminating the main chamber. Even during the experiment, after the initial diagnostics are done for the trap containing high number of atoms, this valve is closed down to cut further the supply of Cs atoms into the chamber. Then, with a time constant of typically several hours (the exact length depending on the history of the chamber), the remaining Cs atoms in the main chamber are pumped away by the ion pump. This way it is possible to achieve the low Cs background pressure required by the conditions for single-atom trapping, estimated in Section 3.5 to be about 2×10^{-16} torr, i.e.,

$$p_{\mathrm{Cs}} \sim 2 \times 10^{-16} \text{ torr.} \tag{3.27}$$

Before we conclude this section, we note that our atomic source is differrent than

the atomic beam usually seen in this type of experiment.[2] Rather, it is more like the thermal beam described in Ref. [5]. To construct a real atomic beam would require long arms with collimating slits to collimate the Cs atoms. Such an apparatus would perhaps take a space more than able to fit on the tabletop.

Finally, we acknowledge that our system is far from ideal and perfect for our purpose and is a product of comprise between quality and effort. Improvements to this end would reduce both the background Cs and other gas pressure. For example, our Cs ampule and cold finger could be eliminated by employing the alkali metal dispensers (AMD)[72] developed by SAES Getters, SpA. An AMD consists of a mixture of powders, usually an alkali metal chromate and a reducing agent rolled around by a metallic strip to form a wire. The Cs is bound in the chemical compound under normal temperature but is released when electric current passes through and its surrounding temperature is elevated. The evaporation flow rate is controlled by the amount of current and is thus reproducible and accurate. Unfortunately, at present time our experiment could not yet benefit from this technique because it could only supply atoms at a relatively large flux. If the future developments in this product enable it to supply a lower flux of atoms, then our isolation valve would be obsolete and would be replaced by a more capable "valve" — the electric current which could regulate the Cs flow continuously. Besides this dramatic alteration to the atomic source, a modest improvement can be achieved by placing proper Cs absorbing chemical compounds in the chamber.

3.4 The Experiment

In this section we will turn to the actual operation of the experiment. The complete setup for the single-atom trapping experiment is shown in Fig. 3.8. Most of the parts are discussed in Chapter 2, e.g., the laser is described in Section 2.2, the frequency stabilization scheme is described in Section 2.3, and the repumping diode laser in Section 2.5. Others, like the detection optics, the vacuum chamber, and the Cs source, are described in the previous section. A significant part of the table space

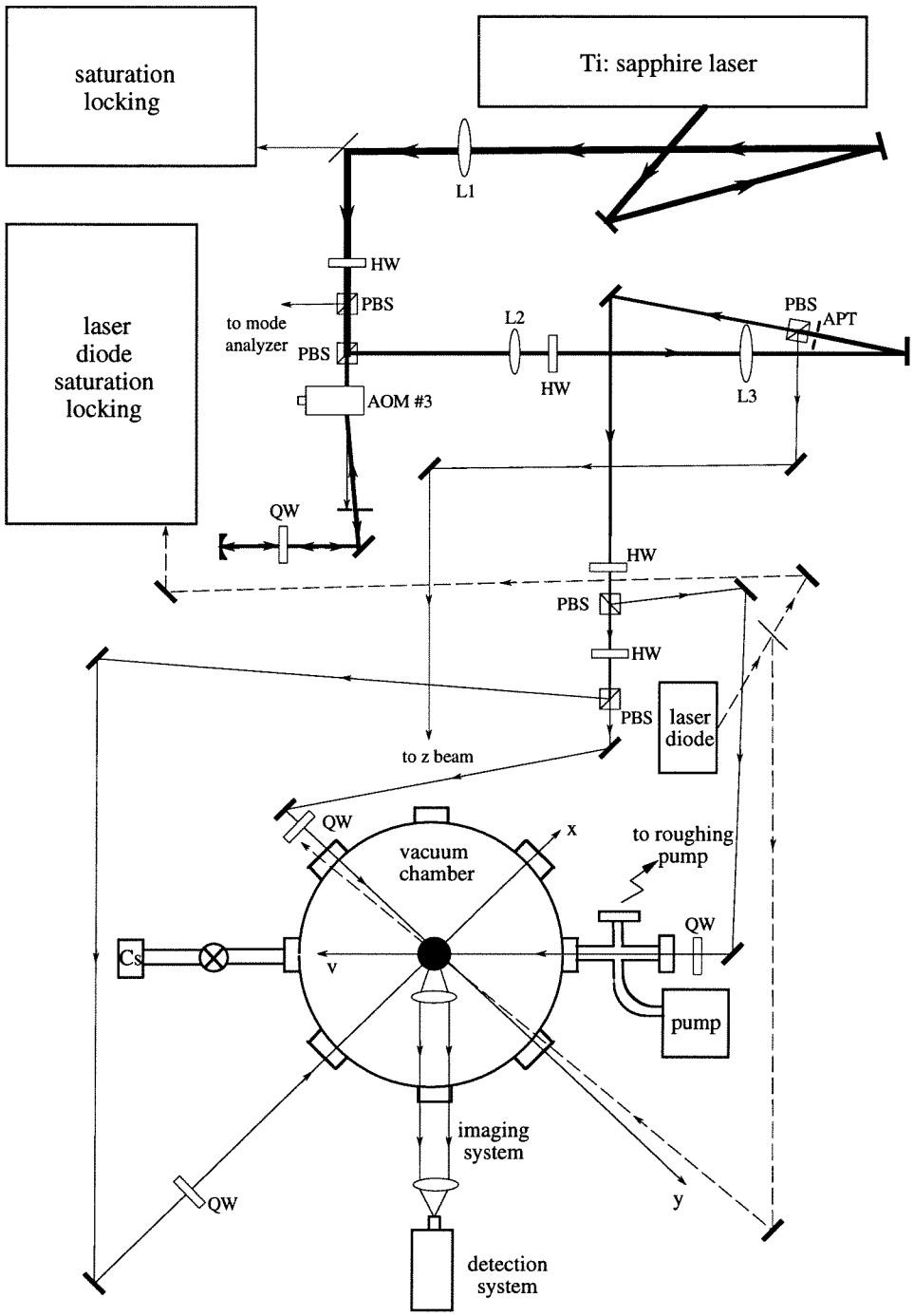

Figure 3.8: The complete setup for the single-atom trapping experiment. HW: half-wave plate; QW: quarter-wave plate; PBS: polarization beamsplitter; APT: aperture, see previous section; AOM#3 and saturation locking: see Section 2.3; Ti:sapphire laser (in solid line): see Section 2.2; laser diode (in dashed line) and laser diode saturation locking: see Section 2.5; vacuum chamber, pump, imaging system and detection system: see previous section; L2 and L3: telescope, see Section 2.5. L1: Newport LBX 082, $f = 50$ cm; z beams (not shown) propagate into and out of the page; mirrors and beamsplitters are not marked.

is dedicated to the splitting and balance of the beams, using half-wave plates (HW) and polarization beamsplitter (PBS) combinations. As mentioned in Section 2.5, we use five beams for our trap instead of the usual six beams to avoid the striation effect associated with the standing waves.

During the experiment, the trap is first observed on the TV screen by a Cohu TV camera. This camera has a sensitivity of about 0.04 fc, about 4×10^5 times worse than that of the Xybion intensified CCD camera. The purpose of using the TV screen is to align and optimize the trap at a high number of atoms, usually containing about 10^6 atoms, similar to those shown in Fig. 4.5. The procedure for optimizing the trap varies, the main criteria being the roundness of the trap and the distribution of atoms in the trap. One can also alter the magnetic field gradient and observe the movement of the trap: if the trap is located at the center of the field gradient and is well-aligned, it changes little during the process. Another criteria is the trend of the trap when the aperture (APT in Fig. 3.8) mentioned in Section 3.3.3 is closed down: as the aperture is inevitably not in the center of the main beam, the five beams will be cut off differently when the aperture is closed down, requiring realignment of the trap. Nevertheless, a well aligned trap should require a minimum of such realignment and usually converts fairly smoothly as one reduces the beam size to its minimum, i.e., $d = 2$ mm according to Eq. (3.25).

Once the limit of the TV camera is reached, the valve V (cf. Section 3.3.3 and Fig. 3.5) which separates the main chamber from the Cs source is closed down to reduce the background Cs pressure in the main chamber, the camera is replaced by the APD system described in Sec 3.3.2. The output of the APD, in TTL pulse format, is fed both into a digital counter (HP 5334B Universal Counter) and an analog ratemeter. The HP 5334B displays on the front panel the number of TTL pulses it detected in a preset gating time Δt, which, according to Eq. (3.18), is typically set to $\Delta t = 0.1$ s. The HPIB interface of the counter allows us to transfer the data into the computer, an HP 382 controller, for storage and further analysis. The data acquisition software, written in HP Basic language, allows us to perform variance calculation, sorting and histogram analysis, in addition to taking data and plotting them on the

computer screen. The ratemeter is used as a means to independently confirm the result reported by the counter. The TC 527 LOG/LIN ratemeter manufactured by Tennelec integrates the signal it receives at its input for a time constant which we also set to be 0.1 sec. The output, an analogue signal whose amplitude is proportional to the integrated rate, is sent to a digital oscilloscope (Lecroy 9400, 125 MHz) for continuous monitoring of the counting rate.

During the transition period, before the pressure falls low enough for the single-atom trapping condition to be reached, it is already evident from Fig. 3.9 that the number of atoms in the trap n_{ss} is in the regime $n_{ss} \ll N_1$. Fig. 3.9 plots the fluorescence counts from the trapped atoms $C_{\rm trap}$ on the x axis versus its relative variance $\sigma_{C_{\rm trap}}/C_{\rm trap}$, which is plotted on the y axis. According to Eqs. (3.2) and (3.3), the relative variance of $C_{\rm trap}$ does not depend on n_{ss} at $n_{ss} \gg N_1$, but varies as $1/\sqrt{n_{ss}}$ when $n_{ss} \ll N_1$. In Fig. 3.9, the experimental data are roughly scattered around the curve $\sigma_{C_{\rm trap}}/C_{\rm trap} = \sqrt{350/C_{\rm trap}}$, which indicates that we are in the regime $n_{ss} \ll N_1$ and $N_1 \sim 350$. The relationship $C_{\rm trap} = N_1 n_{ss}$ then implies that n_{ss} for the data shown in Fig. 3.9 is in the range $n_{ss} \lesssim 6$.

When the background Cs pressure falls yet lower, we are finally able to record traces suggesting single atom. These traces are shown in Figs. 3.10 and 3.11 and discussed in the next section.

3.5 Experimental Results and Data Analysis

The experimental results are shown in Figs. 3.10 and 3.11, where the detected fluorescence counts from the trap are plotted versus time. Fig. 3.11 shows the data recorded by ratemeter and taken by the digital oscilloscope, which offers a close-up view of the short term fluctuations in the fluorescence counts; while Fig. 3.10 shows the long-term variation of the data over a course of 100 sec. In addition, Fig. 3.10, whose data are recorded by the digital counter and taken by the computer, provides the absolute magnitude of the fluorescence counts for comparison with the theoretical predictions. Although not recorded simultaneously, they are obtained under similar experimental

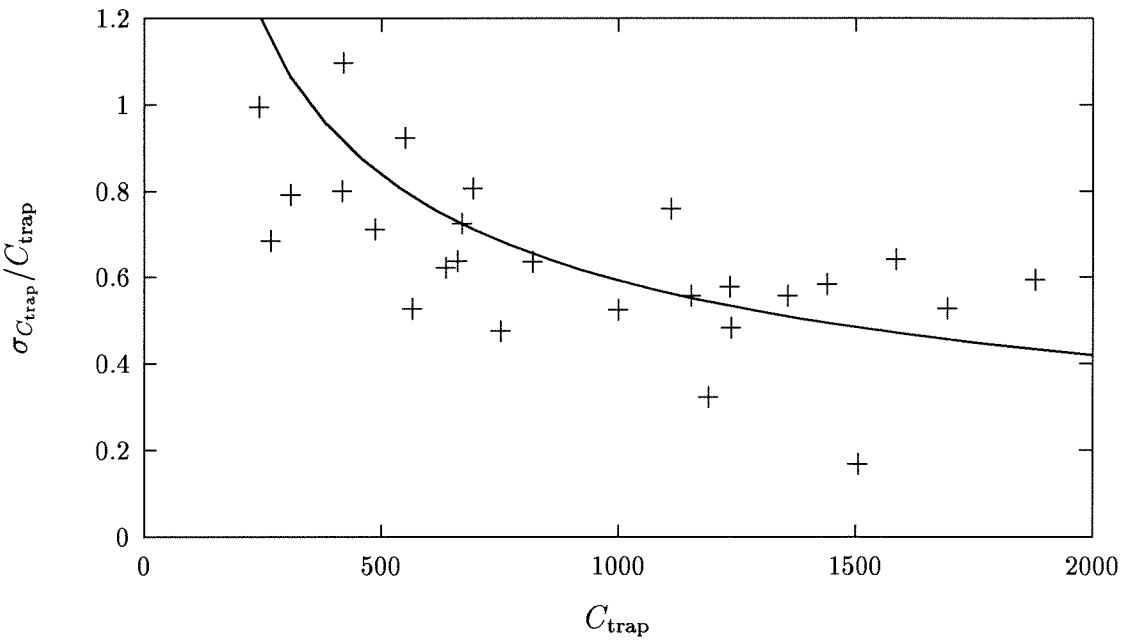

Figure 3.9: The relative variance $\sigma_{C_{\text{trap}}}/C_{\text{trap}}$ of the fluorescence signal from the trap versus signal size C_{trap} measured in the transition period. The "+" denotes data taken from the experiments, while the curve is $\sigma_{C_{\text{trap}}}/C_{\text{trap}} = \sqrt{350/C_{\text{trap}}}$. C_{trap} is obtained by subtracting the background counts C_0 from the total fluorescence counts C, $C_{\text{trap}} = C - C_0$, cf. Fig. 3.10 and 3.11.

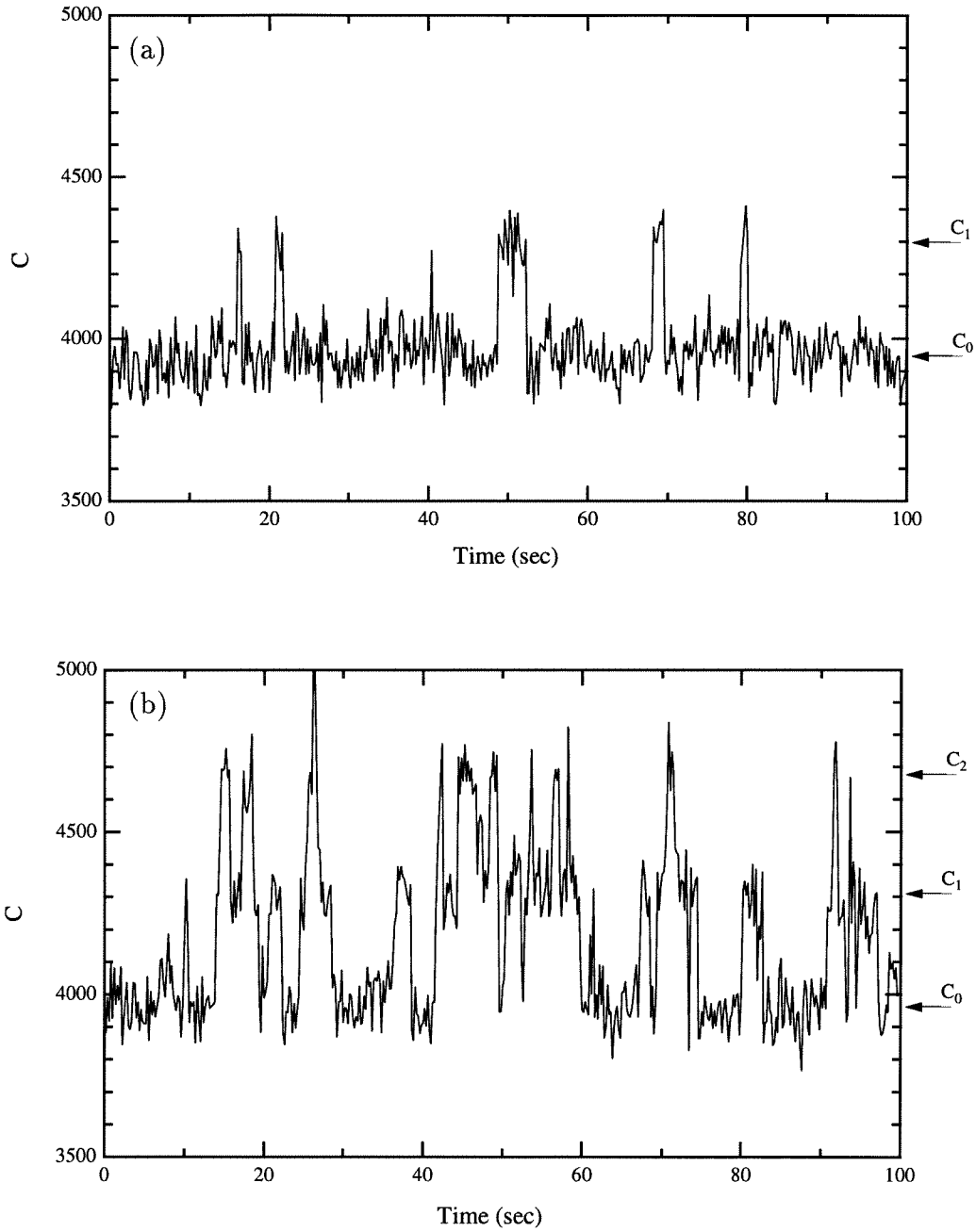

Figure 3.10: Fluorescence signal C (counts/0.1 s) versus time under conditions of very low Cs background pressure. The discrete steps evident in the Figure are interpreted as arising from the arrival and departure of individual Cs atoms in the trap. In moving from (a) to (b), the background Cs pressure has been increased by injection of a small amount of Cs through the V valve (cf. Section 3.3.3 and Fig. 3.5). The total trapping intensity is $I = 10$ mW/cm^2, and the trapping laser detuning is $\Delta/2\pi = 6$ MHz.

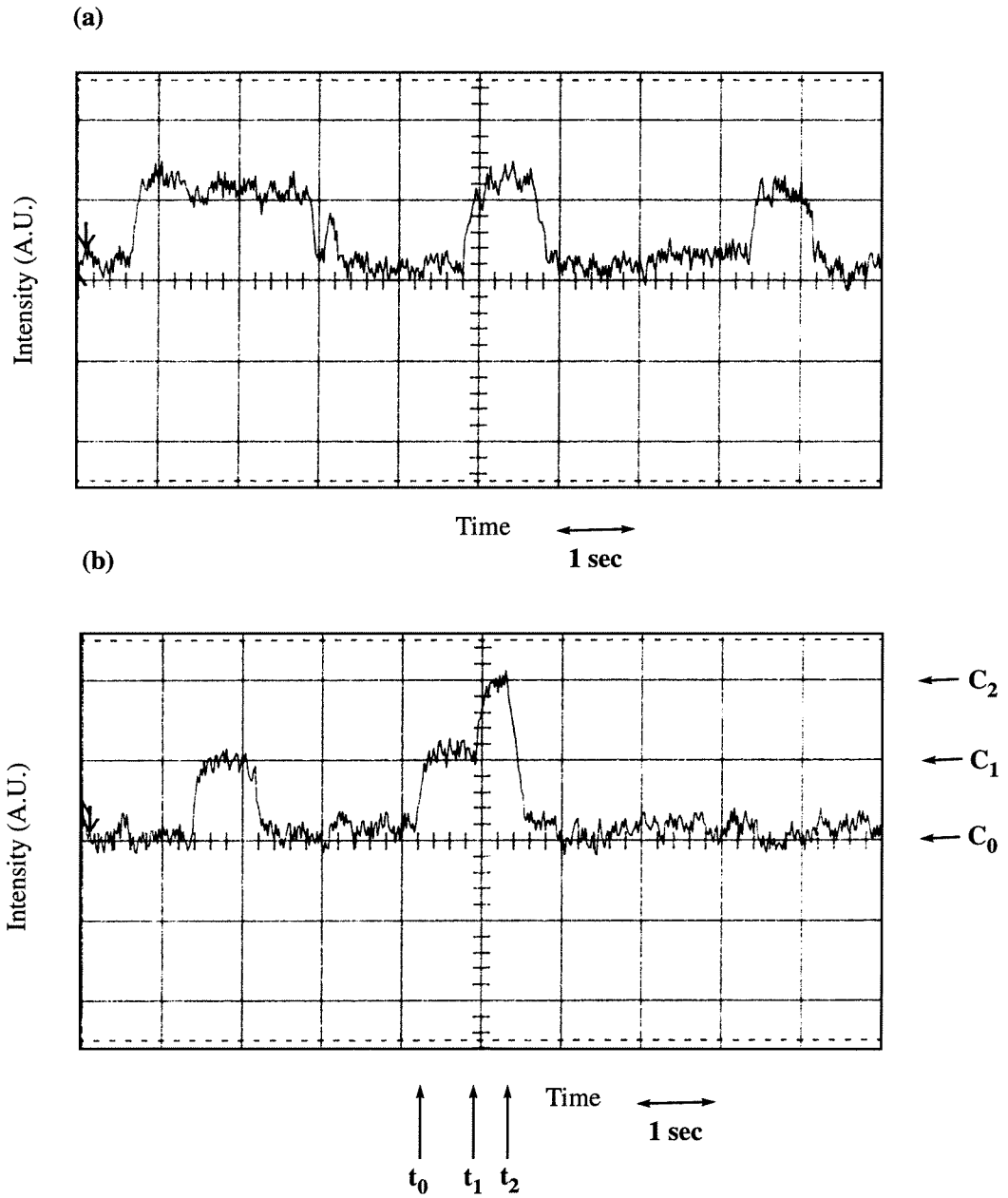

Figure 3.11: Traces of fluorescent counts versus time measured by the ratemeter. (a) and (b) are under similar conditions as in Fig. 3.10(a) and Fig. 3.10(b), respectively, but recorded at a different time.

conditions. From Figs. 3.10 and 3.11 we see that the counting rates exhibit distinct steps above a background level C_0, where C_0 is associated with (nonresonant) scattering from various optical components. (A discussion on what contributes to this background and how to reduce it is presented at the end of Section 3.3.2.) For example, in Fig. 3.11(b) we can associate the well separated jumps C_1 and C_2 during time period $[t_0, t_2]$ with the fluorescence from single atoms: at time t_0, a single atom is trapped from the background, causing the counts to jump from the background level C_0 to C_1; at time t_1, a second atom is added to the trap, causing another jump in the fluorescence signal. The atoms stay in the trap for a time period $[t_1, t_2]$ and both exit the trap at t_2, presumably because of collision with the background atoms, as discussed in Section 3.2.

As mentioned in Section 3.2, if there is only one step in the trace, indicating only one atom in the trap when the trap is on (as in Figs. 3.10(a) and 3.11(a)), the duration of these steps (τ_{on}) should be exponentially distributed with its mean equal to the inverse of the collisional loss rate L, or $\bar{\tau}_{\text{on}} \approx 0.6$ s for our experimental condition, according to Eq. (3.17)[1]. From a quick observation of Figs. 3.10(a) and 3.11(a), one can conclude that this prediction agrees with our experimental data. For a more careful analysis, the distribution of τ_{on} is tabulated from data in a long record of which Fig. 3.10(a) is but one segment, and the result is plotted in Fig. 3.12. From Fig. 3.12 we see that the on-time distribution fits roughly to an exponential curve with time constant $\tau'_{\text{on}} \approx 0.9$ s.

Likewise, the distribution of dwell times τ_{off} between two successive jumps of the fluorescence should also be exponential with its mean being the inverse of the filling rate R. However, a distribution curve similar to Fig. 3.12 is difficult to construct because in the limit of $\bar{n}_{ss} = \tau_{\text{on}}/\tau_{\text{off}} \ll 1$, we have $\tau_{\text{off}} \gg \tau_{\text{on}}$. For τ_{on} close to one

[1]If the trace contains more than one level of steps caused by trapping of more than one atom, (e.g., Fig. 3.10(b) and Fig. 3.11(b) contain steps caused by a two-atom trap), one has to analyze the distribution for the duration of steps at each level. Such an analysis is difficult both theoretically and experimentally, because theoretically, the probability distribution for a particular level of step depends on the history leading to such a level and one has to keep track of the time each atom enters and leaves the trap and sum over such a history, and experimentally, it takes a long time to collect statistically significant data.

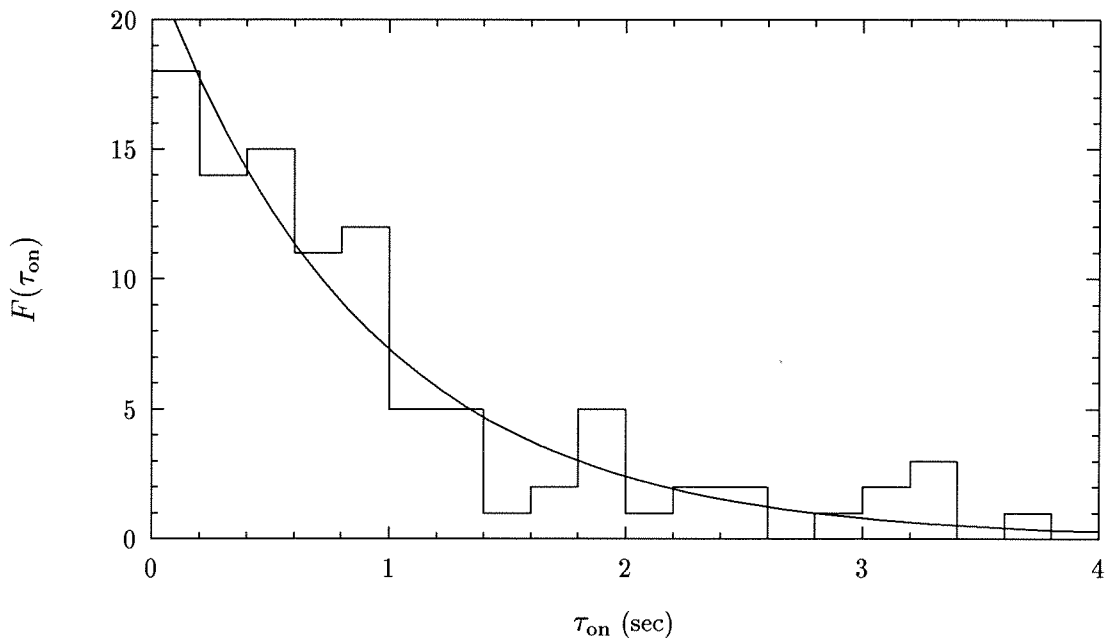

Figure 3.12: The distribution $F(\tau_{on})$ for the trap's on-time τ_{on}. The time is divided into bins of size 0.2 sec. The curve is for $F(\tau_{on}) = (n_{bin}/\tau'_{on}) \exp(-\tau_{on}/\tau'_{on})$, where $\tau'_{on} = 0.9$ s and $n_{bin} = 20$ is the total number of bins.

second according to Fig. 3.12, τ_{off} has a mean of several seconds. Thus to accumulate statistically significant data, one would have to wait for a time long enough that the experimental conditions are changed somewhat, since we are in the transition period and the pressure in the chamber decays with a time constant of several hours (Section 3.3.3). Nevertheless, from Fig. 3.10(a), we can make an order-of-magnitude estimate for τ_{off} to be $\tau_{\text{off}} \sim 10$ s, which is consistent with Eq. (3.14), since we later calculated in Fig. 3.13(a) that $\bar{n}_{ss} = 0.1$. This implies that $n_{\text{Cs}} \approx 20 \sim 50$ /cm^3 or $p_{\text{Cs}} \sim 2 \times 10^{-16}$ torr, according to Eq. (3.24).

Next we turn to the actual magnitude N_1 of the jumps in fluorescence associated with a single trapped atom, which is given by Eq. (3.23) as $0.9 \times 10^3 \lesssim N_1 \lesssim 1.6 \times 10^3$ counts for $\Delta t = 0.1$ s. From Fig. 3.10(a) (and confirmed by the histogram analysis discussed below) we observe that the theoretical prediction is a factor $3 \sim 4$ times larger than the experimental data suggested in Fig. 3.10(a) ($N_1 = C_1 - C_0$). A possible source for this large discrepancy is a potential mismatch between the size of the trap image and of the active area of the APD, which we estimate reduces the expectation for N_1 by roughly a factor of 2. Another possible cause for this discrepancy is that the trap may not have been well centered with respect to the intersection of the trapping beams. Again, since we have no imaging capability in the photon-counting regime, it may be that the actual intensity at the trap site is lower than that given by the peak intensity of the five trapping beams. These and other possibilities are currently being investigated, e.g., the purchase of the intensified CCD camera will permit us to take image of a single atom. A more efficient collection system based on aspherical lens is also under development.

Finally, to get a quantitative picture, we have constructed from traces as in Fig. 3.10, but from much longer time series, histograms of the frequency of occurrence of a given count rate versus count rate. On the graph we have also plotted Gaussian fits for the data. As we first focus on the experimental data, we can see that, at low pressure, as in Fig. 3.13(a), one sees predominantly two peaks, with the larger peak associated with the absence of trapped atoms ($n_{ss} = 0$), whereas the smaller peak corresponds to a jump in fluorescence with one trapped atom ($n_{ss} = 1$). At higher

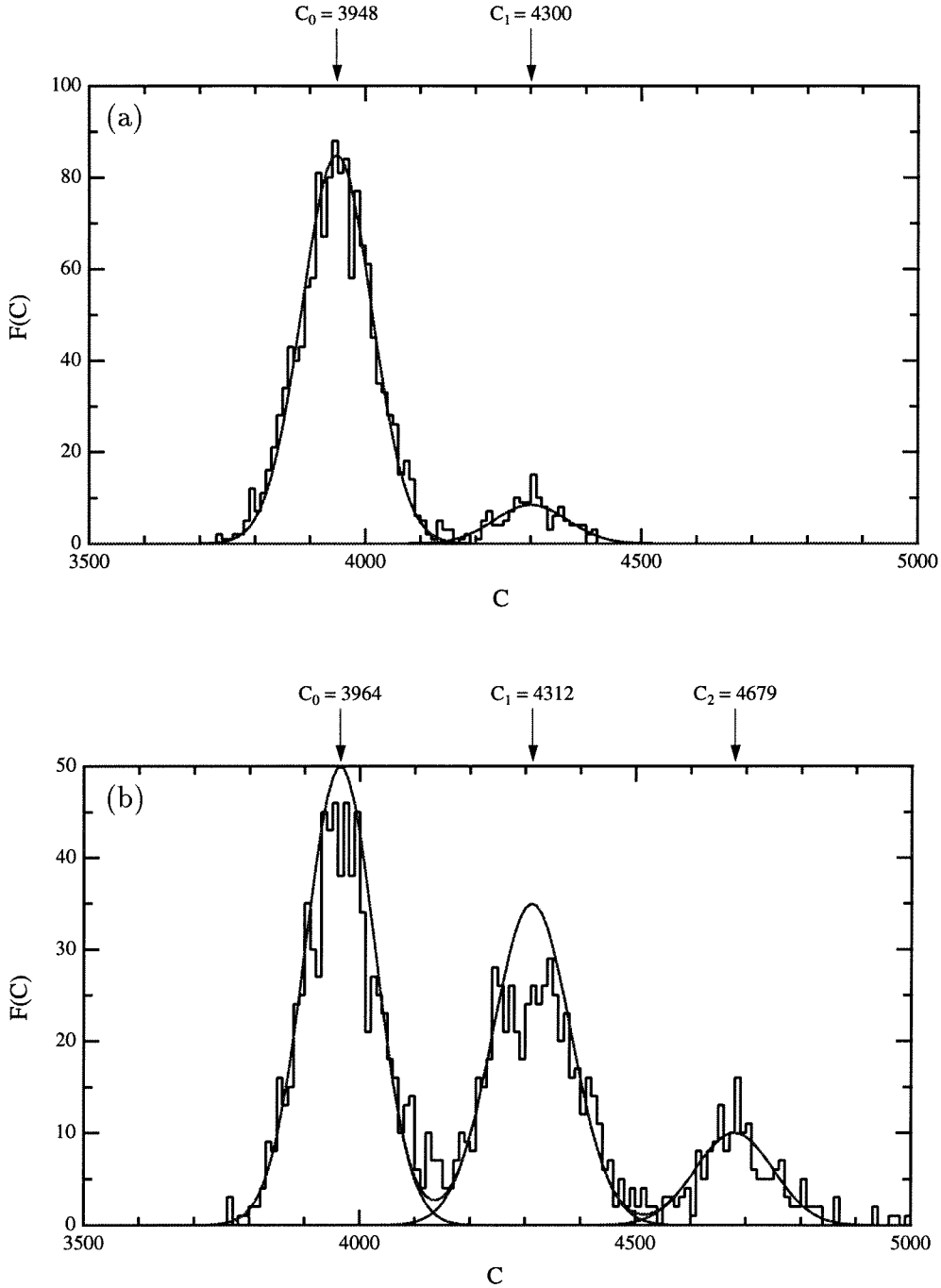

Figure 3.13: Histogram of the frequency of occurrence $F(C)$ of a given number of detected counts in 0.1-s interval. (a) Low Cs background pressure as in Fig. 3.10(a). (b) slightly higher pressure, as in Fig. 3.10(b). The arrows mark the counting levels C_0, C_1, C_2 associated with $n_{ss} = 0, 1, 2$ trapped atoms. The smooth curves are for $F(C) = 85\exp\left[-((C-3948)/63)^2/2\right] + 8.5\exp\left[-((C-4300)/66)^2/2\right]$ for (a) and $F(C) = 50\exp\left[-((C-3964)/63)^2/2\right] + 30\exp\left[-((C-4312)/70)^2/2\right] + 10\exp\left[-((C-4679)/70)^2/2\right]$ for (b).

background Cs density, as in Fig. 3.13(b), the relative weight of the $n_{ss} = 1$ peak increases, and a new peak corresponding to two trapped atoms emerges ($n_{ss} = 2$). By integrating the area under each peaks, we can also determine the average number of atoms in the trap for the particular graph. For example, for Fig. 3.13(a) we calculate that $\bar{n}_{ss} = 0.1$ while for Fig. 3.13(b), $\bar{n}_{ss} = 0.6$. Next as we focus on the smooth Gaussian curves, each individual curve is centered on C_i, where $(C_{i+1} - C_i)$ is the separation of the $N = 0, 1, 2$ peaks and is approximately constant, for example, in Fig. 3.13(b) we have $C_1 - C_0 = 348$ and $C_2 - C_1 = 367$, and for Fig. 3.13(a) we have $C_1 - C_0 = 352$. The relative height of the Gaussian peaks obey Poisson distribution (i.e., $1 : \bar{n}_{ss} : \bar{n}_{ss}^2/2 : \cdots$) with mean $\bar{n}_{ss}$. For example, in Fig. 3.13(a), where the mean number of atoms $\bar{n}_{ss} = 0.1$, the relative ratio for the height of the peaks corresponding to C_0 and C_1 is $10 : 1$. For Fig. 3.13(b), the mean number of atoms $\bar{n}_{ss} = 0.6$, and the ratio for the peak heights is $5 : 3 : 1$, which deviates slightly from Poisson distribution ($1 : 0.6 : 0.18$). Finally, the width of the peaks are close to the Poisson noise level $\sqrt{C_0}$ arising from the background counting rate, confirming our observation that the background scattering is the main contribution to the noise source. Efforts are in progress to reduce this background component and hence to resolve more clearly the individual peaks.

3.6 Further Developments

A number of straightforward improvements have already been discussed at various places throughout this chapter, e.g., the purchase of an intensified CCD camera will provide image capability even at single-atom level; an upgrade in vacuum will increase the dwell-times τ_{on} of the atoms in the trap; improvements of the optical system should lead to enhanced signal-to-noise ratio.

Besides these direct changes in the existing experiment, it is also interesting to explore other trapping schemes. For example, at the time being, there is a report that a single-atom trap has been observed in a cryogenic trap.[12] In a cryotrap the low background pressure (both p_{Cs} and p_{BG}) is accomplished by immersing the whole

vacuum system in a 4 °K environment. As a result, long lifetimes exceeding several hundred seconds are achieved.

Another variation is a Far-Off-Resonance-Trap (FORT).[21] A FORT is an optical dipole force atom trap which operates at very large detunings from atomic resonance. In order to produce appreciable trapping potential, given by[73, 74] $U = \hbar G^2/4\Delta$ for $\Delta \gg G$, the large detuning Δ is compensated by large intensities which is proportional to the square of Rabi frequency G. The advantage of large detuning is obvious: since the scatter rate $\Gamma = \gamma_\perp G^2/2\Delta^2$ falls quadratically as Δ^{-2}, ($1/\Delta$ faster than the potential), the atoms will have a very low spontaneous scattering rate and thus negligible photon recoil heating. The potential will closely approximate the ideal of a truly conservative trapping potential. Currently, a FORT based on our MOT is under development. Our initial result, shown in Fig. 3.14(b), is encouraging. A strong (5 W) laser beam from the output of a YAG laser (Quantronix A116, 1064 nm) is focused on the MOT with a 50 μm waist diameter, producing an intensity of 2.5×10^5 W/cm^2. Such an intense beam will induce a strong Stark effect and shift the MOT beams at 852 nm out of resonance. In order to get the photograph shown in Fig. 3.14(b), atoms are first loaded into the MOT using the usual trapping technique, then the MOT beams are turned off, the YAG beam is turned on [Fig. 3.14(c)], the atoms are loaded into the FORT. After a variable delay time, the FORT beam is turned off and the 852 nm beams turned on again, this time to probe the atoms remaining. From Fig. 3.14 we see that after about 400 ms, there are still an appreciable number of atoms left. That these atoms are not residual atoms from the MOT which have not had enough time to decay away in the 400 ms dark time is confirmed by the absence of such atoms when the YAG beam is not turned on during the 400 ms delay time. Neither are they captured by the 852 nm beams on their way to form another MOT, because the frequency of the 852 nm beams is switched from below atomic resonance to on resonance, and no longer meets the requirements of a positive detuning for a MOT. It would be interesting to ultimately combine this technique with our one-atom trap to form a single-atom FORT. This atom would have very limited movements both in real space (dictated by the waist of the FORT beam) and

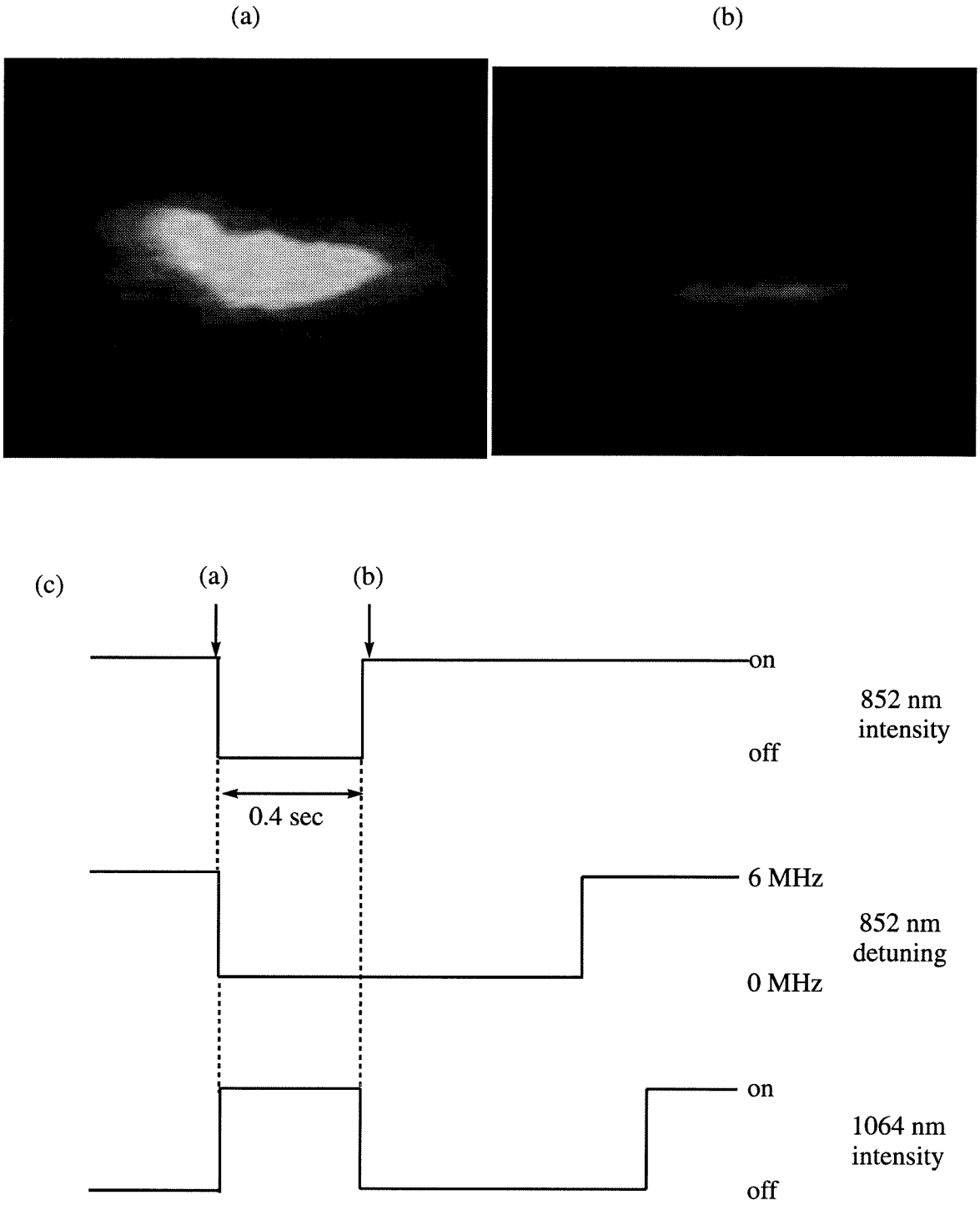

Figure 3.14: Image of a far-off-resonance trap (FORT). (a) Image of a MOT. (b) Image of a FORT. (c) The sequence for switching of the lasers. The time when (a) and (b) are taken is indicated by arrows. Note that the frequency of the 852 nm laser is switched from 6 MHz below the resonance to on resonance.

momentum space (dictated by the temperature of the atoms), thus approaching the ideal of a sample consisting of a single atom cooled to ultra-cold temperature and localized to within a wavelength of the optical field.

Another extension of our work on single-atom trap is to place this trap in a much larger magnetic field gradient in order to increase the ratio of resonance frequency of atomic oscillation $\omega_{\rm trap}$ to the damping rate $\tau_{\rm damp}^{-1}$ for motion in the trap. In its current configuration, this ratio is $2\omega_{\rm trap}\tau_{\rm damp} \sim 0.9$ for our trap [Eq. (2.13)]. By employing iron-boron magnets to increase the gradient dB/dz from its current value of 7 G/cm (Section 2.4) to values approaching 10^5 G/cm, we should be able to reach a regime of underdamped motion ($2\omega_{\rm trap}\tau_{\rm damp} > 1$) and hence to resolve the quantized energy spectrum for the dynamics. In preliminary work with rare earth permanent magnets, we have obtained field changes of 10^4 G on a mm scale. In this quantum domain a number of experiments are made possible by the external control of the system's parameters on a time scale much faster than the oscillation frequency $\omega_{\rm trap}$. For example, if the trapped atom could be cooled to zero point of its motion, then the sudden, nonadiabatic change of the trapping potential to shift the natural frequency of oscillation $\omega_{\rm trap}$ to $\omega'_{\rm trap}$ could be used to produce a squeezed state.[31, 32] Because this kind of experiment is conceptually simple, it may prove useful as a testing ground for topics in quantum measurement theory.

Chapter 4 Non-linear Spectroscopy of Trapped Atoms

In this and the next chapter we turn to the second topic of this thesis, which will deal with a different aspect of the physics with cold atoms, namely, the nonlinear spectroscopy of trapped atoms. Spectroscopy is now a ubiquitous tool for physicists and chemists. Great innovations based on spectroscopic techniques have changed our knowledge of the universe as well as our ways of living. The nascent field of atomic cooling and trapping have created new opportunity for spectroscopic measurements, because a dense collection of atoms, cooled and confined to a restricted region, is the ideal sample for spectroscopy that physicists dream of.

Among a wealth of opportunities for spectroscopic experiments made possible by the atomic cooling and trapping technique, in this chapter we will describe a somewhat modest attempt to characterize our trap by recording the transmission of a weak probe beam focused through the trap. In Section 4.1 we will first briefly describe our experimental setup, emphasizing the difference with the single-atom trapping experiment discussed in the previous chapter; and then present the results of our spectroscopic measurements. An explanation based on simple two-level theory is given in Section 4.2. But such a simple theory does not account for all the features of the spectrum. Section 4.3 discusses the implication of such a discrepancy to the general characteristics of our trap and prepares for the next chapter, in which we will theoretically explore a more complex regime — the three-level atom.

4.1 Experiment

The general principle and experimental setup for a magneto-optical trap is discussed in Chapter 2 and Chapter 3, where our experiment for single-atom trapping is de-

scribed. Our spectroscopy experiment precedes in time our single-atom experiment, and the scheme we employed there is similar to the latter. In this section we will only highlight the different arrangements between the two experiments.

The schematic for our spectroscopic experiment is shown in Fig. 4.1. The six trapping beams are derived from the main beam via a set of sheet beamsplitters and have a waist of $\omega_0 = 4$ mm. The beams are balanced by inserting suitable neutral-density filters in each beam's path. Although this method can only balance the beams' intensity to within 20% compared to the 5% of the more precise method employing polarization-beamsplitter-half-wave-plate assemblies, it gives satisfactory results for the purpose of our experiment, because under high numbers of atoms the trap is not very sensitive to the balance of the beams. The beams are further arranged into three counterpropagating pairs of opposite circular polarization propagating along mutually orthogonal directions and locked (using FM-saturation spectroscopy described in Section 2.3) to a common frequency several natural linewidths below the resonant transition of the Cs D_2 line ($6S_{1/2}, F = 4 \rightarrow 6P_{3/2}, F' = 5$ at 852 nm) to provide a dissipative cooling force. The spatially dependent trapping force is provided by the atomic Zeeman shift in an inhomogeneous magnetic field of gradient of 10 G/cm along z and 5 G/cm along (x,y) created by two current carrying coils, as described in Section 2.4. No measure is taken to offset the earth's magnetic field and other stray fields, e.g., that caused by the vacuum pump (Perkin Elmer Model 202-0125 ion pump, 2 l/s). This is improved in our later experiment for single-atom trapping by employing Helmholtz coils and ion pumps with smaller stray magnetic field (Section 2.4). A semiconductor laser diode which is locked to the Doppler profile recirculates population lost to the $F = 3$ ground state.

An important difference with our single-atom experiment is that our trap is loaded directly from Cs vapor in a quartz cell, as a result, the lowest achievable Cs pressure is only about 2×10^{-8} torr, resulting in a typical filling time of the trap following a sudden turn-on of the trapping laser to be about 1 sec, with the diameter of the steady-state cloud of the trapped Cs atoms to be about 1 mm. The temperature of the trapped atoms is near the Doppler cooling limit of 120 μK for Cs atom, as inferred

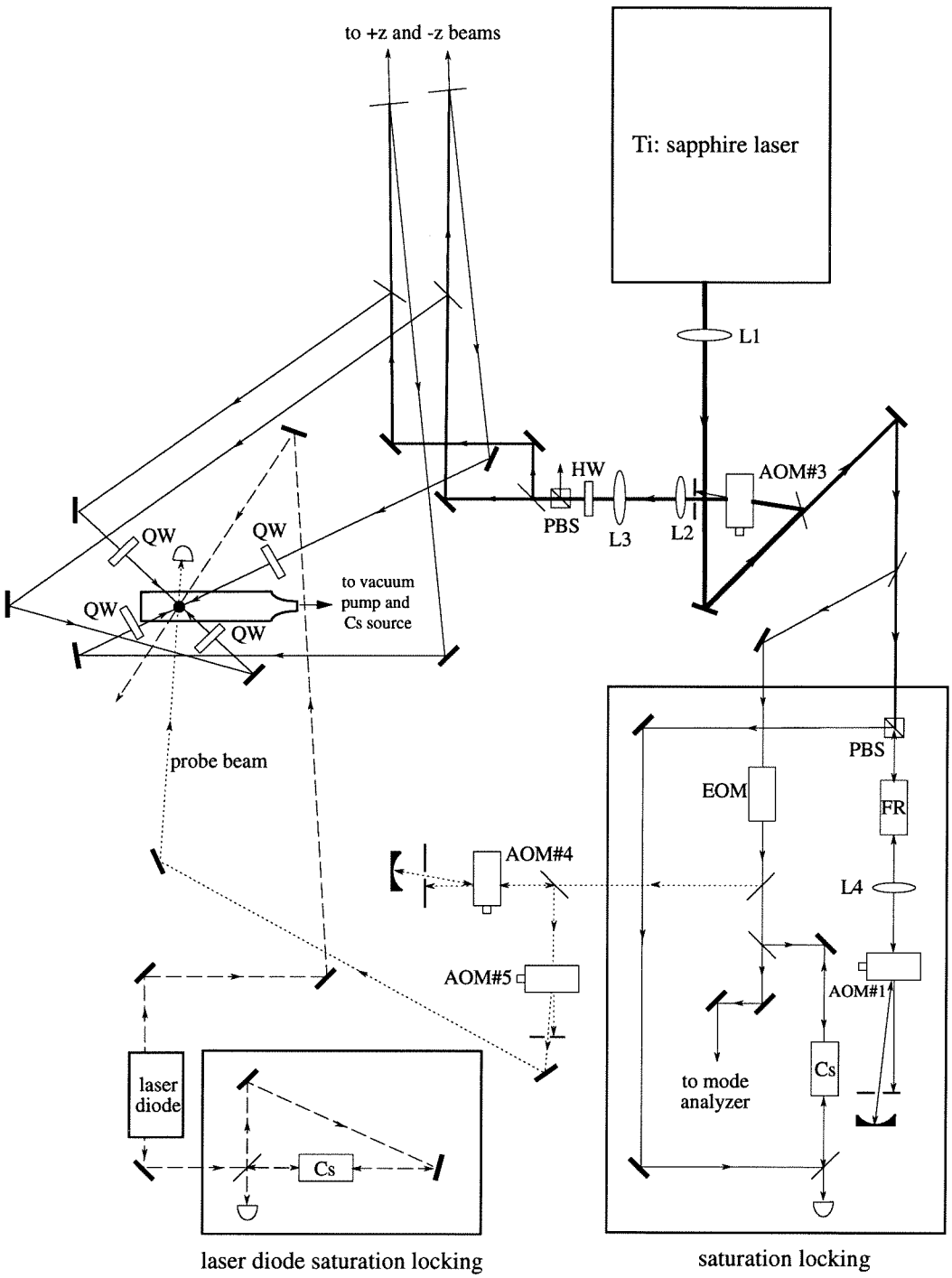

Figure 4.1: The experimental setup for the spectroscopic experiment. HW: half-wave plate; QW: quarter-wave plate; PBS: polarization beamsplitter; AOM#3 and saturation locking: see Section 2.3; Ti:sapphire laser (in solid line): see Section 2.2; laser diode (in dashed line) and laser diode saturation locking: see Section 2.5; probe beam (in dotted line), AOM#4 and AOM#5: see text; L2 and L3: telescope, see Section 2.5. L1: Newport KBX 088, $f = 100$ cm; z beams (not shown) propagate into and out of the page; mirrors and beamsplitters are not marked.

by monitoring the decay in absorption of a weak probe beam when the trapping lasers are chopped off.

In addition to these standard configurations for a magneto-optical trap, a probe beam is derived from the same Ti:sapphire laser for the trapping beams and is focused to a waist of about 100 μm and attenuated to a typical power of about 60 nW, resulting in an intensity of about 0.4 mW/cm^2, compared to the 1 mW/cm^2 saturation intensity for the Cs $6S_{1/2}, F = 4, m_F = 4 \rightarrow 6P_{3/2}, F' = 5, m_{F'} = 5$ transition. The probe beam is double passed through an acousto-optic-modulator AOM #4, which has a center frequency of 80 MHz and can be independently tuned over a frequency range of at least 70 MHz without significant beam steering. The resultant doubly upshifted beam is again passed through another AOM (AOM #5) with a fixed frequency of 40 MHz. The first-order beam downshifted by this AOM finally has the required frequency near the Cs D_2 transition.

Under conditions of strong excitation by the trapping lasers, the transmitted power of the weak probe beam as a function of the probe frequency ω_p is recorded and the result is shown in Fig. 4.2, which is a succession of records of the transmitted probe power normalized to the input probe power (p_1/p_0) versus ω_p, with the positions of the frequencies of the trapping laser ω_T and of the atomic transition ω_A indicated. As might be expected, we observe in Figs. 4.2(a) and 4.2(b) probe spectra with broad regions of absorption and amplification symmetrically placed about ω_T characteristic of the dressed-state splitting. However, in addition to the broad features, a narrow dispersive-shaped feature around ω_T is also clearly evident in Figs. 4.2(a) and 4.2(b). This narrow feature has width below the natural linewidth of $2\gamma_\perp/2\pi = 5$ MHz and can exhibit appreciable single-pass gain of more than 20%. An expanded view of the absorption spectrum is given in Figs. 4.2(c) – 4.2(e), where we see that for increasing levels of trapping power P_T, the dispersive shape broadens and develops substructure. The general trends shown in Fig. 4.2 are independent of the number of trapped atoms as well as of the direction of propagation of the probe beam relative to the trapping beams. However, the spectra do exhibit a dependence on the polarization state of the incident probe beam [especially as regards the substructure shown in Figs. 4.2(c)

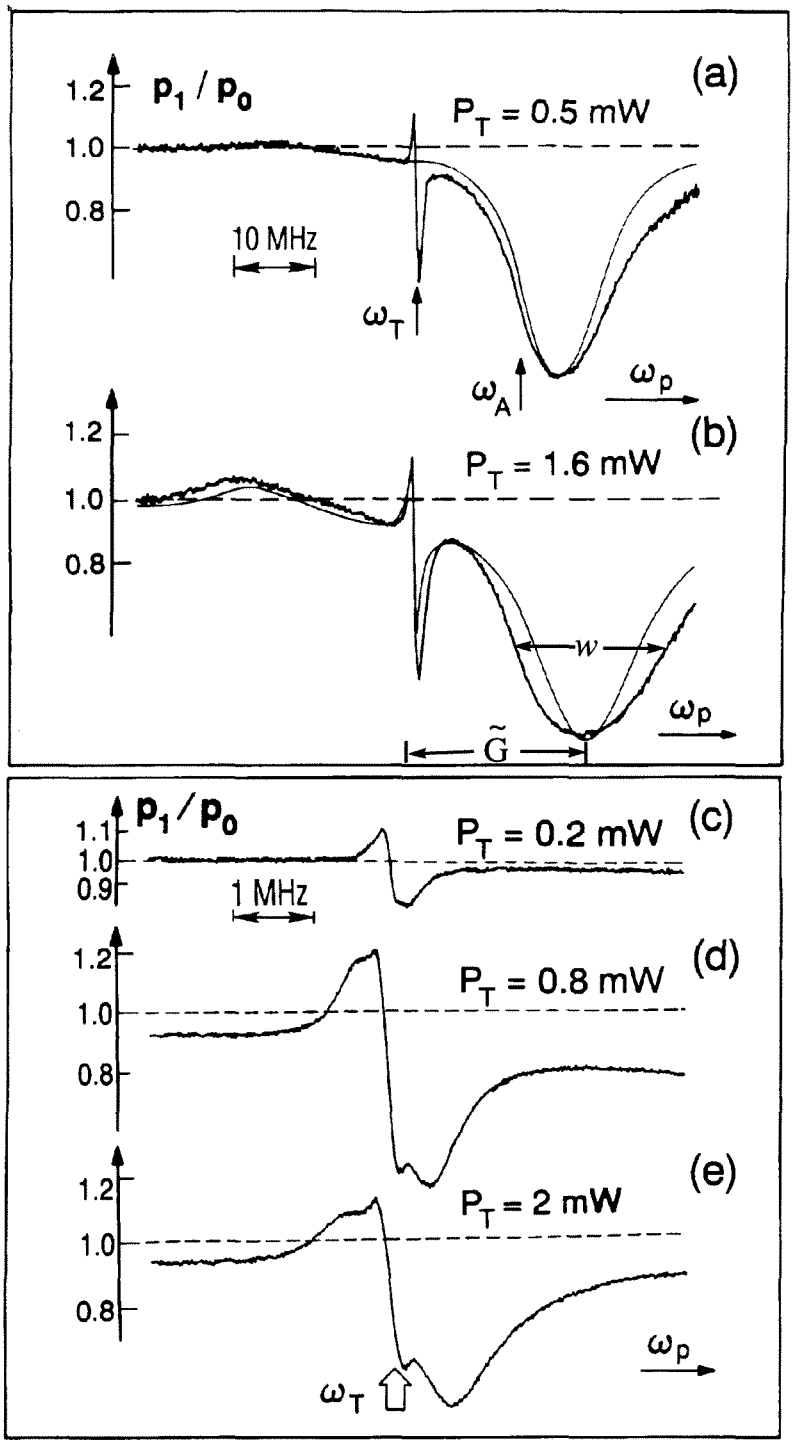

Figure 4.2: Probe absorption spectra p_1/p_0 versus probe frequency ω_p for $(\omega_A - \omega_T)/2\pi = 13.5$ MHz, after Ref. [14]. (a), (b) Scans showing large absorption near ω_A and small gain symmetrically placed about ω_T. (c) - (e) Magnified frequency scale to examine the narrow central feature near ω_T for various P_T. The finely drawn curves in (a) and (b) are discussed in Section 4.2.

– 4.2(e)] and on the magnetic-field gradient across the trap ($\Delta B \sim 1$ G gives a range $\Delta\omega_A/2\pi \sim 1$ MHz).

4.2 Explanation in Two-Level Theory

To model the spectra shown in Fig. 4.2, we can make some headway by first of all neglecting all the complexities in the energy level structure of the trapped Cs atoms and approximate it with a standard two-level system. Such a system is shown in Fig. 4.3(a).

The pump-probe spectroscopy of a standard two-level system was first studied by Ref. [75] and has since then become a textbook example for applying the quantum mechanical method to simple systems.[76] Its various extensions are extensively studied both theoretically and experimentally under numerous different contexts by a host of literatures.[77–82]. These are simply some limiting cases of the more general three-level results discussed in the next chapter. A detailed derivation of the two-level spectra is thus omitted since it is also out of the scope of this thesis. For the purpose here, it suffices to remind the reader that the probe-absorption spectra is different than the linear absorption spectra, or otherwise known as the lineshape, in the sense that the probe-absorption spectra is the transmission spectra for a weak probe in the presence of a possibly intense pumping beam. The role of the pump beam is to maintain a nonzero population in the excited state and thus reduce the difference of the population between the ground and excited state. In the limit of a weak pump, all the atoms are in the ground state, and the probe spectra is identical to the linear spectra which has a Lorentzian lineshape centered at atomic transition frequency $\omega_A = \omega_T + \Delta$ having a width $2\gamma_\perp$ equal to the natural linewidth of the transition. As the pump intensity is increased, the population difference between the ground and excited states is diminished as the excited state gains more population and the atoms become saturated. Such an atom has less ability to absorb any more photons and the peak absorption, characterized by the depth of the Lorentzian lineshape, is decreased, as shown in Fig. 4.3(c). Another trend with the increasing pump

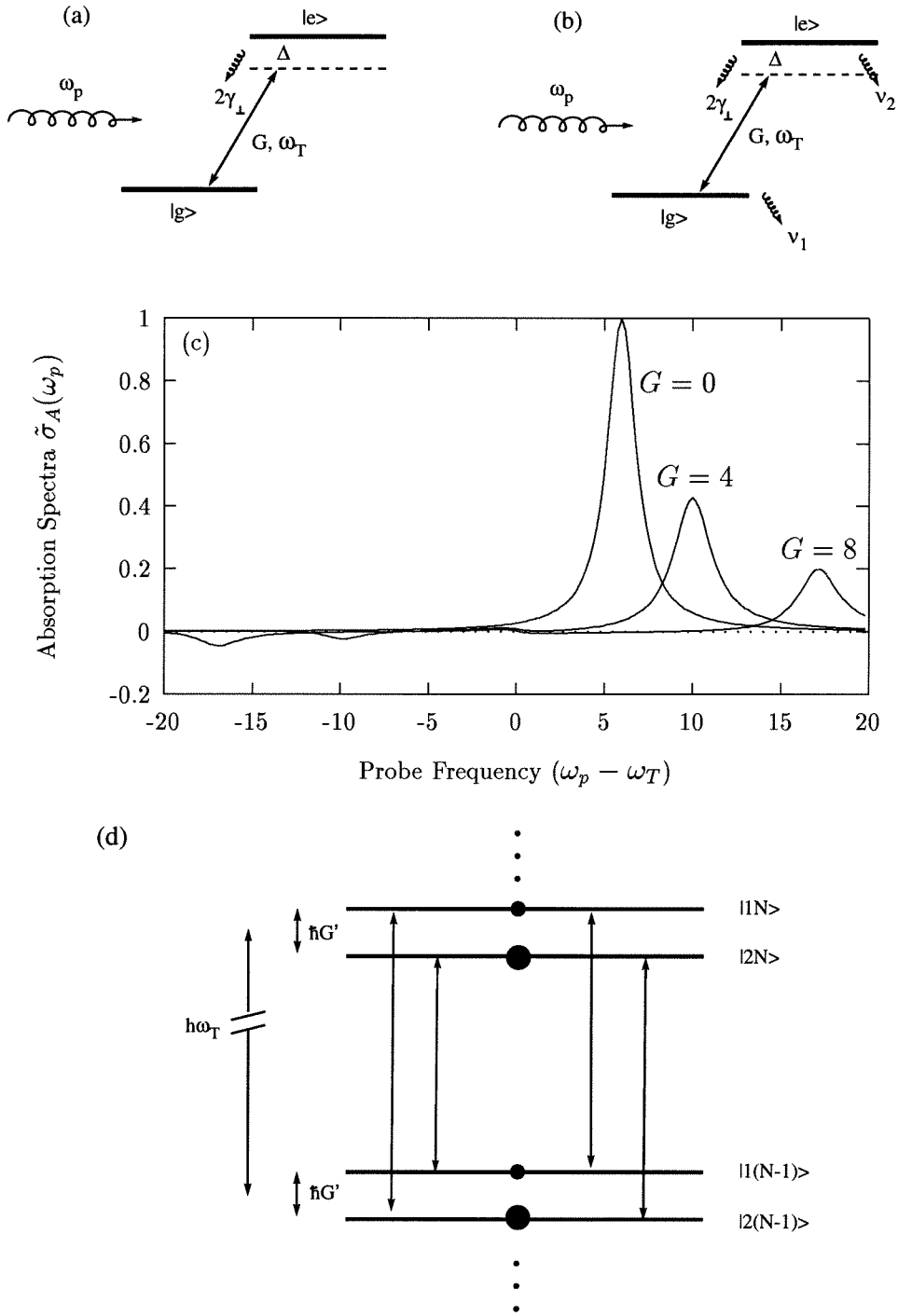

Figure 4.3: Two-level atoms and their absorption spectra. (a) A standard two-level atom having Rabi frequency G, detuning Δ, spontaneous emission rates $2\gamma_\perp$, probed by laser beam of frequency ω_p. (b) A "leaky" open two-level atom with external decay rates ν_1 and ν_2. (c) Absorption spectra of a two-level atom with parameters $\gamma_\perp = 1$, $\Delta = 6$ and $G = 0, 4, 8$. The definition of these quantities are found in the next chapter. Note that the negative values for $\tilde{\sigma}_A$ corresponds to gain. (d) Dressed states for a two-level atom.

intensity is that the center of the Lorentzian peak shifted from position $\omega_T + \Delta$ to $\omega_T + G'$, where $G'^2 = G^2 + (\Delta/\gamma_\perp)^2$ is the generalized Rabi frequency. Interestingly, the probe can exhibit gain when the probe frequency is tuned to $\omega_p = \omega_T - G'$, i.e., opposite to the broad absorption peak. This can be explained by the dressed states of a two-level atom interacting with an electromagnetic field,[76, 83] as shown in Fig. 4.3(d). Under the presence of an external field, the eigenstates of the combined laser-atom system forms an infinite series of manifolds, each consisting of a doublet whose energy levels are separated by $\hbar G'$. Each doublet is a mixture of the ground and excited states, with the mixing angle determined by the laser field. From the quasi-steady-state populations shown in Fig. 4.3(d), one immediately understands that the transition $|\, 1(N)\rangle \leftrightarrow |\, 2(N-1)\rangle$ (of frequency $\omega_T + G'$) is absorbing because the lower level is more populated than the upper level. On the other hand, the transition $|\, 2(N)\rangle \leftrightarrow |\, 1(N-1)\rangle$ (with frequency $\omega_T - G'$) is amplifying because the upper level is more populated than the lower level. This gain in the probe comes from the process of transferring photons from the pump beam into the probe beam, which is more commonly known as the stimulated emission process. Finally, the two transitions $|\, i(N)\rangle \leftrightarrow |\, i(N-1)\rangle$ with $i = 1, 2$ (with frequency ω_T) do not result in any amplification or absorption because they connect equally populated levels.

The results in Fig. 4.3(c) show that the standard two-level theory already agrees qualitatively with the experiment exclusive of the narrow feature. To carry this analysis one step further, we may try to account for the multiplicity of Zeeman transitions with a crude adaptation of the standard two-state result. Our approach is to average absorption spectra for a weak probe over the distribution of dipole moments for the $F = 4 \rightarrow F' = 5$ transition in Cs. As indicated by the finely drawn curve in Fig. 4.2(a), the agreement between this calculation and the experiment is qualitatively reasonable for the broad absorption and gain feature. But our naïve average over the Zeeman sublevels still does not account for the central narrow feature. For the broad feature, we present in Fig. 4.4 a compilation of results such as in Fig. 4.2(a) over a range of trapping power $0 \leq P_T \leq 3$ mW. With regard to the splitting $\tilde{G}$ between ω_T and the broad absorption feature, we find that the average over Zeeman

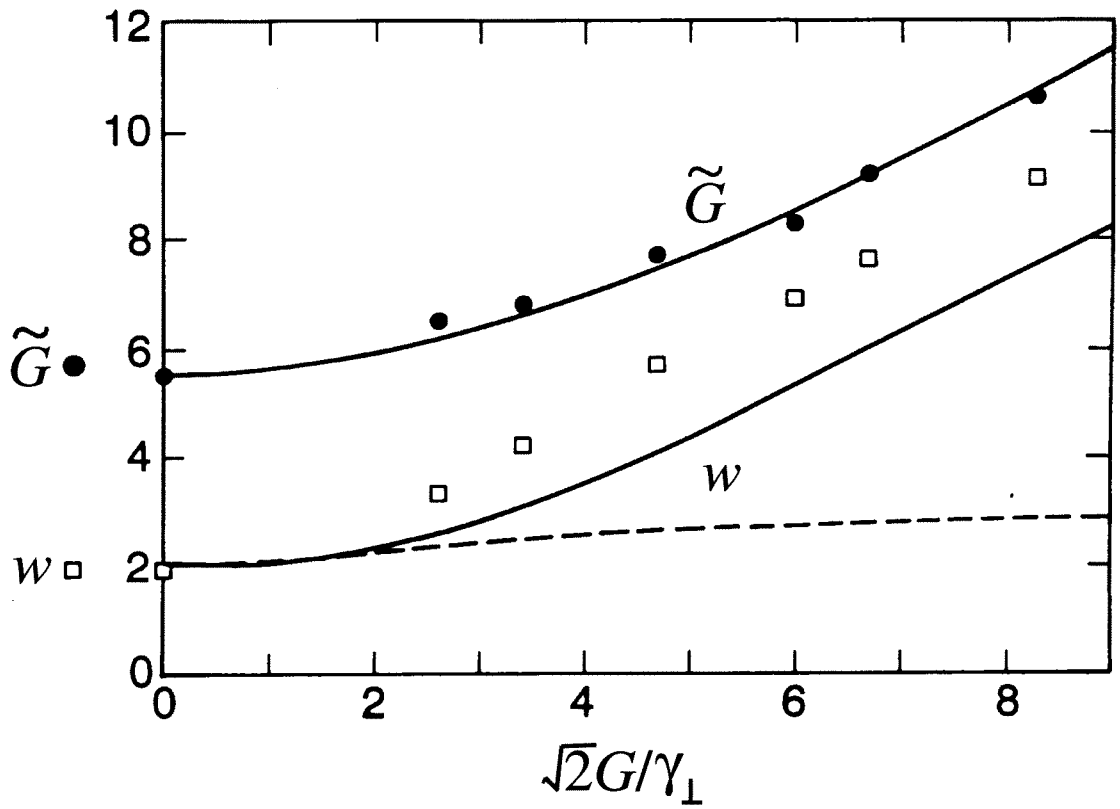

Figure 4.4: Frequency splitting $\tilde{G}$ (•) and width w (□) of the broad absorption feature versus Rabi frequency G of trapping beams for $(\omega_A - \omega_T)/2\pi = 13.5$ MHz, after Ref. [14]. Theoretical curves for $\tilde{G}$ and w are from an average for $F = 4 \rightarrow F' = 5$. The dashed curve gives w for the single two-state transition; a similar curve for $\tilde{G}$ would roughly overlay the multistate result. The normalization for $\tilde{G}$ and w is $\gamma_\perp/2\pi = 2.5$ MHz; and G is defined in Eq. (5.67).

sublevels does not produce significant departures from the two-level result. By contrast, the large spread in Clebsch-Gordan coefficients within the $F = 4 \rightarrow F' = 5$ manifold results in a broadening that substantially increases the width w above the two-level result for both the experimental scans and the calculation. That this excess width does not arise from heating of the trap with increasing P_T has been established with measurements both of the transient decay of the trap and of the probe spectrum with a chopping technique that leads to the points for $(\tilde{G}, w)$ at $G = 0$. Note that in Fig. 4.4, the horizontal axis is normalized to the saturation intensity of the $m_F = 4 \rightarrow m'_F = 5$ transition with $\sqrt{2}G/\gamma_\perp = 1$ for $I = 1$ mW/cm^2, where $I = 6I_T$ and $I_T = 2P_T/\pi\omega_0^2$. The set of theoretical Rabi frequencies has been scaled by $a = 0.85$ $(G \rightarrow aG)$ to optimize the comparison.

If we next consider the narrow central feature near ω_T, we might attempt to account for the rather complex optical pumping processes within the manifold of Zeeman states with an extension of the usual two-level calculation to include relaxation to and from neighboring Zeeman transitions. Such a system, shown in Fig. 4.3(b), is characterized by the external decay rates ν_1 and ν_2. As opposed to our previous summation, such an approach for an "open" two-state offers the possibility for describing certain dynamical aspects of the problem, as for example, the differential rate of relaxation of ground and excited-state populations.[80–82] Unfortunately, the spectrum for the open two-level system exhibits either very small central features of the same symmetry as in Figs. 4.2(a)-(e) or larger features of size comparable to our data but of opposite symmetry.[81] Fortunately, a generalization of the open two-level model to multilevel systems that do not conserve alignment or orientation finds the possibility for reversals in sign of narrow resonances.[82(a)] If we follow this lead and make an otherwise *ad hoc* change of sign in the terms responsible for the narrow feature (Eq. (4) of Ref. [81]), we obtain surprisingly good agreement between the resulting analytic expression and our spectra as evidenced by the comparison in Fig. 4.2(b), for which the external decay rates of the ground state and excited states are $\nu_1/\gamma_\perp = 0.4$ and $\nu_2/\gamma_\perp = 1.2$. Although this circumstance might simply be a curiosity, recent theoretical work[80, 82(b)] may provide an acceptable justification

for what is otherwise simply a fitting function.

4.3 Conclusion

In this chapter, we have described an investigation of the nonlinear spectroscopy of Cs atoms cooled and confined in a magneto-optical trap. While the broad absorption and gain features agree reasonably well with the two-level theory, a narrow dispersive central feature whose width is below the natural linewidth of the transition is also observed with single pass gains exceeding 20%. Such a spectrum, together with the narrow feature which is not accounted for in the simple two-level theory, is also observed and reported in Ref. [84] and explained in the context of Raman transition. To fully understand the absorption spectra will likely require a complex treatment of all the relevant Cs levels together with the microscopic environment. This would certainly be a formidable task, and such an approach[85] might make it difficult to understand the underlying physical meaning. In the next chapter, we will instead attempt to use a relatively simple three-level model to explain partly the spectrum we have described in this chapter.

Not surprisingly then, our measurements of absorption spectra bring us full circle back to the difficult question of the self-consistent relationship between the spectroscopic and mechanical characteristics of the trap. To begin to address this issue, we present in Fig. 4.5 a series of images that illustrate a correlation between the narrow spectral resonances and the morphology of the trap. Fig. 4.5(a) is a relatively symmetric picture of the trapped cloud of Cs atoms in the absence of the probe beam. In Fig. 4.5(b) the probe beam is present and is tuned for absorption in the narrow feature in Fig. 4.2. In this case the atoms in the trap recoil along the direction of propagation of probe beam (stimulated absorption resulting in positive radiation pressure). In Fig. 4.5(c) the probe frequency is tuned into the region of gain in the subnatural profile, with the result that the atoms in the trap recoil opposite to the direction of propagation of the probe beam (stimulated emission resulting in "negative" radiation pressure). Among the various applications that these images suggest,

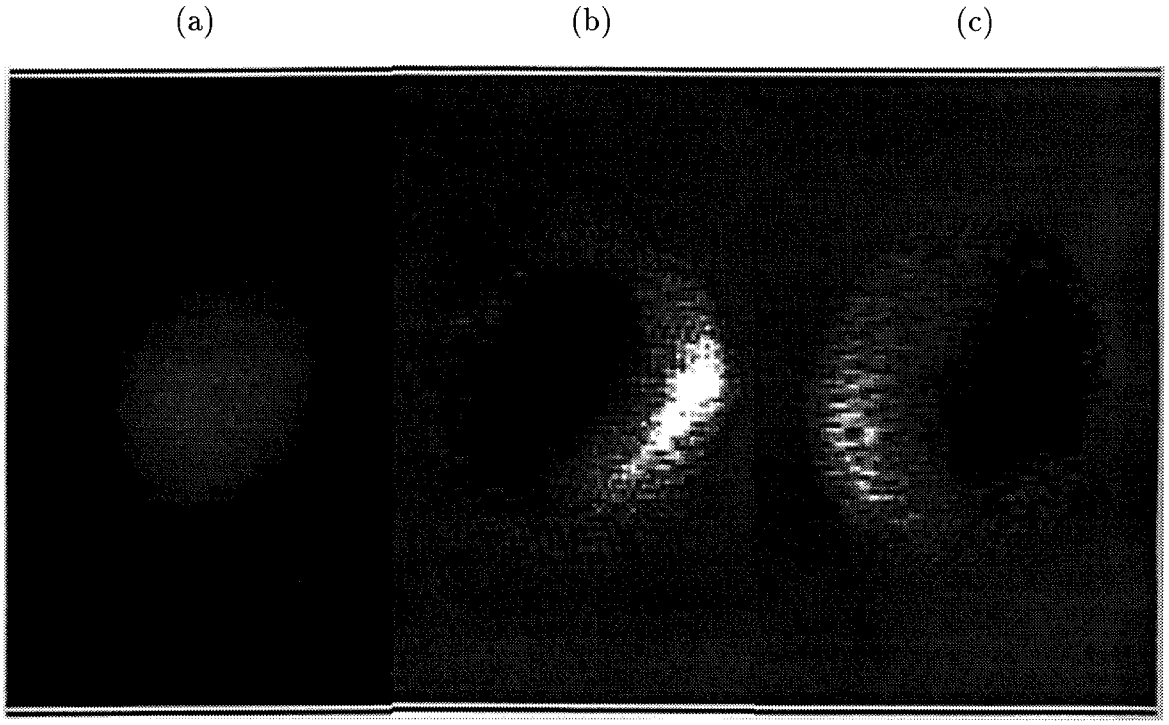

Figure 4.5: Images of trapped Cs atoms viewed from $[1\bar{1}0]$ direction [Fig. 2.2(a)], after Ref. [14]. (a) Trap in the absence of the probe beam with radius $R \sim 0.4$ mm. (b), (c) Trap with probe beam propagating from left to right and into the page by about 25° (along [130] direction). (b) Probe detuning $(\omega_p - \omega_T)/2\pi \simeq +0.3$ MHz, with recoil along the direction of probe propagation (absorption). (c) Probe detuning $(\omega_p - \omega_T)/2\pi \simeq -0.3$ MHz, with recoil opposite to the direction of probe propagation (gain). In (b) and (c), the images shown are the difference between (a) and the corresponding image in the presence of the probe beam, with light (dark) indicating an increase (decrease) in atomic fluorescence. The probe intensity I_p for Fig. 4.5 is about 4 mW/cm^2, while Fig. 4.2 is taken with I_p below 0.4 mW/cm^2 so that the spectra are independent of probe power and do not exhibit such large recoil.

one is a technique for measuring the trap parameters based upon modulation of the probe p_0 at frequency ν while an image of the trap is monitored in fluorescence S with a split photodetector, resulting in the (spatially resolved) trap transfer function $S(\nu)/p_0(\nu)$. (This open-loop response could even be "closed" for active servo control of the trap.)

Beyond the discussion for our particular trapping configuration, the images in Fig. 4.5 together with more general calculations of absorption spectra also suggest new mechanisms for dramatically altering the trap itself. For example, in an optically dense sample conventional radiation pressure leads to a long-range repulsive force between atoms [recoil away from the source as in Fig. 4.5(b)].[58] If however, the absorption cross section for scattered photons could be made negative, then a long-range attractive force between atoms would arise[recoil toward the radiation source as in Fig. 4.5(c)]. While in Fig. 4.2 the absorption cross section $\sigma_A(\omega_p)$ is evidently negative (gain) only over small frequency intervals, recent work has described the possibility of probe gain over the entire frequency range of atomic response in a three-level system.[86] In the next chapter we will identify such a system and explain how the negative radiation pressure accompanying a negative absorption cross section will lead to a long range attractive force which might be employed for optical implosion of the sample.[87]

In addition to these possibilities, experimental advances along the avenues suggested by these spectra include observations of quantized motions in both Rb atoms (by high resolution spectroscopy of resonance fluorescence)[88] and Cs atoms (by Raman spectroscopy of optical molasses)[89], and a "cold atom laser"[37], which operates on the narrow gain feature of the trapped atoms and has achieved a modest power of $\sim$60 nW. Such a laser is important in the study of quantum properties of Raman lasers,[29, 30, 90] which is a candidate for generating highly sub-Poissonian light having spectral linewidth well below the Schawlow-Townes limit and intensity fluctuations below the shot noise level.

Chapter 5 Absorption and Emission Spectrum of a Three-Level Atom

5.1 Introduction

In the previous chapter, we have used a two-level system to explain the pump-probe spectroscopy of a dense sample of Cs atoms trapped in a magneto-optical trap. Such a model could only account for the broad absorption and gain features of the spectrum. To explain the central dispersive narrow feature, we need to go one step further. A natural extension of the two-level system is the three-level system, which includes the Λ, Ξ and V configurations. It is not surprising that a three-level system can exhibit narrow resonances because the width of the narrow resonances with width below the natural linewidth, because such a narrow width could come in through other avenues, such as ground state splitting of a Λ system. Our interest in three-level atoms is also driven by the recent discovery that the absorption spectrum of a three-level system could exhibit gain over the entire frequency range.[86] This anomaly in the spectrum would not occur in a two-level system because the steady-state population of a two-level atom could never be inverted. This could have profound implication for the radiation pressure force we introduced by the end of previous chapter, because the radiation pressure force is closely related to the integral of the absorption spectrum (weighed by emission spectrum).

Historically, ever since the experimental techniques have grown beyond the sophistication of a two-level system, thanks mainly to the invention and widespread application of frequency stabilized lasers to atomic and molecular physics, the three-level system has been the platform of many interesting experimental phenomena, such as the optical double resonance[91], two-photon spectroscopy, and optical pumping. Recently there has been a resurgence of interest in three-level systems mainly be-

cause of the explosion in the field of atomic cooling and trapping. Three-level atoms have been proposed to be the candidate in which to observe such exotic behaviors as lasing without inversion[92], coherent population trapping[93], linewidth reduction in the fluorescent spectrum[86], and most recently, generation of Fock states and coherent superposition states ("Schrödinger's cat" states)[94]. It has also been suggested that three-level forces may explain some of the differences between observation of real trapped atoms and predictions for two-level atoms or incoherent processes in multilevel atoms[95].

Motivated by these rich and interesting features of a three-level system, in this chapter we attempt to investigate the absorption and emission spectrum of a three-level atom driven by two intense optical fields. Our notation for the atom-field system is defined in Section 5.2, where an outline of our approach is also given. In Sections 5.3 - 5.6 we derive the master equation for the density matrix of a three-level Λ system and apply the quantum regression theorem in Laplace space to obtain the formulae for the spectrum. Section 5.7 extends our results to the Ξ and V system and key formulae and equations are listed. After explaining how to understand the parameters used in our theoretical derivation in terms of experimental observables (Section 5.8), we present the results of our calculation in Section 5.9, emphasizing the narrow feature and negative radiation pressure that is not present in a two-level system.

5.2 Overview

The framework of our discussion in this section is shown in Fig. 5.1, where the three different configurations of the three-level system, i.e., Λ, V, and Ξ systems, are illustrated. The atomic levels 2 and 3 are optically connected to level 1 via the spontaneous decay rates[1] $2\gamma_1$ and $2\gamma_2$. The transition between levels $1 \leftrightarrow 3$ and levels $1 \leftrightarrow 2$ are

[1]Here γ_1 and γ_2 are the "transverse" decay rates for the radiation, which is equivalent to $\gamma_\perp$ we introduced in two-level system. We have assumed pure "radiative decay" $\gamma_\parallel = 2\gamma_\perp$ throughout the thesis.

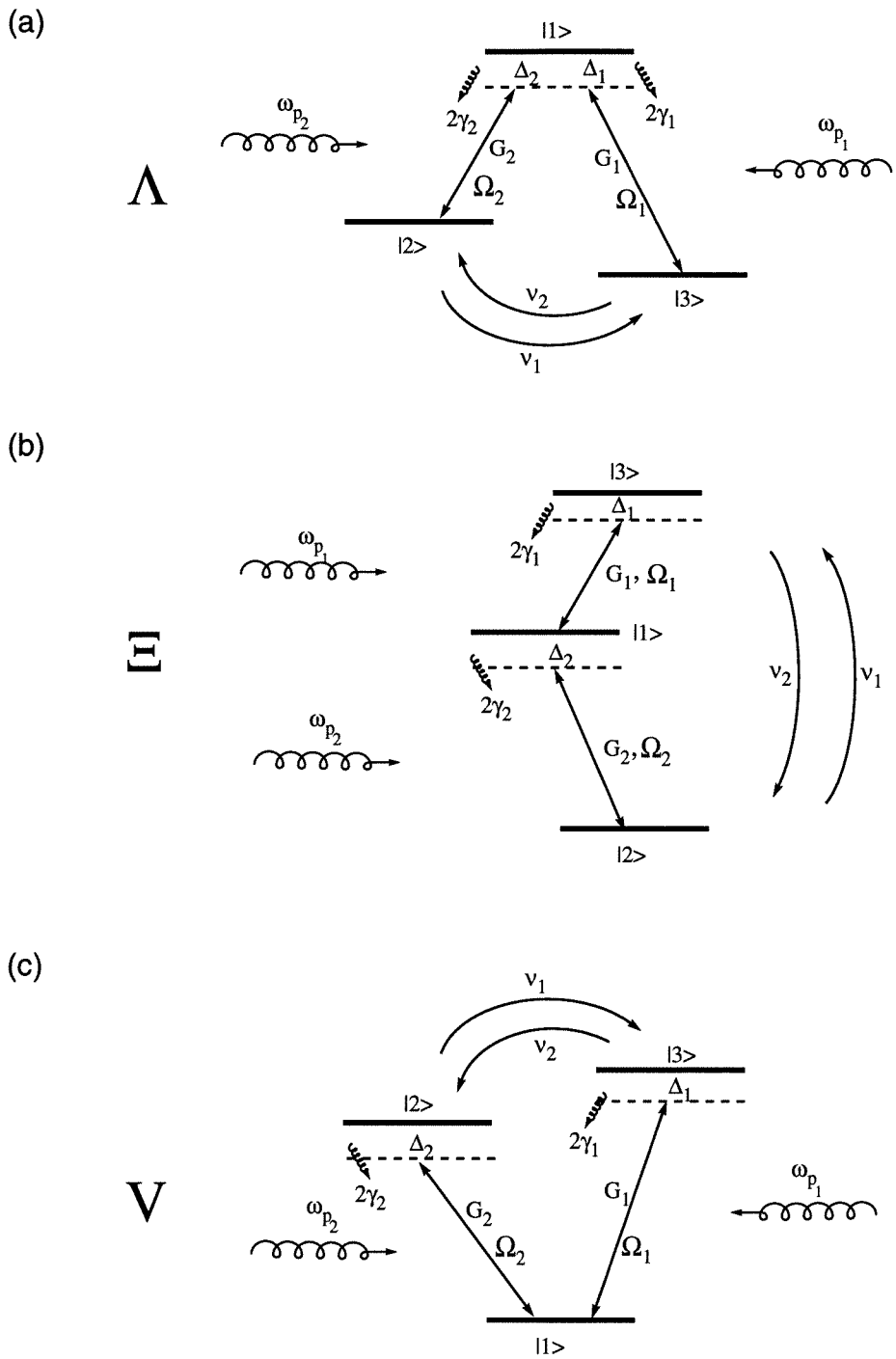

Figure 5.1: The three-level Λ, V, and Ξ configuration. Ω_1, Ω_2: frequencies of the driving fields; G_1, G_2: Rabi frequencies of the driving fields; Δ_1, Δ_2: detunings of the pump beams; $2\gamma_1$, $2\gamma_2$: spontaneous emission rates of transitions $1 \leftrightarrow 3$ and $1 \leftrightarrow 2$; ν_1, ν_2: population transfer rates between levels 2 and 3. ω_{p_1}, ω_{p_2}: frequencies of the probe beams.

driven by two electro-magnetic fields of frequency Ω_1 and Ω_2, whose amplitudes are characterized by the two Rabi frequencies G_1 and G_2, respectively. There is no field driving the transition $2 \leftrightarrow 3$, but they can relax via the rates ν_1 and ν_2, as shown in Fig. 5.1. The atomic transition frequencies between levels $1 \leftrightarrow 3$ and levels $1 \leftrightarrow 2$, i.e., $|\omega_{13}| = |\epsilon_1 - \epsilon_3|/\hbar$ and $|\omega_{12}| = |\epsilon_1 - \epsilon_2|/\hbar$ (where ϵ_1, ϵ_2 and ϵ_3 are the individual energy levels for the unperturbed states) and the field frequencies Ω_1 and Ω_2 do not enter our final equation[2] because our system is characterized by the detunings $\Delta_1 = |\omega_{13}| - \Omega_1$ and $\Delta_2 = |\omega_{12}| - \Omega_2$. Thus, our spectra can be completely determined by the following 8 parameters: the Rabi frequencies G_1 and G_2, the detunings Δ_1 and Δ_2, the spontaneous decay rates $2\gamma_1$ and $2\gamma_2$ and the relaxation rates between levels 2 and 3: ν_1 and ν_2. With very few exceptions, the subscript "1" refers to transition $1 \leftrightarrow 3$ and "2" refers to transition $1 \leftrightarrow 2$.

In the text that follows, we will take the Λ system as an example to illustrate our procedure for calculating the three-level emission and absorption spectra. Similar techniques apply to the V and Ξ systems, and the results are summarized in Section 5.7.

To calculate the emission and absorption spectra, we will need the field correlation function:

$$G^{(1)}(t+\tau, \tau) = \langle \hat{\mathbf{E}}^{(-)}(t+\tau) \cdot \hat{\mathbf{E}}^{(+)}(\tau) \rangle, \tag{5.1}$$

where the scattered field $\hat{\mathbf{E}} = \hat{\mathbf{E}}^{(+)} + \hat{\mathbf{E}}^{(-)}$ takes the form in the far field:

$$\hat{\mathbf{E}}^{(+)}(\mathbf{r}, t) = \hat{\mathbf{E}}_0^{(+)}(\mathbf{r}, t) - \frac{\omega_0^2}{c^2 r} \hat{\mathbf{n}} \times (\hat{\mathbf{n}} \times \hat{\mathbf{d}}) \hat{P}^{(+)} \left(t - \frac{r}{c} \right). \tag{5.2a}$$

$$\hat{\mathbf{E}}^{(-)}(\mathbf{r}, t) = \left(\hat{\mathbf{E}}^{(+)}(\mathbf{r}, t) \right)^{\dagger}. \tag{5.2b}$$

Here $\hat{\mathbf{E}}^{(+)}$ and $\hat{\mathbf{E}}^{(-)}$ are the positive and negative part of the total field operator $\hat{\mathbf{E}}$, respectively, $\hat{\mathbf{E}}_0^{(+)}$ and $\hat{\mathbf{E}}_0^{(-)}$ are the corresponding solution of the homogeneous wave equation, $\hat{P}^{(+)}$ and $\hat{P}^{(-)}$ are the positive and negative frequency part of the atomic

[2]Note that we have used ω_A and ω_T for the frequencies of the atomic transition and the driving field in the previous chapter for a two-level system.

polarization operator $\hat{P}$ whose complete form is given in Eqs. (5.27) and (5.28), and $\hat{\mathbf{n}}$ and $\hat{\mathbf{d}}$ are unit vectors in the direction of observation and along the atomic dipole moment, respectively. Away from the forward direction, the field and the atomic polarization operators are directly proportional to each other for normally ordered quantities. Hence, we only need to limit our considerations to the atomic correlation function:

$$\Gamma^{(1)}(t+\tau,\tau) = \langle \hat{P}^{(-)}(t+\tau)\hat{P}^{(+)}(\tau)\rangle. \tag{5.3}$$

The Fourier transform of Eq. (5.3) is proportional to the emission spectrum $S(\omega)$:

$$S(\omega) = \text{const} \times \int_{-\infty}^{+\infty} \langle \hat{P}^{(-)}(t+\tau)\hat{P}^{(+)}(\tau)\rangle \mid_{\tau\to\infty} e^{-i\omega t} dt, \tag{5.4}$$

whereas such a Fourier transform is also related to the absorption spectrum $A(\omega)$ according to linear response theory:[75]

$$A(\omega_p) = \text{const} \times \int_{-\infty}^{+\infty} \langle \left[\hat{P}^{(-)}(t+\tau), \hat{P}^{(+)}(\tau)\right]\rangle \mid_{\tau\to\infty} e^{-i\omega_p t} dt. \tag{5.5}$$

For convenience, we will perform Laplace transform instead of Fourier transform. The Laplace transform for a function $f(t)$ is given by:

$$\bar{f}(z) = \int_0^{\infty} f(t) e^{-zt} dt. \tag{5.6}$$

Where the overbar denotes functions in Laplace space. It is clear from Eq. (5.6) that for a function $f(t) = f^*(-t)$, the Laplace transform is easily linked to Fourier transform by taking the real part of $\bar{f}(z)$ and setting $z = i\omega$.

We will first write down the master equation in the interaction picture to solve for the one-time expectation values for the elements of density matrix, then, we will apply the quantum regression theorem to obtain the equations for the two-time atomic correlation function $\Gamma^{(1)}(t+\tau,\tau)$, whose Fourier transform gives the emission and absorption spectrum. As mentioned earlier, we will solve the equations in the Laplace space and obtain expressions for the emission and absorption spectrum.

5.3 Master Equation

We will start our derivation with the Hamiltonian:

$$\hat{H} = \hat{H}_0 + \hat{H}_i, \tag{5.7}$$

where

$$\hat{H}_0 = \epsilon_1 \hat{a}_1^\dagger \hat{a}_1 + \epsilon_2 \hat{a}_2^\dagger \hat{a}_2 + \epsilon_3 \hat{a}_3^\dagger \hat{a}_3 \tag{5.8}$$

is the unperturbed Hamiltonian for the three-level atom and ϵ_i $(i = 1, 2, 3)$ are the energy eigenvalues of the isolated atom with atomic transition frequencies $\hbar\omega_{13} = \epsilon_1 - \epsilon_3$ and $\hbar\omega_{12} = \epsilon_1 - \epsilon_2$. $\hat{a}_i$ and $\hat{a}_i^\dagger$ are the fermion operators that describe the creation of an electron in level i or its removal. A complete set of the eigenvectors for the unperturbed Hamiltonian is taken as $|1\rangle$, $|2\rangle$ and $|3\rangle$ with the relations:

$$\hat{a}_i^\dagger \hat{a}_j |k\rangle = \delta_{jk} |i\rangle, \quad i, j, k = 1, 2, 3. \tag{5.9}$$

The interactive part of the Hamiltonian, H_i can be written as,

$$H_i = -\hat{\boldsymbol{\mu}} \cdot \hat{\mathbf{E}}_0 \tag{5.10}$$

where $\hat{\boldsymbol{\mu}} = \hat{\boldsymbol{\mu}}_1 + \hat{\boldsymbol{\mu}}_2$ is the total atomic dipole operator and $\hat{\mathbf{E}}_0$ is the total electric field, which we have simply taken to be a classical field and can be written as the sum of the two driving fields:

$$\hat{\mathbf{E}}_0 = \mathbf{E}_1 e^{-i\Omega_1 t} + \mathbf{E}_2 e^{-i\Omega_2 t} + \text{ c.c.} \tag{5.11}$$

Assume that the driving field $\mathbf{E}_1$ only interacts with the transition $1 \leftrightarrow 3$ and the field $\mathbf{E}_2$ only interacts with the transition $1 \leftrightarrow 2$, and define Rabi frequencies G_1 and G_2:

$$G_i = -\frac{\hat{\boldsymbol{\mu}}_i \cdot \mathbf{E_i}}{\hbar}, \qquad (i = 1, 2) \tag{5.12}$$

then the interaction Hamiltonian can be expressed in the rotating wave approximation

as:

$$\hat{H}_i = \left(\hbar G_1 e^{-i\Omega_1 t}\hat{a}_1^\dagger \hat{a}_3 + \text{ h.c.}\right) + \left(\hbar G_2 e^{-i\Omega_2 t}\hat{a}_1^\dagger \hat{a}_2 + \text{ h.c.}\right). \tag{5.13}$$

The evolution of the system in the interaction picture is governed by the master equation:

$$\frac{\partial \hat{\rho}}{\partial t} = \frac{1}{i\hbar}\left[\hat{H}_i, \hat{\rho}\right] + \text{relaxation terms}, \tag{5.14}$$

with $\hat{\rho}$ being the density matrix:

$$\hat{\rho} = |i\rangle\langle j|, \qquad (i,j = 1,2,3), \tag{5.15}$$

and the relaxation terms are included phenomenologically according to the following rules:

1. The three-level system defined by $|1\rangle$, $|2\rangle$ and $|3\rangle$ is closed, in the sense that the relaxation mechanisms only produce transitions within it. This implies that the equality:

   $$\text{Tr}(\hat{\rho}) = \rho_{11} + \rho_{22} + \rho_{33} = 1 \tag{5.16}$$

   holds for all time.

2. The excited state population ρ_{11} decays by spontaneous emission with the rates $2\gamma_1$ and $2\gamma_2$ to the lower states $|3\rangle$ and $|2\rangle$, respectively. This introduces a term of $-(2\gamma_1 + 2\gamma_2)\rho_{11}$ in the equation for ρ_{11} and a term $2\gamma_1\rho_{11}$ $(2\gamma_2\rho_{22})$ in the equation for ρ_{33} (ρ_{22}) .

3. The ground states $|2\rangle$ and $|3\rangle$ exchange population with rates ν_1 and ν_2, i.e., the state $|2\rangle$ transfers population to $|3\rangle$ with a rate of ν_1 and vice versa with a rate of ν_2, this introduces a term $-\nu_1\rho_{22} + \nu_2\rho_{33}$ in the equation for ρ_{22} and the same term with opposite sign in the equation for ρ_{33}.

4. The relaxation rates for the coherences (ρ_{12}, ρ_{13} and ρ_{23}) are half of the sum of the population decay rates for the upper and lower levels. For example, for the optical coherence ρ_{12}, the upperlevel $|1\rangle$ loses population at a rate of $2\gamma_1 + 2\gamma_2$,

and the lowerlevel $|2\rangle$ loses population at a rate of ν_1, thus the relaxation rate for ρ_{12} is $(\gamma_1 + \gamma_2 + \nu_2/2)$. For the ground state coherence ρ_{23}, the upper and lower levels loses population at a rate of ν_1 or ν_2, making the relaxation rate for ρ_{23} to be $(\nu_1 + \nu_2)/2$.

With these assumptions and the convenient expression for the matrix elements of the operators $\hat{a}_i^\dagger \hat{a}_j$ derived from Eq. (5.9):

$$\langle l|\hat{a}_i^\dagger \hat{a}_j|k\rangle = \delta_{jk}\delta_{li}, \tag{5.17}$$

it is straightforward to expand the master equation into component form:

$$\frac{\partial \tilde{\rho}_{11}}{\partial t} = -iG_2\tilde{\rho}_{21} + iG_2^*\tilde{\rho}_{12} - iG_1\tilde{\rho}_{31} + iG_1^*\tilde{\rho}_{13} - (2\gamma_1 + 2\gamma_2)\tilde{\rho}_{11} \tag{5.18a}$$

$$\frac{\partial \tilde{\rho}_{22}}{\partial t} = iG_2\tilde{\rho}_{21} - iG_2^*\tilde{\rho}_{12} + 2\gamma_2\tilde{\rho}_{11} + \nu_2\tilde{\rho}_{33} - \nu_1\tilde{\rho}_{22} \tag{5.18b}$$

$$\frac{\partial \tilde{\rho}_{33}}{\partial t} = iG_1\tilde{\rho}_{31} - iG_1^*\tilde{\rho}_{13} + 2\gamma_1\tilde{\rho}_{11} - \nu_2\tilde{\rho}_{33} + \nu_1\tilde{\rho}_{22} \tag{5.18c}$$

$$\frac{\partial \tilde{\rho}_{12}}{\partial t} = -iG_2(\tilde{\rho}_{22} - \tilde{\rho}_{11}) - iG_1\tilde{\rho}_{32} - i\Delta_2\tilde{\rho}_{12} - (\gamma_1 + \gamma_2 + \nu_1/2)\,\tilde{\rho}_{12} \tag{5.18d}$$

$$\frac{\partial \tilde{\rho}_{13}}{\partial t} = -iG_1(\tilde{\rho}_{33} - \tilde{\rho}_{11}) - iG_2\tilde{\rho}_{23} - i\Delta_1\tilde{\rho}_{13} - (\gamma_1 + \gamma_2 + \nu_2/2)\,\tilde{\rho}_{13} \tag{5.18e}$$

$$\frac{\partial \tilde{\rho}_{23}}{\partial t} = -iG_2^*\tilde{\rho}_{13} + iG_1\tilde{\rho}_{21} - i\,(\Delta_1 - \Delta_2)\,\tilde{\rho}_{23} - \frac{\nu_1 + \nu_2}{2}\tilde{\rho}_{23} \tag{5.18f}$$

$$\tilde{\rho}_{21} = \tilde{\rho}_{12}^* \tag{5.18g}$$

$$\tilde{\rho}_{31} = \tilde{\rho}_{13}^* \tag{5.18h}$$

$$\tilde{\rho}_{32} = \tilde{\rho}_{23}^* \tag{5.18i}$$

where we have defined

$$\tilde{\rho}_{ii} = \rho_{ii} \qquad i = 1, 2, 3 \tag{5.19a}$$

$$\tilde{\rho}_{12} = \rho_{12}e^{i\Omega_2 t} \tag{5.19b}$$

$$\tilde{\rho}_{13} = \rho_{13} e^{i\Omega_1 t} \tag{5.19c}$$

$$\tilde{\rho}_{23} = \rho_{23} e^{i(\Omega_1 - \Omega_2)t} \tag{5.19d}$$

to remove the rapid oscillating terms in ρ_{ij}.

As mentioned in Eq. (5.16), only eight out of the nine components of $\tilde{\rho}$ are independent, in order to use the quantum regression theorem, we must eliminate one of the diagonal matrix element of $\tilde{\rho}$, e.g., $\tilde{\rho}_{33}$, and define the column vector $\boldsymbol{\psi}$ with its eight components as:

$$\boldsymbol{\psi}^T = (\tilde{\rho}_{11}, \tilde{\rho}_{12}, \tilde{\rho}_{13}, \tilde{\rho}_{21}, \tilde{\rho}_{22}, \tilde{\rho}_{23}, \tilde{\rho}_{31}, \tilde{\rho}_{32}) . \tag{5.20}$$

The final result can be cast in the form of the compact vector equation:

$$\frac{d}{dt} \boldsymbol{\psi}(t) = \mathbf{L}\, \boldsymbol{\psi}(t) + \mathbf{I}. \tag{5.21}$$

The explicit forms of matrix $\mathbf{L}$ and vector $\mathbf{I}$ are listed in Table 5.1. The inhomogeneous vector $\mathbf{I}$ originates from the elimination of $\tilde{\rho}_{33}$ from Eq. (5.18) and its replacement with $1 - \tilde{\rho}_{11} - \tilde{\rho}_{22}$ according to the trace condition Eq. (5.16).

Because, we have already mentioned in Section 5.2, our calculation of the quantities of interest involves the quantum regression theorem, we will need explicit expressions for variables $\psi_i (i = 1, 2, ..., 8)$ in terms of their initial values. This can be done more conveniently in Laplace space. Thus, if τ denotes an arbitrary initial time, the Laplace transform of Eq. (5.21) yields

$$\bar{\boldsymbol{\psi}}(z) = \bar{\mathbf{M}}(z)\ \boldsymbol{\psi}(\tau) + \frac{1}{z} \bar{\mathbf{M}}(z)\, \mathbf{I} \tag{5.22}$$

where

$$\mathbf{M}(z) = (z\mathbf{1} - \mathbf{L})^{-1}, \tag{5.23}$$

and $\mathbf{1}$ denotes the identity matrix.

We do not need to worry about the explicit time-dependent solution of Eq. (5.21)

Matrix Elements L_{ij} for the Λ system									I_i
j \ i	1	2	3	4	5	6	7	8	1
1	$-2\gamma_1$ $-2\gamma_2$	iG_2^*	iG_1^*	$-iG_2$	0	0	$-iG_1$	0	0
2	iG_2	$-i\Delta_2-$ $\gamma_1-\gamma_2$ $-\nu_1/2$	0	0	$-iG_2$	0	0	$-iG_1$	0
3	$2iG_1$	0	$-i\Delta_1-$ $\gamma_1-\gamma_2$ $-\nu_2/2$	0	iG_1	$-iG_2$	0	0	$-iG_1$
4	$-iG_2^*$	0	0	$i\Delta_2-$ $\gamma_1-\gamma_2$ $-\nu_1/2$	iG_2^*	iG_1^*	0	0	0
5	$2\gamma_2-\nu_2$	$-iG_2^*$	0	iG_2	$-\nu_1-\nu_2$	0	0	0	ν_2
6	0	0	$-iG_2^*$	iG_1	0	$i\Delta_2-i\Delta_1$ $-\nu_1/2$ $-\nu_2/2$	0	0	0
7	$-2iG_1^*$	0	0	0	$-iG_1^*$	0	$i\Delta_1-$ $\gamma_1-\gamma_2$ $-\nu_2/2$	iG_2^*	iG_1^*
8	0	$-iG_1^*$	0	0	0	0	iG_2	$i\Delta_1-i\Delta_2$ $-\nu_1/2$ $-\nu_2/2$	0

Table 5.1: Matrix elements **L** and **I** for the Λ system

(except of course in our implementation of the regression theorem), but we do need the steady-state solution. This is given by

$$\psi(\infty) = -\mathbf{L}^{-1}\mathbf{I}. \tag{5.24}$$

5.4 The Quantum Regression Theorem

Next we will apply the quantum regression theorem to the expectation values of the atomic operators to get the two-time correlation function.

The quantum regression theorem[96] states that if $\hat{M}$, $\hat{Q}$, $\hat{N}$ are members of a complete set of system operators $\{\hat{S}_\mu\}$ and if the one-time averages can be expressed in the form

$$\langle \hat{M}(t+\tau)\rangle = \sum_\mu O_\mu(t+\tau,\tau)\langle \hat{S}_\mu(\tau)\rangle, \qquad t>0, \tag{5.25}$$

where $O_\mu(t+\tau,\tau)$ are c-number functions of time, then two-time expectation values take the form

$$\langle \hat{Q}(\tau)\hat{M}(t+\tau)\hat{N}(\tau)\rangle = \sum_\mu O_\mu(t+\tau,\tau)\langle \hat{Q}(\tau)\hat{S}_\mu(\tau)\hat{N}(\tau)\rangle, \qquad t>0. \tag{5.26}$$

Specifically, the operator $\hat{M}$ can be identified as the negative part of the total atomic polarization operator $\hat{P}(t)$ which takes the form

$$\hat{P}(t) = \hat{P}^{(+)}(t) + \hat{P}^{(-)}(t) \tag{5.27}$$

with its positive and negative parts:

$$\hat{P}^{(+)}(t) = \mu_{12}\hat{a}_1^\dagger\hat{a}_2 + \mu_{13}\hat{a}_1^\dagger\hat{a}_3 \tag{5.28a}$$

$$\hat{P}^{(-)}(t) = \left(\hat{P}^{(+)}(t)\right)^\dagger, \tag{5.28b}$$

where μ_{1i} $(i=2,3)$ are the moduli of the induced transition dipole moments and where we have assumed $\mu_{23}=0$. The complete set of system operators $\{\hat{S}_\mu\}$ in

Eq. (5.25) can be chosen as ψ_i $(i = 1, 2, ..., 8)$, which are the one-time expectation values of the atomic operators (cf. Eq. (5.37)). The one-time average of $\hat{P}^{(-)}$ is readily expressed in term of $\psi_i(t)$:

$$\langle \hat{P}^{(-)}(t+\tau) \rangle = \mu_{12} e^{i\Omega_2(t+\tau)} \psi_4(t+\tau) + \mu_{13} e^{i\Omega_1(t+\tau)} \psi_7(t+\tau) \tag{5.29}$$

which can in turn be expressed in terms of $\psi_i(\tau)$ by means of Eq. (5.21). Thus if we take the operator $\hat{Q}$ in Eq. (5.26) to be the identity operator, and the operator $\hat{N}$ to be the positive part of the the atomic polarization operator, we can evaluate the atomic correlation function $\Gamma^{(1)}$ in Eq. (5.3) and make a Fourier transform to get the emission and absorption spectra as outlined in Section 5.2.

For the reasons discussed in Section 5.2, we will not take such an approach and will follow along a different path instead. In fact, we can reexpress the quantum regression theorem in Laplace space, then, Eq. (5.25) becomes:

$$\langle \hat{\bar{M}}(z) \rangle = \sum_{\mu} \bar{O}_{\mu}(z, \tau) \langle \hat{S}_{\mu}(\tau) \rangle. \tag{5.30}$$

And the expression for the correlation function Eq. (5.26) becomes:

$$\langle \hat{Q}(\tau) \hat{\bar{M}}(z) \hat{N}(\tau) \rangle = \sum_{\mu} \bar{O}_{\mu}(z, \tau) \langle \hat{Q}(\tau) \hat{S}_{\mu}(\tau) \hat{N}(\tau) \rangle. \tag{5.31}$$

The advantage of operating in Laplace space is evident: not only is Eq. (5.21) more easily solved with initial conditions in Laplace space, but the emission and absorption spectra $S(\omega)$ and $A(\omega)$ themselves are obtained through Fourier transformation Eq. (5.4) and Eq. (5.5) and is now simpler in Laplace space:

$$S(\omega) \propto \mathrm{Re} \left\{ \left\langle \hat{\bar{P}}^{(-)}(z) \hat{P}^{(+)}(\tau) \right\rangle \Big|_{z=i\omega} \right\}, \tag{5.32}$$

and

$$A(\omega_p) \propto \mathrm{Re} \left\{ \left\langle \left[\hat{\bar{P}}^{(-)}(z), \hat{P}^{(+)}(\tau) \right] \right\rangle \Big|_{z=i\omega_p} \right\}. \tag{5.33}$$

5.5 The Emission Spectrum

In this section, we will explicitly apply the quantum regression theorem (in Laplace space) to derive the formula for the fluorescent spectrum.

Our starting point is the one-time average Eq. (5.29), which is now expressed in Laplace space as:

$$\langle \hat{\bar{P}}^{(-)}(z) \rangle = \mu_{12} \bar{\psi}_4 (z - i\Omega_2) + \mu_{13} \bar{\psi}_7 (z - i\Omega_1). \tag{5.34}$$

With the help of Eq. (5.22), Eq. (5.34) can be cast into the required form:

$$\langle \hat{\bar{P}}^{(-)}(z) \rangle = \mu_{12} \sum_j \left(\bar{M}_{4j} (z - i\Omega_2) \psi_j (\tau) + \frac{\bar{M}_{4j} (z - i\Omega_2)}{z - i\Omega_2} I_j \right) + \mu_{13} \sum_j \left(\bar{M}_{7j} (z - i\Omega_1) \psi_j (\tau) + \frac{\bar{M}_{7j} (z - i\Omega_1)}{z - i\Omega_1} I_j \right). \tag{5.35}$$

Next we must express $\psi_j(\tau)$ and I_j in the form of expectation values of system operators at τ. This can be done directly from the definition of $\psi_j(\tau)$ and the relationship Eq. (5.17), e.g.:

$$\langle \hat{a}_1^\dagger \hat{a}_2 \rangle_\tau = \mathrm{Tr} \left(\rho \hat{a}_1^\dagger \hat{a}_2 \right)_\tau = \langle 2|\rho|1\rangle_\tau \langle 1|\hat{a}_1^\dagger \hat{a}_2|2\rangle_\tau = \tilde{\rho}_{21} e^{i\Omega_2 \tau} = \psi_4 (\tau) e^{i\Omega_2 \tau} \tag{5.36}$$

or

$$\psi_4 (\tau) = e^{-i\Omega_2 \tau} \langle \hat{a}_1^\dagger \hat{a}_2 \rangle_\tau. \tag{5.37}$$

In addition, the inhomogeneous term I_j can also be written as:

$$I_j = I_j \mathrm{Tr} (\rho \mathbf{1}) = I_j \langle \mathbf{1} \rangle. \tag{5.38}$$

According to the regression theorem, the correlation function $\langle \hat{\bar{P}}^{(-)}(z)\, \hat{P}^{(+)}(\tau) \rangle$ can be obtained from the above expression for $\langle \hat{\bar{P}}^{(-)}(z) \rangle$ by replacing every expectation value of the type $\langle \hat{a}_1^\dagger \hat{a}_2 \rangle_\tau$ with $\langle \hat{a}_1^\dagger \hat{a}_2 \hat{P}^{(+)} \rangle_\tau$. Consider for example $\psi_4(\tau)$ which

contains the expectation value $\langle \hat{a}_1^\dagger \hat{a}_2 \rangle_\tau$, in this case we have:

$$\begin{aligned}
\psi_4(\tau) = e^{-i\Omega_2\tau}\langle \hat{a}_1^\dagger \hat{a}_2 \rangle_\tau \quad &\rightarrow \quad e^{-i\Omega_2\tau}\langle \hat{a}_1^\dagger \hat{a}_2 \hat{P}^{(+)} \rangle_\tau \\
&= e^{-i\Omega_2\tau}\left(\mu_{12}\langle \hat{a}_1^\dagger \hat{a}_2 \hat{a}_2^\dagger \hat{a}_1 \rangle_\tau + \mu_{13}\langle \hat{a}_1^\dagger \hat{a}_2 \hat{a}_3^\dagger \hat{a}_1 \rangle_\tau\right) \\
&= \mu_{12} e^{-i\Omega_2\tau}\tilde{\rho}_{11} \\
&= \mu_{12} e^{-i\Omega_2\tau}\psi_1(\tau). \qquad (5.39)
\end{aligned}$$

The complete replacement table of type $\left\langle \hat{a}_i^\dagger \hat{a}_j \hat{P}^{(+)} \right\rangle_\tau$ is provided in Table 5.2(a).

In a similar way we have

$$\langle \mathbf{1} \rangle \rightarrow \langle \hat{P}^{(+)} \rangle_\tau = \mu_{12} e^{-i\Omega_2\tau}\psi_2(\tau) + \mu_{13} e^{-i\Omega_1\tau}\psi_3(\tau). \qquad (5.40)$$

Now we will take the limit $\tau \rightarrow \infty$ and get to the following result:

$$\begin{aligned}
&\langle \hat{\tilde{P}}^{(-)}(z)\hat{P}^{(+)}(\infty) \rangle = \\
&\mu_{13}^2 \left\{ M_{77}(z_1)\psi_1(\infty) + M_{78}(z_1)\psi_2(\infty) + \sum_j \frac{1}{z_1} M_{7j}(z_1) I_j \psi_3(\infty) \right\} + \\
&\quad \mu_{12}^2 \left\{ M_{44}(z_2)\psi_1(\infty) + M_{45}(z_2)\psi_2(\infty) + \right. \\
&\quad \left. M_{46}(z_2)\psi_3(\infty) + \sum_j \frac{1}{z_2} M_{4j}(z_2) I_j \psi_2(\infty) \right\}, \qquad (5.41)
\end{aligned}$$

where $z_i = z - i\Omega_i$ $(i = 1, 2)$. Eq.(5.41) shows that the spectrum of resonance fluorescence is composed of two separate structures with center frequencies located at Ω_2 and Ω_1, respectively, and magnitudes proportional to the dipole moments of the two atomic transitions. Each contribution is the sum of the terms:

$$f(z) = M(z - i\Omega_i)\psi(\infty) + \frac{M(z - i\Omega_i) I_j \psi(\infty)}{z - i\Omega_i}, \qquad (5.42)$$

where M and ψ should be understood as the components of the corresponding ma-

(a) Replacement table of type $\left\langle \hat{a}_i^\dagger \hat{a}_j \hat{P}^{(+)} \right\rangle_\tau$ for the Λ system			
$\psi_1(\tau)$	$\longrightarrow$	$\left\langle \hat{a}_1^\dagger \hat{a}_1 \hat{P}^{(+)} \right\rangle_\tau$	$= 0$
$\psi_2(\tau)$	$\longrightarrow$	$e^{i\Omega_2\tau} \left\langle \hat{a}_2^\dagger \hat{a}_1 \hat{P}^{(+)} \right\rangle_\tau$	$= 0$
$\psi_3(\tau)$	$\longrightarrow$	$e^{i\Omega_1\tau} \left\langle \hat{a}_3^\dagger \hat{a}_1 \hat{P}^{(+)} \right\rangle_\tau$	$= 0$
$\psi_4(\tau)$	$\longrightarrow$	$e^{-i\Omega_2\tau} \left\langle \hat{a}_1^\dagger \hat{a}_2 \hat{P}^{(+)} \right\rangle_\tau$	$= \mu_{12} e^{-i\Omega_2\tau} \psi_1(\tau)$
$\psi_5(\tau)$	$\longrightarrow$	$\left\langle \hat{a}_2^\dagger \hat{a}_2 \hat{P}^{(+)} \right\rangle_\tau$	$= \mu_{12} e^{-i\Omega_2\tau} \psi_2(\tau)$
$\psi_6(\tau)$	$\longrightarrow$	$e^{-i(\Omega_2-\Omega_1)\tau} \left\langle \hat{a}_3^\dagger \hat{a}_2 \hat{P}^{(+)} \right\rangle_\tau$	$= \mu_{12} e^{-i\Omega_2\tau} \psi_3(\tau)$
$\psi_7(\tau)$	$\longrightarrow$	$e^{-i\Omega_1\tau} \left\langle \hat{a}_3^\dagger \hat{a}_1 \hat{P}^{(+)} \right\rangle_\tau$	$= \mu_{13} e^{-i\Omega_1\tau} \psi_1(\tau)$
$\psi_8(\tau)$	$\longrightarrow$	$e^{i(\Omega_2-\Omega_1)\tau} \left\langle \hat{a}_2^\dagger \hat{a}_3 \hat{P}^{(+)} \right\rangle_\tau$	$= \mu_{13} e^{-i\Omega_1\tau} \psi_2(\tau)$
$\langle \mathbf{1} \rangle_\tau$	$\longrightarrow$	$\left\langle \hat{P}^{(+)} \right\rangle_\tau$	$= \mu_{12} e^{-i\Omega_2\tau} \psi_2(\tau) + \mu_{13} e^{-i\Omega_1\tau} \psi_3(\tau)$

(b) Replacement table of type $\left\langle \hat{P}^{(+)} \hat{a}_i^\dagger \hat{a}_j \right\rangle_\tau$ for the Λ system			
$\psi_1(\tau)$	$\longrightarrow$	$\left\langle \hat{P}^{(+)} \hat{a}_1^\dagger \hat{a}_1 \right\rangle_\tau$	$= \mu_{12} e^{-i\Omega_2\tau} \psi_2(\tau) + \mu_{13} e^{-i\Omega_1\tau} \psi_3(\tau)$
$\psi_2(\tau)$	$\longrightarrow$	$e^{i\Omega_2\tau} \left\langle \hat{P}^{(+)} \hat{a}_2^\dagger \hat{a}_1 \right\rangle_\tau$	$= 0$
$\psi_3(\tau)$	$\longrightarrow$	$e^{i\Omega_1\tau} \left\langle \hat{P}^{(+)} \hat{a}_3^\dagger \hat{a}_1 \right\rangle_\tau$	$= 0$
$\psi_4(\tau)$	$\longrightarrow$	$e^{-i\Omega_2\tau} \left\langle \hat{P}^{(+)} \hat{a}_1^\dagger \hat{a}_2 \right\rangle_\tau$	$= \mu_{12} e^{-i\Omega_2\tau} \psi_5(\tau) + \mu_{13} e^{-i\Omega_1\tau} \psi_6(\tau)$
$\psi_5(\tau)$	$\longrightarrow$	$\left\langle \hat{P}^{(+)} \hat{a}_2^\dagger \hat{a}_2 \right\rangle_\tau$	$= 0$
$\psi_6(\tau)$	$\longrightarrow$	$e^{-i(\Omega_2-\Omega_1)\tau} \left\langle \hat{P}^{(+)} \hat{a}_3^\dagger \hat{a}_2 \right\rangle_\tau$	$= 0$
$\psi_7(\tau)$	$\longrightarrow$	$e^{-i\Omega_1\tau} \left\langle \hat{P}^{(+)} \hat{a}_3^\dagger \hat{a}_1 \right\rangle_\tau$	$= \mu_{12} e^{-i\Omega_2\tau} \psi_8(\tau) + \mu_{13} e^{-i\Omega_1\tau} \times$ $(1 - \psi_1(\tau) - \psi_5(\tau))$
$\psi_8(\tau)$	$\longrightarrow$	$e^{i(\Omega_2-\Omega_1)\tau} \left\langle \hat{P}^{(+)} \hat{a}_2^\dagger \hat{a}_3 \right\rangle_\tau$	$= 0$
$\langle \mathbf{1} \rangle_\tau$	$\longrightarrow$	$\left\langle \hat{P}^{(+)} \right\rangle_\tau$	$= \mu_{12} e^{-i\Omega_2\tau} \psi_2(\tau) + \mu_{13} e^{-i\Omega_1\tau} \psi_3(\tau)$

Table 5.2: The complete replacement table for the Λ system

trices. Eq. (5.42) can be further written in the form:

$$f(z) = \frac{A}{z} + g(z), \tag{5.43}$$

where A is a constant whose value is determined by $M(0)I_j\psi(\infty)$ and $g(z)$ has the form $M(z - i\Omega_i)\psi(\infty) + (M(z - i\Omega_i) - M(0))I_j\psi(\infty)/(z - i\Omega_i)$. Both terms are analytic functions of z for $\mathrm{Re}(z - i\Omega_i) \geq 0$ because the singularity at $z = i\Omega_i$ of the latter can be removed by taking the limit $z \to i\Omega_i$. Such a limit exists because $M(z)$ itself is differentiable at $z = i\Omega_i$.

The singularity in Eq. (5.43) reflects the existence of a coherent Rayleigh peak whose origin can be traced to the elastic scattering of the driving fields, while $g(z)$ describes the incoherent part of the spectrum of the emitted radiation. Indeed, the coherent part of the scattered field would take the form $e^{i\Omega_i t}$ in the real space, and its Laplace transform would take the form $1/(z - i\Omega_i)$ in Laplace space.

We are interested primarily in the incoherent part of the scattered field, which can be obtained by removing the singularity from Eq. (5.41). If we denote the full correlation function in Laplace space with

$$\bar{\Gamma}^{(1)}(z) \equiv \langle \hat{\bar{P}}^{(-)}(z)\, \hat{P}^{(+)}(\infty) \rangle \equiv \bar{\Gamma}^{(1)}_{\mathrm{coh}}(z) + \bar{\Gamma}^{(1)}_{\mathrm{incoh}}(z), \tag{5.44}$$

then the incoherent part $\bar{\Gamma}^{(1)}_{\mathrm{incoh}}(z)$ can be calculated according to the simple algorithm

$$\bar{\Gamma}^{(1)}_{\mathrm{incoh}}(z) = \bar{\Gamma}^{(1)}(z) - \frac{1}{z - i\Omega_1} \lim_{z \to i\Omega_1} (z - i\Omega_1)\, \bar{\Gamma}^{(1)}(z) - \frac{1}{z - i\Omega_2} \lim_{z \to i\Omega_2} (z - i\Omega_2)\, \bar{\Gamma}^{(1)}(z), \tag{5.45}$$

where after removal of the singularity, the diverging term $\mathbf{M}(z - i\Omega_i)/(z - i\Omega_i)$ in Eq. (5.42) takes the form:

$$\frac{\mathbf{M}(z - i\Omega_i) - \mathbf{M}(0)}{z - i\Omega_i} = \mathbf{L}^{-1}(z\mathbf{1} - \mathbf{L})^{-1}, \tag{5.46}$$

where we have used Eq. (5.23) and the identity

$$[\mathbf{L}(z\mathbf{1}-\mathbf{L})]\times\left[(z\mathbf{1}-\mathbf{L})^{-1}+\mathbf{L}^{-1}\right]=z\mathbf{1}. \tag{5.47}$$

Thus if we replace all the instances of $M_{ij}(z-i\Omega_i)/(z-i\Omega_i)$ in Eq. (5.41) by N_{ij} where

$$\hat{\mathbf{N}}(z)=\left(\mathbf{L}^{-1}(z\mathbf{1}-\mathbf{L})^{-1}\right), \tag{5.48}$$

and taking $z=i\omega$, we are finally able to obtain the incoherent fluorescence spectra $S_1^{\text{incoh}}(\omega)$ for the transition $1\leftrightarrow 3$ and $S_2(\omega)$ for the transition $1\leftrightarrow 2$:

$$\begin{aligned} S_1^{\text{incoh}}(\omega) &= \text{Re}\Big\{M_{77}(i\omega-i\Omega_1)\psi_1(\infty)+M_{78}(i\omega-i\Omega_1)\psi_2(\infty)+ \\ &\qquad \sum_j N_{7j}(i\omega-i\Omega_1)I_j\psi_3(\infty)\Big\}, \end{aligned} \tag{5.49a}$$

$$\begin{aligned} S_2^{\text{incoh}}(\omega) &= \text{Re}\Big\{M_{44}(i\omega-i\Omega_2)\psi_1(\infty)+M_{45}(i\omega-i\Omega_2)\psi_2(\infty)+ \\ &\qquad M_{46}(i\omega-i\Omega_2)\psi_3(\infty)+\sum_j N_{4j}(i\omega-i\Omega_2)I_j\psi_2(\infty)\Big\}. \end{aligned} \tag{5.49b}$$

The total emission spectra $S_i^{\text{total}}(\omega)$ consists of the sum of the coherent and incoherent parts:

$$S_i^{\text{total}}(\omega)=S_i^{\text{incoh}}(\omega)+S_i^{\text{coh}}(\omega). \tag{5.50}$$

The coherent part of the emission spectra $S_i^{\text{coh}}(\omega)$ is only related to the steady-state solution of the master equation and is discussed elsewhere [cf. Eq. (5.66)].

5.6 The Absorption Spectrum of a Weak Probe

We now turn our attention to a related problem: the three-level system is driven by the external fields at frequencies Ω_1 and Ω_2 and is probed by a tunable weak beam of frequency ω_p whose attenuation (or amplification) is measured in transmission.

According to the linear response theory, the exponential attenuation coefficient at a given frequency ω_p is given by Eq. (5.5), where the square brackets indicate the unequal time commutator and the quantum ensemble average $\langle ... \rangle$ must be carried out under steady-state conditions $\tau \to \infty$.

The absorption spectrum is composed of two parts: the first, $\langle \hat{P}^{(-)}(t+\tau)\hat{P}^{(+)}(\tau)\rangle$, is identical to the one calculated in the previous section; the second, $\langle \hat{P}^{(+)}(\tau)\hat{P}^{(-)}(t+\tau)\rangle$, can be derived following the same procedure with only minor modifications, i.e., we must replace the terms $\psi_j(\tau)$ and I_j in the one-time average equation Eq. (5.35) of the type $\langle \hat{a}_i \hat{a}_j^\dagger \rangle$ and $\langle \mathbf{1} \rangle$ with $\langle \hat{P}^{(+)}(\tau)\hat{a}_i\hat{a}_j^\dagger\rangle$ and $\langle \hat{P}^{(+)}(\tau)\rangle$, respectively. Such a replacement table is given in Table 5.2(b) and the result for $\langle \hat{P}^{(+)}(\infty)\hat{\tilde{P}}^{(-)}(z)\rangle$ is:

$$
\begin{aligned}
&\langle \hat{\tilde{P}}^{(+)}(\infty)\hat{P}^{(-)}(z)\rangle = \\
&\quad \mu_{13}^2 \Bigg\{ M_{71}(z_1)\,\psi_3(\infty) + M_{74}(z_1)\,\psi_6(\infty) + \\
&\qquad M_{77}(z_1)\,(1-\psi_1(\infty)-\psi_5(\infty)) + \sum_j \frac{1}{z_1} M_{7j}(z_1)\, I_j \psi_3(\infty) \Bigg\} + \\
&\quad \mu_{12}^2 \Bigg\{ M_{41}(z_2)\,\psi_2(\infty) + M_{44}(z_2)\,\psi_5(\infty) + \\
&\qquad M_{47}(z_2)\,\psi_8(\infty) + \sum_j \frac{1}{z_2} M_{4j}(z_2)\, I_j \psi_2(\infty) \Bigg\}. \qquad (5.51)
\end{aligned}
$$

The diverging part in Eq. (5.51) cancels with the diverging part of Eq. (5.41), and the final result for the absorption spectrum $A_1(\omega_{p_1})$ for the transition $1 \leftrightarrow 3$ and $A_2(\omega_{p_2})$ for the transition $1 \leftrightarrow 2$ are:

$$
\begin{aligned}
A_1(\omega_{p_1}) = \mathrm{Re} \Big\{ & M_{78}(i\omega_{p_1} - i\Omega_1)\,\psi_2(\infty) - M_{71}(i\omega_{p_1} - i\Omega_1)\,\psi_3(\infty) - \\
& M_{74}(i\omega_{p_1} - i\Omega_1)\,\psi_6(\infty) - M_{77}(i\omega_{p_1} - i\Omega_1)\,(1 - 2\psi_1(\infty) - \psi_5(\infty)) \Big\} \qquad (5.52a)
\end{aligned}
$$

$$A_2(\omega_{p_2}) = \mathrm{Re}\Big\{ M_{44}(i\omega_{p_2} - i\Omega_2)\,\psi_1(\infty) + M_{45}(i\omega_{p_2} - i\Omega_2)\,\psi_2(\infty) +$$

$$M_{46}(i\omega_{p_2} - i\Omega_2)\,\psi_3(\infty) - M_{41}(i\omega_{p_2} - i\Omega_2)\,\psi_2(\infty) -$$

$$M_{44}(i\omega_{p_2} - i\Omega_2)\,\psi_5(\infty) - M_{47}(i\omega_{p_2} - i\Omega_2)\,\psi_8(\infty) \Big\}. \qquad (5.52b)$$

5.7 Ξ and V system

The above result can easily be extended to Ξ and V systems. Our notation in Fig. (5.1) is that the level "1" is always the common level, thus in V system the level 1 is the ground state and in Ξ system it is the middle level, whereas in the Λ system discussed above the level 1 is the excited state. Our definition for Δ_i thus must be changed slightly to always refer to a "positive" detuning, i.e., a positive Δ_i always means that the frequency of the driving field is lower than the frequency of the corresponding atomic transition. Thus for Ξ system:

$$\Delta_1 = \omega_{31} - \Omega_1 \qquad (5.53a)$$

$$\Delta_2 = \omega_{12} - \Omega_2 \qquad (5.53b)$$

and for V system:

$$\Delta_1 = \omega_{31} - \Omega_1 \qquad (5.54a)$$

$$\Delta_2 = \omega_{21} - \Omega_2. \qquad (5.54b)$$

Our definition for the atomic polarization operator $\hat{P}^{(\pm)}$ must also be altered, e.g.,

for Ξ system,

$$\hat{P}^{(+)}(t) = \mu_{12}\hat{a}_1^\dagger\hat{a}_2 + \mu_{13}\hat{a}_3^\dagger\hat{a}_1 \tag{5.55a}$$

$$\hat{P}^{(-)}(t) = \left(\hat{P}^{(+)}(t)\right)^\dagger, \tag{5.55b}$$

and for V system,

$$\hat{P}^{(+)}(t) = \mu_{12}\hat{a}_2^\dagger\hat{a}_1 + \mu_{13}\hat{a}_3^\dagger\hat{a}_1 \tag{5.56a}$$

$$\hat{P}^{(-)}(t) = \left(\hat{P}^{(+)}(t)\right)^\dagger. \tag{5.56b}$$

With these redefinitions and a reorganization for the relaxation terms according to the similar rules outlined in Section 5.3, the key results for Ξ and V systems are summarized in Tables 5.3 through 5.10.

5.8 Implementation for Numerical Calculation

After the long and laborious derivations of the previous sections, with obscure matrices such as **M** and **N** whose complicated structure makes them uninterpretable in simple physical grounds, we are finally rewarded with the relatively straightforward implementation on the computer for numerical calculation of the spectra by means of standard matrix manipulation techniques. The program for calculating the spectra is listed in Appendix A, again using Λ system as an example. Written in Fortran programming language, the program (`Ag.f`) first reads the input parameters from the input file `A.in`, and then assigns values to the matrices **L** (`Ldc(8, 8)`) and **I** (`Idc(8)`) according to Table 5.1. After multiplying $\mathbf{L}^{-1}$ (`Li(8, 8)`) and **I** to get the steady-state density matrix elements $\psi(\infty)$ (`Fdc(8)`), the program loops through the start (`-dp1`) and stop (`dp2`) values of the probe frequency ($\omega_{p_i} - \Omega_i$) (or ($\omega - \Omega_i$) in the case of emission spectra) (`dp`), and applies Eqs. (5.49) and (5.52) to get the emission (`S1` and `S2`) and absorption (`A1` and `A2`) spectrum. Finally, the values of `S1`, `S2`, `A1` and `A2` are multiplied by the proper scaling constant and written to the

$$\frac{\partial\tilde{\rho}_{11}}{\partial t} = -iG_2\tilde{\rho}_{21} + iG_2^*\tilde{\rho}_{12} - iG_1^*\tilde{\rho}_{31} + iG_1\tilde{\rho}_{13} + 2\gamma_1\tilde{\rho}_{33} - 2\gamma_2\tilde{\rho}_{11} \quad (5.57a)$$

$$\frac{\partial\tilde{\rho}_{22}}{\partial t} = iG_2\tilde{\rho}_{21} - iG_2^*\tilde{\rho}_{12} + 2\gamma_2\tilde{\rho}_{11} + \nu_2\tilde{\rho}_{33} - \nu_1\tilde{\rho}_{22} \quad (5.57b)$$

$$\frac{\partial\tilde{\rho}_{33}}{\partial t} = iG_1^*\tilde{\rho}_{31} - iG_1\tilde{\rho}_{13} - 2\gamma_1\tilde{\rho}_{33} - \nu_2\tilde{\rho}_{33} + \nu_1\tilde{\rho}_{22} \quad (5.57c)$$

$$\frac{\partial\tilde{\rho}_{12}}{\partial t} = -iG_2(\tilde{\rho}_{22} - \tilde{\rho}_{11}) - iG_1^*\tilde{\rho}_{32} - i\Delta_2\tilde{\rho}_{12} - (\gamma_1 + \nu_1/2)\,\tilde{\rho}_{12} \quad (5.57d)$$

$$\frac{\partial\tilde{\rho}_{13}}{\partial t} = -iG_1^*(\tilde{\rho}_{33} - \tilde{\rho}_{11}) - iG_2\tilde{\rho}_{23} + i\Delta_1\tilde{\rho}_{13} - (\gamma_1 + \gamma_2 + \nu_2/2)\,\tilde{\rho}_{13} \quad (5.57e)$$

$$\frac{\partial\tilde{\rho}_{23}}{\partial t} = -iG_2^*\tilde{\rho}_{13} + iG_1^*\tilde{\rho}_{21} + i\,(\Delta_1 + \Delta_2)\,\tilde{\rho}_{23} - \left(\frac{\nu_1 + \nu_2}{2} + \gamma_1\right)\tilde{\rho}_{23} \quad (5.57f)$$

$$\tilde{\rho}_{21} = \tilde{\rho}_{12}^* \quad (5.57g)$$

$$\tilde{\rho}_{31} = \tilde{\rho}_{13}^* \quad (5.57h)$$

$$\tilde{\rho}_{32} = \tilde{\rho}_{23}^* \quad (5.57i)$$

where

$$\tilde{\rho}_{ii} = \rho_{ii} \qquad i = 1, 2, 3 \quad (5.58a)$$

$$\tilde{\rho}_{12} = \rho_{12}e^{i\Omega_2 t} \quad (5.58b)$$

$$\tilde{\rho}_{13} = \rho_{13}e^{-i\Omega_1 t} \quad (5.58c)$$

$$\tilde{\rho}_{23} = \rho_{23}e^{-i(\Omega_1+\Omega_2)t} \quad (5.58d)$$

Table 5.3: The master equation for the Ξ system

$$\frac{\partial \tilde{\rho}_{11}}{\partial t} = -iG_2^*\tilde{\rho}_{21} + iG_2^*\tilde{\rho}_{12} - iG_1^*\tilde{\rho}_{31} + iG_1\tilde{\rho}_{13} + 2\gamma_1\tilde{\rho}_{33} + 2\gamma_2\tilde{\rho}_{22} \tag{5.59a}$$

$$\frac{\partial \tilde{\rho}_{22}}{\partial t} = iG_2^*\tilde{\rho}_{21} - iG_2\tilde{\rho}_{12} - 2\gamma_2\tilde{\rho}_{22} + \nu_2\tilde{\rho}_{33} - \nu_1\tilde{\rho}_{22} \tag{5.59b}$$

$$\frac{\partial \tilde{\rho}_{33}}{\partial t} = iG_1^*\tilde{\rho}_{31} - iG_1\tilde{\rho}_{13} - 2\gamma_1\tilde{\rho}_{33} - \nu_2\tilde{\rho}_{33} + \nu_1\tilde{\rho}_{22} \tag{5.59c}$$

$$\frac{\partial \tilde{\rho}_{12}}{\partial t} = -iG_2^*(\tilde{\rho}_{22} - \tilde{\rho}_{11}) - iG_1^*\tilde{\rho}_{32} + i\Delta_2\tilde{\rho}_{12} - (\gamma_2 + \nu_1/2)\,\tilde{\rho}_{12} \tag{5.59d}$$

$$\frac{\partial \tilde{\rho}_{13}}{\partial t} = -iG_1^*(\tilde{\rho}_{33} - \tilde{\rho}_{11}) - iG_2^*\tilde{\rho}_{23} + i\Delta_1\tilde{\rho}_{13} - (\gamma_1 + \nu_2/2)\,\tilde{\rho}_{13} \tag{5.59e}$$

$$\frac{\partial \tilde{\rho}_{23}}{\partial t} = -iG_2\tilde{\rho}_{13} + iG_1^*\tilde{\rho}_{21} + i\,(\Delta_1 - \Delta_2)\,\tilde{\rho}_{23} - \left(\gamma_1 + \gamma_2 + \frac{\nu_1 + \nu_2}{2}\right)\tilde{\rho}_{23} \tag{5.59f}$$

$$\tilde{\rho}_{21} = \tilde{\rho}_{12}^* \tag{5.59g}$$

$$\tilde{\rho}_{31} = \tilde{\rho}_{13}^* \tag{5.59h}$$

$$\tilde{\rho}_{32} = \tilde{\rho}_{23}^* \tag{5.59i}$$

where

$$\tilde{\rho}_{ii} = \rho_{ii} \qquad i = 1, 2, 3 \tag{5.60a}$$

$$\tilde{\rho}_{12} = \rho_{12}e^{-i\Omega_2 t} \tag{5.60b}$$

$$\tilde{\rho}_{13} = \rho_{13}e^{-i\Omega_1 t} \tag{5.60c}$$

$$\tilde{\rho}_{23} = \rho_{23}e^{i(\Omega_2 - \Omega_1)t} \tag{5.60d}$$

Table 5.4: The master equation for the V system

Matrix Elements L_{ij} for the Ξ system									I_i
j \ i	1	2	3	4	5	6	7	8	1
1	$-2\gamma_1$ $-2\gamma_2$	iG_2^*	iG_1	$-iG_2$	$-2\gamma_1$	0	$-iG_1^*$	0	$2\gamma_1$
2	iG_2	$-i\Delta_2-$ $\gamma_2-\nu_1/2$	0	0	$-iG_2$	0	0	$-iG_1^*$	0
3	$2iG_1^*$	0	$i\Delta_1-$ $\gamma_1-\gamma_2$ $-\nu_2/2$	0	iG_1^*	$-iG_2$	0	0	$-iG_1^*$
4	$-iG_2^*$	0	0	$i\Delta_2-$ $\gamma_2-\nu_1/2$	iG_2^*	iG_1	0	0	0
5	$2\gamma_2-\nu_2$	$-iG_2^*$	0	iG_2	$-\nu_1-\nu_2$	0	0	0	ν_2
6	0	0	$-iG_2^*$	iG_1^*	0	$i\Delta_1+i\Delta_2$ $-\gamma_1-(\nu_1$ $+\nu_2)/2$	0	0	0
7	$-2iG_1$	0	0	0	$-iG_1$	0	$-i\Delta_1-$ $\gamma_1-\gamma_2$ $-\nu_2/2$	iG_2^*	iG_1
8	0	$-iG_1$	0	0	0	0	iG_2	$-i\Delta_1$ $-i\Delta_2-$ $\frac{\nu_1+\nu_2}{2}-\gamma_1$	0

Table 5.5: Matrix elements **L** and **I** for the Ξ system

Matrix Elements L_{ij} for the V system									I_i
j \ i	1	2	3	4	5	6	7	8	1
1	$-2\gamma_1$	iG_2	iG_1	$-iG_2^*$	$2\gamma_2-2\gamma_1$	0	$-iG_1^*$	0	$2\gamma_1$
2	iG_2^*	$i\Delta_2-$ $\gamma_2-\nu_1/2$	0	0	$-iG_2^*$	0	0	$-iG_1^*$	0
3	$2iG_1^*$	0	$i\Delta_1-$ $\gamma_1-\nu_2/2$	0	iG_1^*	$-iG_2^*$	0	0	$-iG_1^*$
4	$-iG_2$	0	0	$-i\Delta_2-$ $\gamma_2-\nu_1/2$	iG_2	iG_1	0	0	0
5	$-\nu_2$	$-iG_2$	0	iG_2^*	$-2\gamma_2-$ $(\nu_1+\nu_2)$	0	0	0	ν_2
6	0	0	$-iG_2$	iG_1^*	0	$i\Delta_1-i\Delta_2$ $-\gamma_1-\gamma_2$ $-\frac{\nu_1+\nu_2}{2}$	0	0	0
7	$-2iG_1$	0	0	0	$-iG_1$	0	$i\Delta_1-$ $\gamma_1-\nu_2/2$	iG_2	iG_1
8	0	$-iG_1$	0	0	0	0	iG_2^*	$i\Delta_2-i\Delta_1$ $-\gamma_1-\gamma_2$ $-\frac{\nu_1+\nu_2}{2}$	0

Table 5.6: Matrix elements **L** and **I** for the V system

(a) Replacement table of type $\left\langle \hat{a}_i^\dagger \hat{a}_j \hat{P}^{(+)} \right\rangle_\tau$ for the Ξ system			
$\psi_1(\tau)$	$\longrightarrow$	$\left\langle \hat{a}_1^\dagger \hat{a}_1 \hat{P}^{(+)} \right\rangle_\tau$	$= \mu_{13} e^{-i\Omega_1 \tau} \psi_7(\tau)$
$\psi_2(\tau)$	$\longrightarrow$	$e^{i\Omega_2 \tau} \left\langle \hat{a}_2^\dagger \hat{a}_1 \hat{P}^{(+)} \right\rangle_\tau$	$= \mu_{13} e^{-i\Omega_1 \tau} \psi_8(\tau)$
$\psi_3(\tau)$	$\longrightarrow$	$e^{-i\Omega_1 \tau} \left\langle \hat{a}_3^\dagger \hat{a}_1 \hat{P}^{(+)} \right\rangle_\tau$	$= \mu_{13} e^{-i\Omega_1 \tau} \left(1 - \psi_1(\tau) - \psi_5(\tau)\right)$
$\psi_4(\tau)$	$\longrightarrow$	$e^{-i\Omega_2 \tau} \left\langle \hat{a}_1^\dagger \hat{a}_2 \hat{P}^{(+)} \right\rangle_\tau$	$= \mu_{12} e^{-i\Omega_2 \tau} \psi_1(\tau)$
$\psi_5(\tau)$	$\longrightarrow$	$\left\langle \hat{a}_2^\dagger \hat{a}_2 \hat{P}^{(+)} \right\rangle_\tau$	$= \mu_{12} e^{-i\Omega_2 \tau} \psi_2(\tau)$
$\psi_6(\tau)$	$\longrightarrow$	$e^{-i(\Omega_1+\Omega_2)\tau} \left\langle \hat{a}_3^\dagger \hat{a}_2 \hat{P}^{(+)} \right\rangle_\tau$	$= \mu_{12} e^{-i\Omega_2 \tau} \psi_3(\tau)$
$\psi_7(\tau)$	$\longrightarrow$	$e^{i\Omega_1 \tau} \left\langle \hat{a}_3^\dagger \hat{a}_1 \hat{P}^{(+)} \right\rangle_\tau$	$= 0$
$\psi_8(\tau)$	$\longrightarrow$	$e^{i(\Omega_1+\Omega_2)\tau} \left\langle \hat{a}_2^\dagger \hat{a}_3 \hat{P}^{(+)} \right\rangle_\tau$	$= \mu_{13} e^{-i\Omega_1 \tau} \psi_2(\tau)$
$\langle \mathbf{1} \rangle_\tau$	$\longrightarrow$	$\left\langle \hat{P}^{(+)} \right\rangle_\tau$	$= \mu_{12} e^{-i\Omega_2 \tau} \psi_2(\tau) + \mu_{13} e^{-i\Omega_1 \tau} \psi_7(\tau)$

(b) Replacement table of type $\left\langle \hat{P}^{(+)} \hat{a}_i^\dagger \hat{a}_j \right\rangle_\tau$ for the Ξ system			
$\psi_1(\tau)$	$\longrightarrow$	$\left\langle \hat{P}^{(+)} \hat{a}_1^\dagger \hat{a}_1 \right\rangle_\tau$	$= \mu_{12} e^{-i\Omega_2 \tau} \psi_2(\tau)$
$\psi_2(\tau)$	$\longrightarrow$	$e^{i\Omega_2 \tau} \left\langle \hat{P}^{(+)} \hat{a}_2^\dagger \hat{a}_1 \right\rangle_\tau$	$= 0$
$\psi_3(\tau)$	$\longrightarrow$	$e^{-i\Omega_1 \tau} \left\langle \hat{P}^{(+)} \hat{a}_3^\dagger \hat{a}_1 \right\rangle_\tau$	$= \mu_{13} e^{-i\Omega_1 \tau} \psi_1(\tau)$
$\psi_4(\tau)$	$\longrightarrow$	$e^{-i\Omega_2 \tau} \left\langle \hat{P}^{(+)} \hat{a}_1^\dagger \hat{a}_2 \right\rangle_\tau$	$= \mu_{12} e^{-i\Omega_2 \tau} \psi_5(\tau)$
$\psi_5(\tau)$	$\longrightarrow$	$\left\langle \hat{P}^{(+)} \hat{a}_2^\dagger \hat{a}_2 \right\rangle_\tau$	$= 0$
$\psi_6(\tau)$	$\longrightarrow$	$e^{-i(\Omega_1+\Omega_2)\tau} \left\langle \hat{P}^{(+)} \hat{a}_3^\dagger \hat{a}_2 \right\rangle_\tau$	$= \mu_{13} e^{-i\Omega_1 \tau} \psi_4(\tau)$
$\psi_7(\tau)$	$\longrightarrow$	$e^{i\Omega_1 \tau} \left\langle \hat{P}^{(+)} \hat{a}_3^\dagger \hat{a}_1 \right\rangle_\tau$	$= \mu_{12} e^{-i\Omega_2 \tau} \psi_8(\tau)$
$\psi_8(\tau)$	$\longrightarrow$	$e^{i(\Omega_1+\Omega_2)\tau} \left\langle \hat{P}^{(+)} \hat{a}_2^\dagger \hat{a}_3 \right\rangle_\tau$	$= 0$
$\langle \mathbf{1} \rangle_\tau$	$\longrightarrow$	$\left\langle \hat{P}^{(+)} \right\rangle_\tau$	$= \mu_{12} e^{-i\Omega_2 \tau} \psi_2(\tau) + \mu_{13} e^{-i\Omega_1 \tau} \psi_7(\tau)$

Table 5.7: The complete replacement table for the Ξ system

(a) Replacement table of type $\left\langle \hat{a}_i^\dagger \hat{a}_j \hat{P}^{(+)} \right\rangle_\tau$ for the V system			
$\psi_1(\tau)$	$\longrightarrow$	$\left\langle \hat{a}_1^\dagger \hat{a}_1 \hat{P}^{(+)} \right\rangle_\tau$	$= \mu_{12} e^{-i\Omega_2 \tau} \psi_4(\tau) + \mu_{13} e^{-i\Omega_1 \tau} \psi_7(\tau)$
$\psi_2(\tau)$	$\longrightarrow$	$e^{-i\Omega_2 \tau} \left\langle \hat{a}_2^\dagger \hat{a}_1 \hat{P}^{(+)} \right\rangle_\tau$	$= \mu_{12} e^{-i\Omega_2 \tau} \psi_5(\tau) + \mu_{13} e^{-i\Omega_1 \tau} \psi_8(\tau)$
$\psi_3(\tau)$	$\longrightarrow$	$e^{-i\Omega_1 \tau} \left\langle \hat{a}_3^\dagger \hat{a}_1 \hat{P}^{(+)} \right\rangle_\tau$	$= \mu_{12} e^{-i\Omega_2 \tau} \psi_6(\tau) + \mu_{13} e^{-i\Omega_1 \tau} \times$ $(1 - \psi_1(\tau) - \psi_5(\tau))$
$\psi_4(\tau)$	$\longrightarrow$	$e^{i\Omega_2 \tau} \left\langle \hat{a}_1^\dagger \hat{a}_2 \hat{P}^{(+)} \right\rangle_\tau$	$= 0$
$\psi_5(\tau)$	$\longrightarrow$	$\left\langle \hat{a}_2^\dagger \hat{a}_2 \hat{P}^{(+)} \right\rangle_\tau$	$= 0$
$\psi_6(\tau)$	$\longrightarrow$	$e^{i(\Omega_2 - \Omega_1)\tau} \left\langle \hat{a}_3^\dagger \hat{a}_2 \hat{P}^{(+)} \right\rangle_\tau$	$= 0$
$\psi_7(\tau)$	$\longrightarrow$	$e^{i\Omega_1 \tau} \left\langle \hat{a}_3^\dagger \hat{a}_1 \hat{P}^{(+)} \right\rangle_\tau$	$= 0$
$\psi_8(\tau)$	$\longrightarrow$	$e^{-i(\Omega_2 - \Omega_1)\tau} \left\langle \hat{a}_2^\dagger \hat{a}_3 \hat{P}^{(+)} \right\rangle_\tau$	$= 0$
$\langle \mathbf{1} \rangle_\tau$	$\longrightarrow$	$\left\langle \hat{P}^{(+)} \right\rangle_\tau$	$= \mu_{12} e^{-i\Omega_2 \tau} \psi_4(\tau) + \mu_{13} e^{-i\Omega_1 \tau} \psi_7(\tau)$

(b) Replacement table of type $\left\langle \hat{P}^{(+)} \hat{a}_i^\dagger \hat{a}_j \right\rangle_\tau$ for the V system			
$\psi_1(\tau)$	$\longrightarrow$	$\left\langle \hat{P}^{(+)} \hat{a}_1^\dagger \hat{a}_1 \right\rangle_\tau$	$= 0$
$\psi_2(\tau)$	$\longrightarrow$	$e^{-i\Omega_2 \tau} \left\langle \hat{P}^{(+)} \hat{a}_2^\dagger \hat{a}_1 \right\rangle_\tau$	$= \mu_{12} e^{-i\Omega_2 \tau} \psi_1(\tau)$
$\psi_3(\tau)$	$\longrightarrow$	$e^{-i\Omega_1 \tau} \left\langle \hat{P}^{(+)} \hat{a}_3^\dagger \hat{a}_1 \right\rangle_\tau$	$= \mu_{13} e^{-i\Omega_1 \tau} \psi_1(\tau)$
$\psi_4(\tau)$	$\longrightarrow$	$e^{i\Omega_2 \tau} \left\langle \hat{P}^{(+)} \hat{a}_1^\dagger \hat{a}_2 \right\rangle_\tau$	$= 0$
$\psi_5(\tau)$	$\longrightarrow$	$\left\langle \hat{P}^{(+)} \hat{a}_2^\dagger \hat{a}_2 \right\rangle_\tau$	$= \mu_{12} e^{-i\Omega_2 \tau} \psi_4(\tau)$
$\psi_6(\tau)$	$\longrightarrow$	$e^{i(\Omega_2 - \Omega_1)\tau} \left\langle \hat{P}^{(+)} \hat{a}_3^\dagger \hat{a}_2 \right\rangle_\tau$	$= \mu_{13} e^{-i\Omega_1 \tau} \psi_4(\tau)$
$\psi_7(\tau)$	$\longrightarrow$	$e^{i\Omega_1 \tau} \left\langle \hat{P}^{(+)} \hat{a}_3^\dagger \hat{a}_1 \right\rangle_\tau$	$= 0$
$\psi_8(\tau)$	$\longrightarrow$	$e^{-i(\Omega_2 - \Omega_1)\tau} \left\langle \hat{P}^{(+)} \hat{a}_2^\dagger \hat{a}_3 \right\rangle_\tau$	$= \mu_{13} e^{-i\Omega_1 \tau} \psi_7(\tau)$
$\langle \mathbf{1} \rangle_\tau$	$\longrightarrow$	$\left\langle \hat{P}^{(+)} \right\rangle_\tau$	$= \mu_{12} e^{-i\Omega_2 \tau} \psi_4(\tau) + \mu_{13} e^{-i\Omega_1 \tau} \psi_7(\tau)$

Table 5.8: The complete replacement table for the V system

$$S_1^{\text{incoh}}(\omega) = \text{Re}\Big\{ M_{31}(i\omega - i\Omega_1)\psi_7(\infty) + M_{32}(i\omega - i\Omega_1)\psi_8(\infty) + M_{33}(i\omega - i\Omega_1)(1 - \psi_1(\infty) - \psi_5(\infty)) + \sum_j N_{3j}(i\omega - i\Omega_1) I_j \psi_7(\infty) \Big\} \quad (5.61a)$$

$$S_2^{\text{incoh}}(\omega) = \text{Re}\Big\{ M_{44}(i\omega - i\Omega_2)\psi_1(\infty) + M_{45}(i\omega - i\Omega_2)\psi_2(\infty) + M_{46}(i\omega - i\Omega_2)\psi_3(\infty) + \sum_j N_{4j}(i\omega - i\Omega_2) I_j \psi_2(\infty) \Big\} \quad (5.61b)$$

$$A_1(\omega_{p_1}) = \text{Re}\Big\{ M_{31}(i\omega_{p_1} - i\Omega_1)\psi_7(\infty) + M_{32}(i\omega_{p_1} - i\Omega_1)\psi_8(\infty) - M_{36}(i\omega_{p_1} - i\Omega_1)\psi_4(\infty) + M_{33}(i\omega_{p_1} - i\Omega_1)(1 - 2\psi_1(\infty) - \psi_5(\infty)) \Big\} \quad (5.62a)$$

$$A_2(\omega_{p_2}) = \text{Re}\Big\{ M_{44}(i\omega_{p_2} - i\Omega_2)\psi_1(\infty) + M_{45}(i\omega_{p_2} - i\Omega_2)\psi_2(\infty) + M_{46}(i\omega_{p_2} - i\Omega_2)\psi_3(\infty) - M_{41}(i\omega_{p_2} - i\Omega_2)\psi_2(\infty) - M_{44}(i\omega_{p_2} - i\Omega_2)\psi_5(\infty) - M_{47}(i\omega_{p_2} - i\Omega_2)\psi_8(\infty) \Big\} \quad (5.62b)$$

Table 5.9: The equations for absorption and emission spectrum for the Ξ system

$$S_1^{\text{incoh}}(\omega) = \text{Re}\Big\{ M_{31}(i\omega - i\Omega_1)\psi_7(\infty) + M_{32}(i\omega - i\Omega_1)\psi_8(\infty) + M_{33}(i\omega - i\Omega_1)(1 - \psi_1(\infty) - \psi_5(\infty)) + \sum_j N_{3j}(i\omega - i\Omega_1) I_j \psi_7(\infty) \Big\} \quad (5.63a)$$

$$S_2^{\text{incoh}}(\omega) = \text{Re}\Big\{ M_{21}(i\omega - i\Omega_2)\psi_4(\infty) + M_{22}(i\omega - i\Omega_2)\psi_5(\infty) + M_{23}(i\omega - i\Omega_2)\psi_6(\infty) + \sum_j N_{2j}(i\omega - i\Omega_2) I_j \psi_4(\infty) \Big\} \quad (5.63b)$$

$$A_1(\omega_{p_1}) = \text{Re}\Big\{ M_{31}(i\omega_{p_1} - i\Omega_1)\psi_7(\infty) + M_{32}(i\omega_{p_1} - i\Omega_1)\psi_8(\infty) - M_{36}(i\omega_{p_1} - i\Omega_1)\psi_4(\infty) + M_{33}(i\omega_{p_1} - i\Omega_1)(1 - 2\psi_1(\infty) - \psi_5(\infty)) \Big\} \quad (5.64a)$$

$$A_2(\omega_{p_2}) = \text{Re}\Big\{ M_{21}(i\omega_{p_2} - i\Omega_2)\psi_4(\infty) + M_{22}(i\omega_{p_2} - i\Omega_2)\psi_5(\infty) + M_{23}(i\omega_{p_2} - i\Omega_2)\psi_6(\infty) - M_{22}(i\omega_{p_2} - i\Omega_2)\psi_1(\infty) - M_{25}(i\omega_{p_2} - i\Omega_2)\psi_4(\infty) - M_{28}(i\omega_{p_2} - i\Omega_2)\psi_7(\infty) \Big\} \quad (5.64b)$$

Table 5.10: The equations for absorption and emission spectrum for the V system

output file (e.g., `Ag.data/A1.*` for absorption spectrum of level $1 \leftrightarrow 3$).

The scaling constants are determined by the normalization. In our program, we have multiplied the absorption spectra $A_i(\omega_{p_i})$ by the relevant decay rates γ_i so that

$$\gamma_i A_i\left(\omega_{p_i}\right) = \frac{\sigma_{A_i}\left(\omega_{p_i}\right)}{\sigma_0} = \tilde{\sigma}_{A_i}\left(\omega_{p_i}\right) \tag{5.65}$$

where $\sigma_0 = (3/2\pi)\lambda_i^2$ is the maximum absorption cross section for a weak laser beam exactly on resonance with the atomic transition. Thus the resultant dimensionless $\tilde{\sigma}_{A_i}(\omega_{p_i})$ is the (frequency-resolved) absorption cross section for the probe beam at frequency ω_{p_i} (normalized to σ_0). Such a cross section can be easily converted into "real" absorption spectrum p_1/p_0 measured in the experiment (like those shown in Fig. 4.2) by multiplying the optical thickness of the trap nl and using the Beer's law $p_1/p_0 = e^{-n\sigma_A l}$.

The normalization for $S_i^{\text{incoh}}(\omega)$ is not important in this thesis, thus no scaling constant is applied to emission spectrum. It is perhaps worthwhile to point out that there are some simple relationships between the integrated absorption and emission spectrum ($\int_0^\infty A_i(\omega_{p_i})\, d\omega_{p_i}$ and $\int_0^\infty S_i^{\text{total}}(\omega)\, d\omega$) and the density matrix elements, e.g., for the transition $1 \leftrightarrow 2$ in the Λ system:

$$2\int_0^\infty A_2\left(\omega_{p_2}\right)\, d\omega_{p_2} = 2\pi\left(\rho_{11} - \rho_{22}\right) \tag{5.66a}$$

$$2\int_0^\infty S_2^{\text{total}}(\omega)\, d\omega = 2\pi\rho_{11} \tag{5.66b}$$

$$2S_2^{\text{coh}}(\omega) = 2\pi\left|\rho_{12}\right|^2 \delta\left(\omega - \Omega_2\right), \tag{5.66c}$$

which comes directly from Eqs. (5.4) and (5.5). These are simply extensions of the familiar two-level results which state that the total absorption cross section is proportional to the population difference between the upper and lower level of the transition, and the total emission rate is proportional only to the upper state population.

Before going on to discuss the general result of the spectra, we need to make connections to experimental parameters. Our convention is to reference all our pa-

rameters to one of the decay rates, e.g., γ_2 (setting $\gamma_2 = 1$). Thus if transition $1 \leftrightarrow 2$ refers to the Cs transition of $6S_{1/2}, F = 4, m_F = 4 \leftrightarrow 6P_{3/2}, F' = 5, m_{F'} = 5$ having natural linewidth of 5 MHz ($= 2\gamma_2/2\pi$), then $\Delta_2 = 5.5$ would mean a pump detuning of 14 MHz. The Rabi frequency G_i defined in Eq. (5.12) is related to the intensity of the driving field by:

$$\frac{I_i}{I_{i_s}} = \frac{2G_i^2}{\gamma_i^2}, \tag{5.67}$$

where I_{i_s} is the saturation intensity for the relevant transition. Thus, in the above example where $I_{2_s} = 1$ mW/cm^2, $G_2 = 1.5$ would mean a pump intensity of 4.5 mW/cm^2.

We are now finally ready to reap the reward of our meticulous calculations in the previous sections.

5.9 Results and Discussions

5.9.1 General Features

As a check of our results, we have used our program for three-level spectra to reproduce the two-level results shown in Fig. 4.3(c). By setting $\gamma_2 = 0$ in a Λ system [Fig. 5.2(a)], we have effectively turned off the $1 \leftrightarrow 2$ transition and the transition $1 \leftrightarrow 3$ is precisely a two-state transition. The emission spectra for the same system is shown in Fig. 5.2(b), where we see a triplet structure separated by the generalized Rabi frequency G'. This socalled "Mollow triplet" is also easily explained in the dressed state picture (cf. Fig. 4.3(d) and Section 4.2). It is also worthwhile to note that by setting proper parameters, e.g., a nonzero γ_2 and ν_2, our three-level system can also reproduce the "open" two-level system shown in Fig. 4.3(b).

Next as we turn to three level, a remarkable feature is that the absorption spectra develop double absorption peaks at high Rabi frequency, as evidenced in Fig. 5.3(b) and Fig. 5.3(d). This is called the Autler-Townes doublet[97] and can again be understood in the dressed-atom picture. Another difference with the two-level system is that the emission spectra show five peaks instead of three [cf. Fig. 5.3(c) and

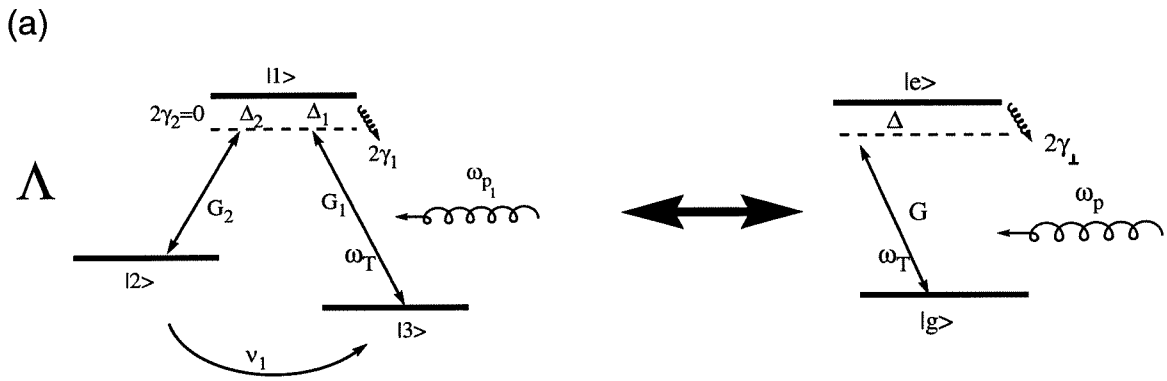

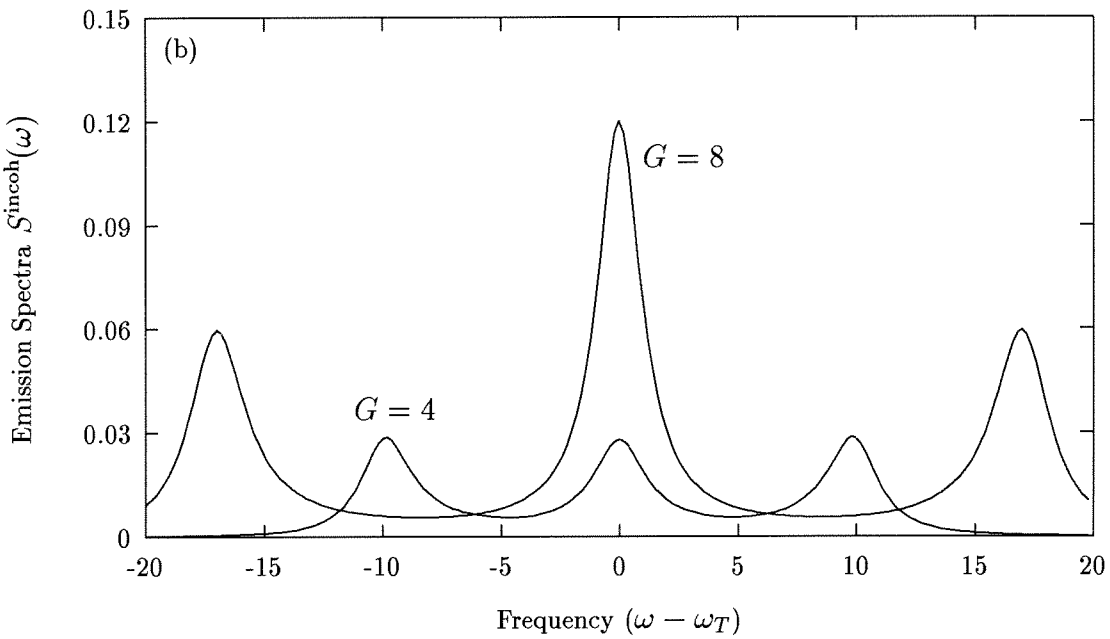

Figure 5.2: The (incoherent part of the) emission spectra for a two-level atom. (a) A Λ system with $\gamma_2 = 0$ is equivalent to a two-level system. (b) The (incoherent part of the) emission spectra for a two-level atom with $\gamma_\perp = 1$, $\Delta = 6$ and $G = 4, 8$, obtained from the $1 \leftrightarrow 3$ (incoherent) emission spectra of a Λ system with $G_1 = 4, 8$, $G_2 = 0$, $\Delta_1 = 6.0$, $\Delta_2 = 5.5$, $\gamma_1 = 1.0$, γ_2=0, $\nu_1 = 1$, and $\nu_2 = 0$.

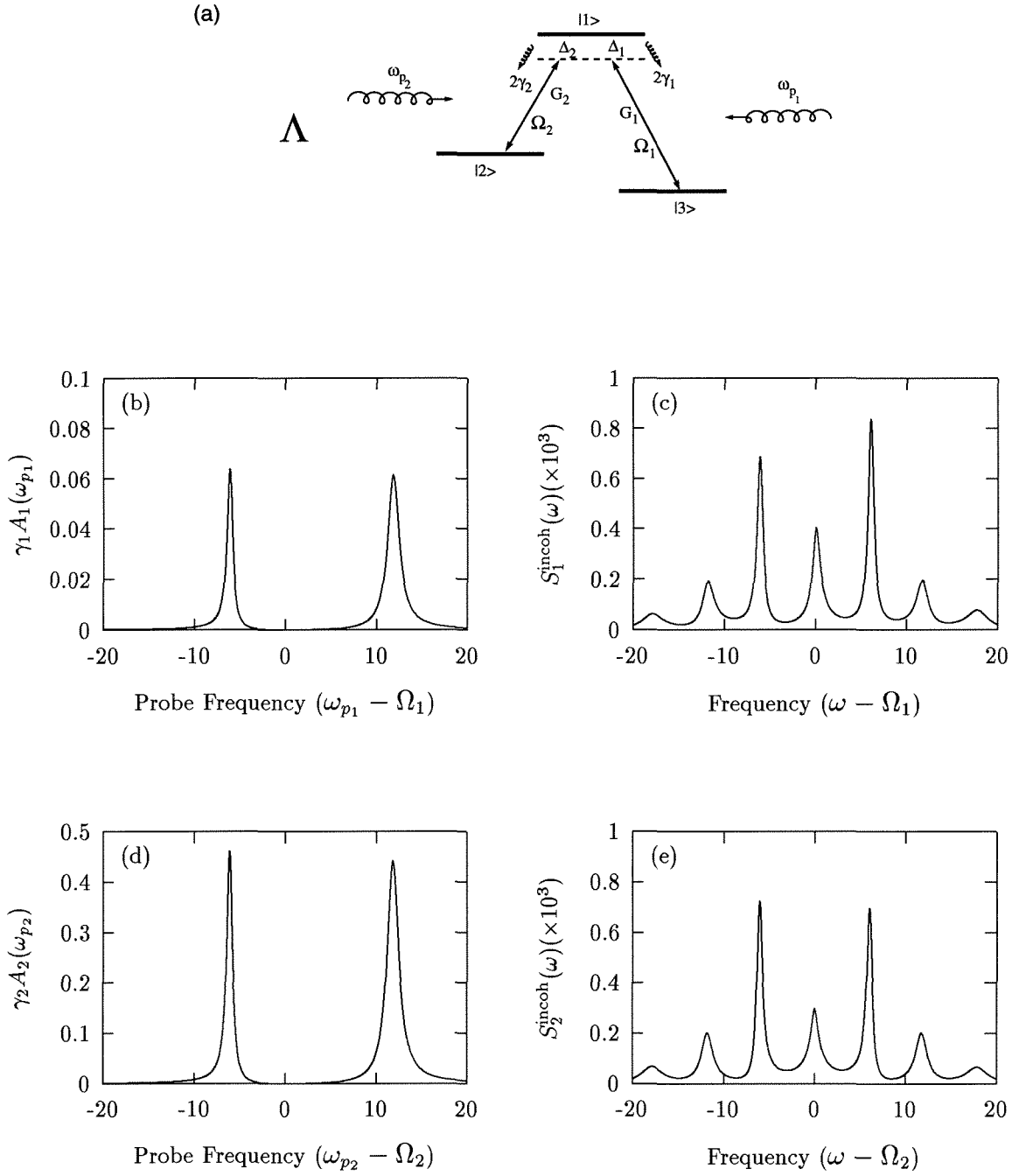

Figure 5.3: Absorption and (incoherent part of the) emission spectra for a Λ system with parameters $G_1 = 6$, $G_2 = 6$, $\Delta_1 = 6$, $\Delta_2 = 5.5$, $\gamma_1 = 0.15$, $\gamma_2 = 1.0$, and $\nu_1 = \nu_2 = 0$. The emission spectra [(c), (e)] show five peaks, while the absorption spectra [(b), (d)] show double peaks characteristic of Autler-Townes effect.

Fig. 5.3(e)]. This is because in three-level systems, the dressed state splitting of the atomic levels can generally support up to five spectral components.[86]

One more unique feature of the three-level system is that the width of the fluorescence spectrum can become narrower than predicted by the standard theory of resonance fluorescence.[75] As explained in Ref. [86], this is because the spontaneous decay rate of each atomic transition in the presence of the two driving fields becomes a linear superposition of all decay rates γ_i connecting the levels of interest, with weighting factors that depend on the relative magnitude of the Rabi frequency. As a result, the spectral linewidth of the emission spectrum can become narrower than the natural linewidth of the upper state of the transition. This is studied experimentally by Mossberg and coworkers[98] and their result in a three-level Ba atom is in good agreement with the prediction of Ref. [86].

As of our own calculation, we have discovered that under some conditions, the probe-absorption spectrum of the upper transition $1 \leftrightarrow 3$ in a Ξ system does not reflect the linewidth of the lower level (level 1) of the transition. Fig. 5.4(a) illustrates an ordinary case where the lower transition $1 \leftrightarrow 2$ is turned off ($G_2 = 0$), and population lost to the lower transition is put back to the upper transition by setting $\nu_1 = 1$. Thus the upper transition $1 \leftrightarrow 3$ is very close to the "open" two-level system illustrated in Fig. 4.3(b). Under a weak driving field ($G_1 = 0.01 \ll \gamma_1, \gamma_2$), the absorption spectrum has a FWHM equal to twice the sum of the decay rates for the upper and lower levels, $2(\gamma_1 + \gamma_2) = 3$. If, on the other hand, we examine a "real" three-level system by turning on the lower transition ($G_2 = 0.01$) and eliminating the population transfer rates ν_1 from the ground (level 2) to the excited state (level 3), we see that the width of the absorption spectrum is now determined by the upper state decay rate γ_1 alone rather than the sum of γ_1 and γ_2. We speculate that this is also due to some "coherent mixing" of the atomic levels involved because of the crucial role the driving fields play here.

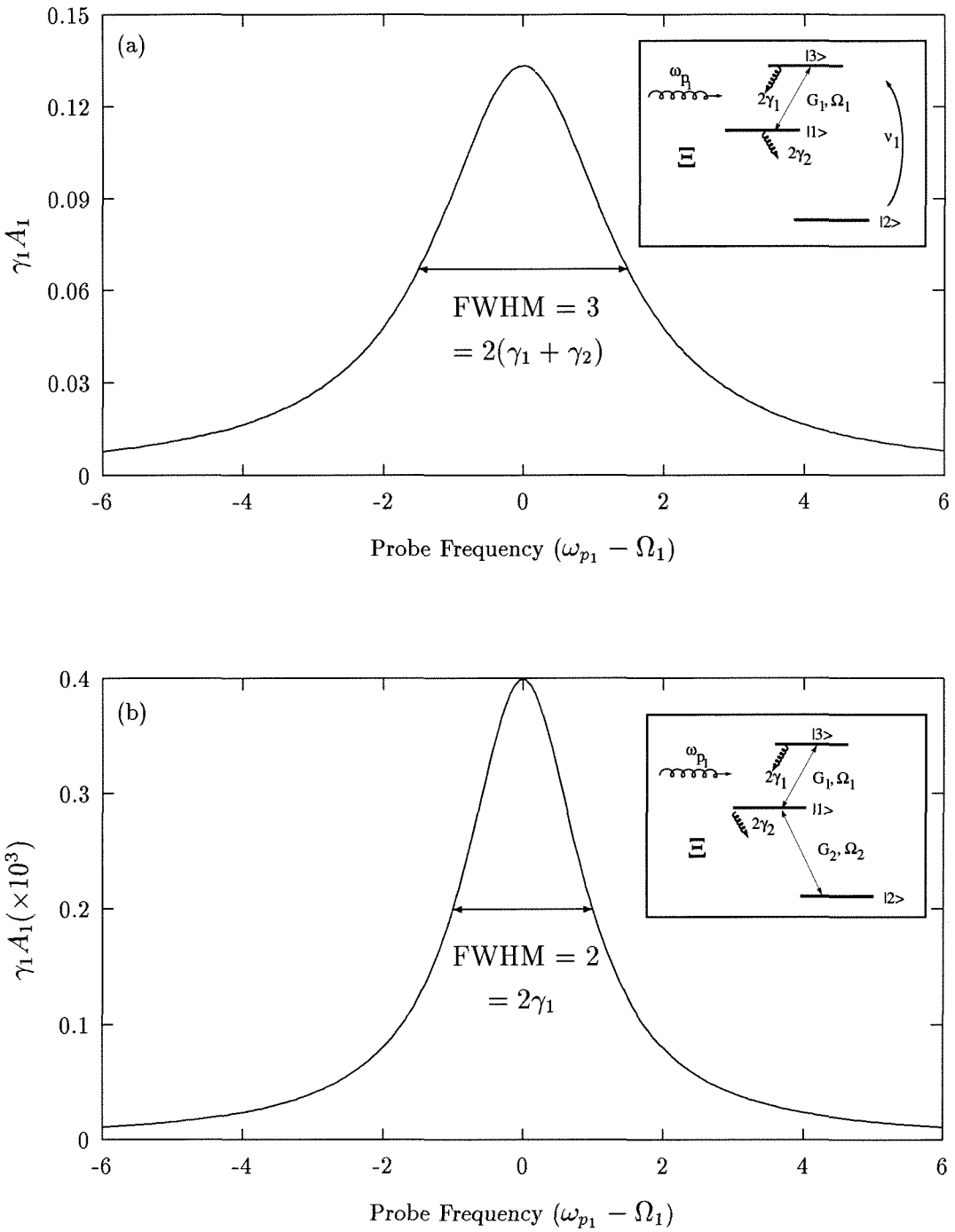

Figure 5.4: Absorption spectra for Ξ systems on resonance with weak driving field. (a) Absorption spectrum for the $1 \leftrightarrow 3$ transition of a Ξ system with parameters $G_1 = 0.01$, $G_2 = 0$, $\Delta_1 = \Delta_2 = 0$, $\gamma_1 = 1$, $\gamma_2 = 0.5$, $\nu_1 = 1$, $\nu_2 = 0$, the FWHM of the transition is $2(\gamma_1 + \gamma_2)$. (b) Absorption spectrum for the $1 \leftrightarrow 3$ transition of a Ξ system with parameters $G_1 = G_2 = 0.01$, $\Delta_1 = \Delta_2 = 0$, $\gamma_1 = 1$, $\gamma_2 = 0.5$, $\nu_1 = \nu_2 = 0$, the FWHM of the transition is $2\gamma_1$.

5.9.2 Narrow Resonances in Three-Level Λ Systems

As a principal motivation for deriving the three-level spectra, we will now attempt to identify a three-level configuration which would exhibit narrow gains and absorptions near the frequency of the driving field in addition to the usual broad absorption peak. It is well known that narrow resonances will occur in a Λ system if the frequency difference between the pump and probe beam coincides with the ground state splitting.[99] In Figs. 5.5(b) and (c) we have sketched the absorption spectra for a Λ system having detunings $\Delta_1 = 6$ and $\Delta_2 = 5.5$ [Fig. 5.5(a)]. If we assume the same pump frequency for both transitions ($\Omega_1 = \Omega_2 = \omega_T$), then the difference in detuning ($\Delta_1 - \Delta_2$) represents the ground state splitting. The $1 \leftrightarrow 2$ transition is the main transition with $\gamma_2 = 1.0$ and $G_2 = 1.5$. We already calculated in Section 5.8 that this would mean a detuning of about 14 MHz and a total pump intensity of 4.5 mW/cm^2 if $1 \leftrightarrow 2$ transition represents the Cs $6S_{1/2}, F = 4, m_F = 4 \leftrightarrow 6P_{3/2}, F' = 5, m_{F'} = 5$ transition. The transition $1 \leftrightarrow 3$, with $\gamma_1 = 0.15$ and $G_1 = 0.1$ is a perturbation for the main transition between levels 1 and 2. There is no direct population transfer between the ground states levels 2 and 3 ($\nu_1 = \nu_2 = 0$). The correspondence of this model with the spectroscopy experiment in the previous chapter is presumably that the ground state splitting arises from small Doppler shifts, from the spatially dependent Zeeman splitting across the trap, and from local variations in light shifts. Mixing of ground state coherence and population might be driven by atomic motion through the polarization gradients of the trap. From Fig. 5.5 we see that narrow resonances with the correct symmetry occurs in the $1 \leftrightarrow 2$ transition [Fig. 5.5(c)], while only a narrow absorption peak is evident in the $1 \leftrightarrow 3$ spectrum [Fig. 5.5(b)]. To compare with the experiment we have summed the spectra $\tilde{\sigma}_{A_1}(\omega_{p_1})$, $\tilde{\sigma}_{A_2}(\omega_{p_2})$ and used the Beer's law $p_1/p_0 = \exp\left[-nl\sigma_0\left(\tilde{\sigma}_{A_1} + \tilde{\sigma}_{A_2}\right)\right]$ to convert it into real absorption measured by the ratio of the incident and transmitted probe power (p_1/p_0), and the result is shown in Figs. 5.5(d) and (e). Although they agree qualitatively with the experiment (cf. Fig. 4.2), there are several discrepancies, e.g., the narrow resonances only occur for a limited range of Rabi frequency G_2. This contradicts directly with

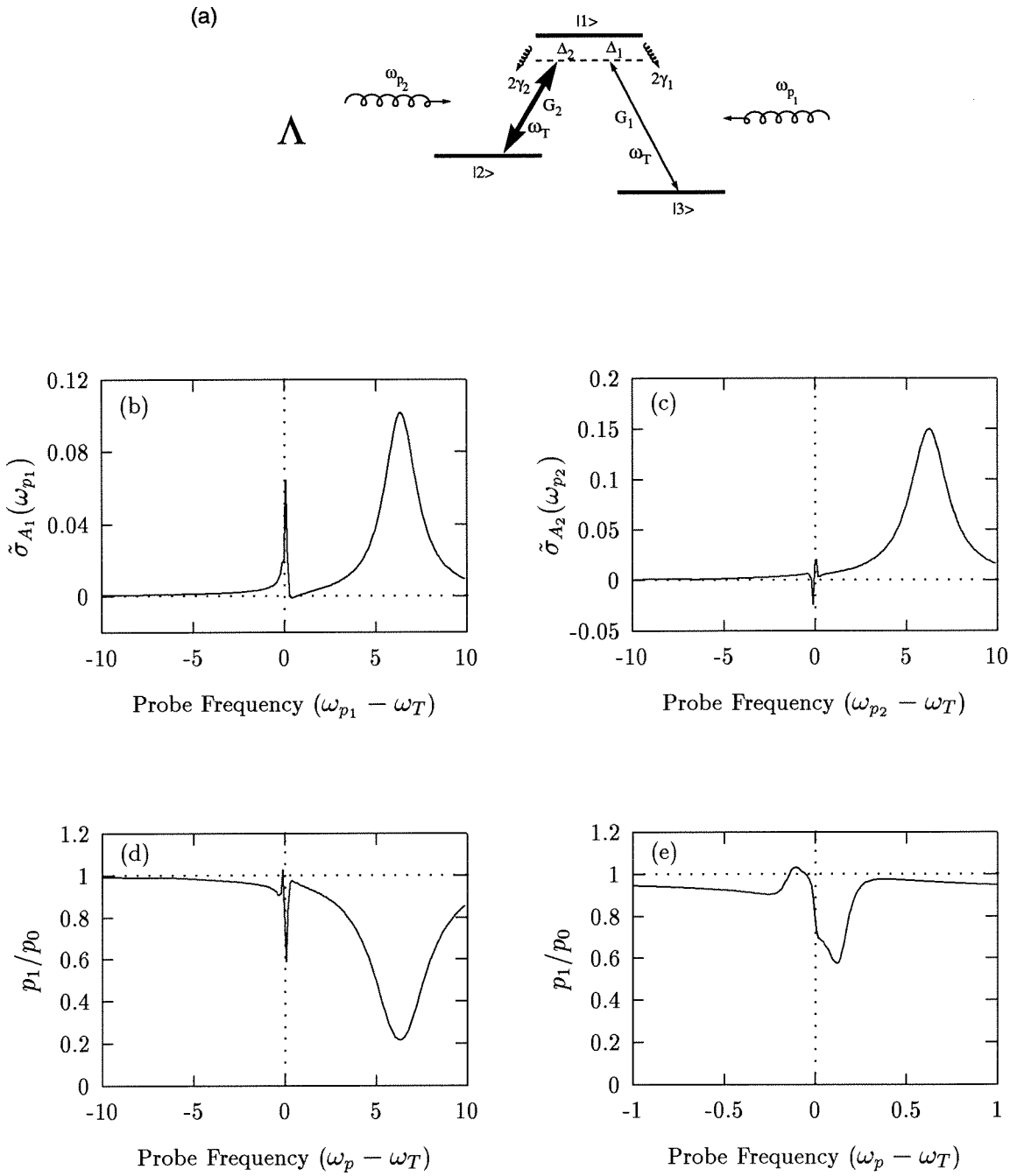

Figure 5.5: A Λ system which exhibits narrow gain. (b), (c) The absorption spectra $\tilde{\sigma}_{A_1}$ and $\tilde{\sigma}_{A_2}$ for a Λ system with parameters $G_1 = 0.1$, $G_2 = 1.5$, $\Delta_1 = 6.0$, $\Delta_2 = 5.5$, $\gamma_1 = 0.15$, $\gamma_2 = 1$, and $\nu_1 = \nu_2 = 0$. The negative values of $\tilde{\sigma}_A$ correspond to gain. (d) the probe transmission $p_1/p_0 = \exp[-nl\sigma_0(\tilde{\sigma}_{A_1} + \tilde{\sigma}_{A_2})]$, where $nl\sigma_0 = 6.1$. (e) the center part of (d).

the experimental fact that the narrow feature is robust for a wide range of pump intensities [Figs. 4.2(c)-(e)]. This vulnerability is also responsible for the fact that we were not able to obtain broad gain in Fig. 5.5(d), because in order to do so we would need to increase the Rabi frequencies G_1 and G_2 to such an extent that the Autler-Townes effect associated with the high pump intensities would destroy the narrow feature (cf. Fig. 5.3).

In addition to these apparent contradictions with the experiment, such a three-level theory is necessarily unsatisfactory because it is a dramatic simplification of the real situation in the trap. The ground state splitting, the parameters of the "perturbative" transition $1 \leftrightarrow 3$ are all put in phenomenologically. But despite such weakness the simplicity of the three-level theory offers us a way to understand the narrow resonances which is not accounted for in the two-level theory. The fact that the three-level theory still does not explain all the features in the spectra would only enforce the notion that the trap lives in a complex microscopic environment and the dynamics of the trap are driven collectively by the sum of all the different aspects of such an environment.

5.9.3 Introduction to Negative Radiation Pressure

Instead of attempting to construct a more complex theory to take into account all the energy levels involved, (Ref. [85] represents a serious attempt to obtain a quantitative comparison between theory and experiment with no fitting parameters,) we will stay in the three-level regime and try to explore new experimental configurations the three-level spectra offer. One such possibility is the negative radiation pressure we suggested by the end of Section 4.3. The "radiation pressure force" is the force arising from the atoms reradiating absorbed photons which are subsequently scattered a second time by other atoms. As demonstrated in a beautiful set of experiments by C. Wieman's group at JILA,[58] conventional radiation pressure leads to a long range repulsive force in an optically dense sample. For example, in Fig. 5.6(a), atom 2 absorbs the photon emitted from atom 1, and thus receives a momentum kick of $\hbar\mathbf{k}$ in the same

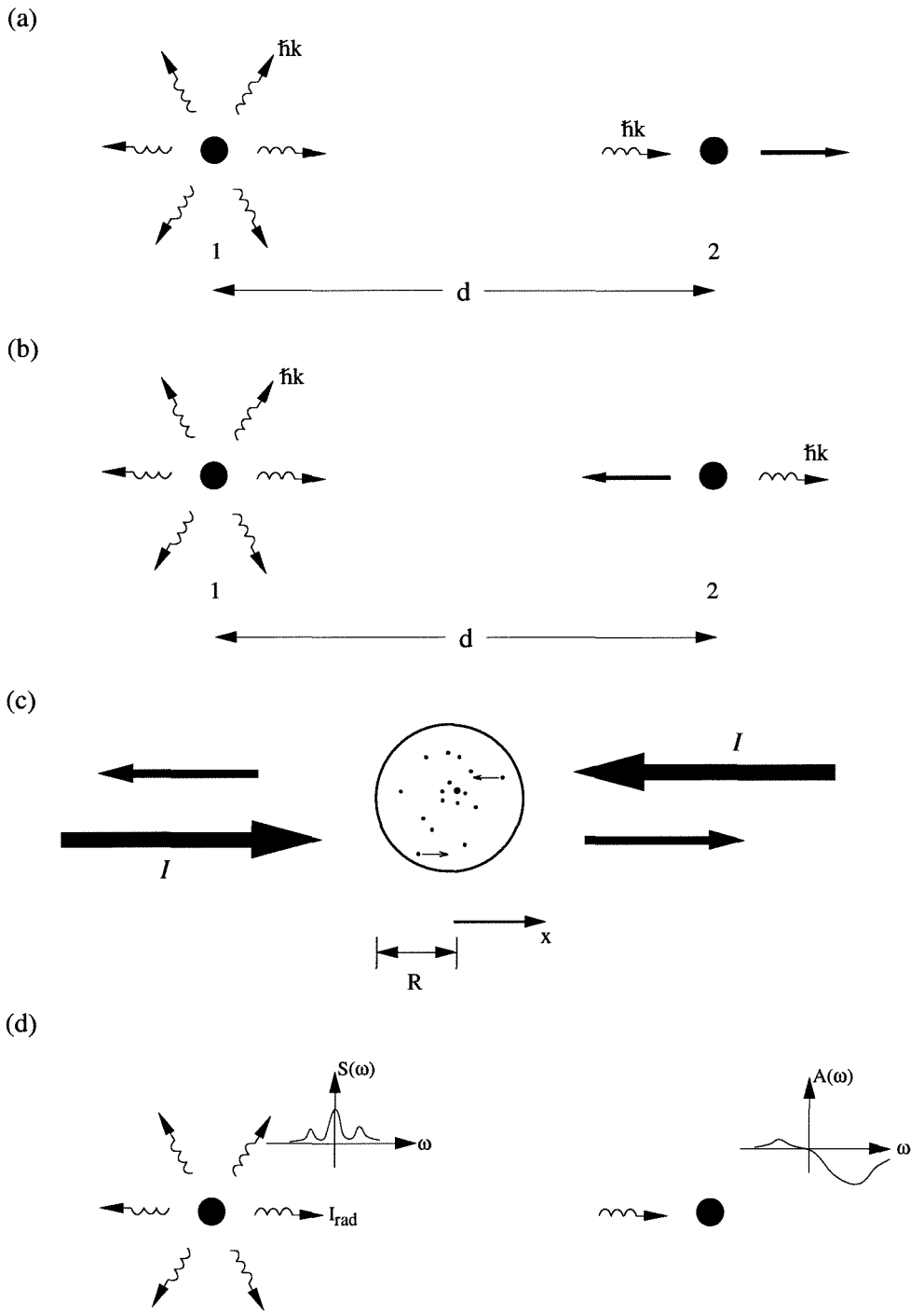

Figure 5.6: Radiation pressures force and attenuation force. (a) Positive radiation pressure (b) Negative radiation pressure (c) Attenuation force (d) The integrated absorption cross section for scattered light.

direction of the photon coming from atom 1. The resultant movement of atom 2 is away from atom 1, and thus the radiation pressure is positive. In traps such as ours, this repulsive force is as large as the Zeeman-shift restoring force and must be taken into account in any analysis of the trap dynamics. Indeed, as discussed in detail in Ref. [58] and confirmed by Ref. [100] using a more rigorous approach, steady-state configurations are determined by a balance among the following forces: (i) the (attractive) Zeeman-shift restoring force, (ii) the (repulsive) force due to radiation pressure, and (iii) the (attractive) force associated with attenuation of the trapping beams in propagation through the trap.[87] The net result of these three forces is that as more atoms are added to the trap, the trap size grows in such a way as to keep the trap density approximately constant.[58] That is, if the density of atoms in the trap goes up, then so does the magnitude of the radiation pressure force, and hence the trap swells to a larger size to keep the sum of the three forces (i) - (iii) approximately zero across the trap. Conventional radiation pressure thus leads to a limitation on the density achievable in an optical trap[3].[58, 56]

Given that radiation pressure seems to be the villain in this story, one might ask whether in fact there must fundamentally be a repulsive force associated with the scattered photons in an optical dense medium. In support of a view of the contrary, our previous work suggests that in fact over some regions in frequency, the absorption spectrum for an atom in the trap can be such as to give rise to gain for scattered photons in the trap and hence to recoil toward the emitting atom (that is, to a resulting attractive force). For example, if the atoms 1 and 2 in Fig. 5.6(b) were in our trap and atom 1 emitted a photon at the frequency of narrow gain in Fig. 4.2, then atom 2 would amplify this radiation and emit another photon with the same momentum. Thus the recoil of atom 2 toward atom 1 would give rise to an attractive force, i.e., the radiation pressure becomes negative. Of course the difficulty is that the regions of gain evidenced in Fig. 4.2 are over limited ranges in frequency and are presumably overwhelmed by the regions of large absorption. Note

[3]One way to overcome this limit is the "dark SPOT" trap demonstrated in Ref. [59] and mentioned by the end of Section 2.1

that whereas we have previously viewed spectra as in Fig. 4.2 as the response to an external field, we now shift perspective and identify such spectra as the response to the internal scattered fields of the trap. Since these internal fluorescent fields are not monochromatic (as was the probe field in Fig. 4.2), we must necessarily integrate the atomic response function against the spectrum of incoming frequencies. In this case, the response function is the frequency resolved absorption cross section $\sigma_A(\omega)$ for a weak probe of frequency ω in the presence of the strong trapping fields, while the distribution of incident frequencies ω is specified by the fluorescent spectrum $S^{\text{total}}(\omega) = S^{\text{incoh}}(\omega) + S^{\text{coh}}(\omega)$, which includes both elastic and inelastic scattering. The total atomic cross section σ_R for scattered radiation in the trap is thus

$$\sigma_R = \frac{\int_0^\infty S^{\text{total}}(\omega)\,\sigma_A(\omega)\,d\omega}{\int_0^\infty S^{\text{total}}(\omega)\,d\omega} \tag{5.68}$$

$$\overset{\text{for transition } 1\leftrightarrow 2}{=} \frac{|\rho_{12}|^2\,\sigma_{A_2}(\Omega_2)}{\rho_{11}} + \frac{\int_0^\infty S^{\text{incoh}}(\omega)\,\sigma_{A_2}(\omega)\,d\omega}{\pi\rho_{11}}, \tag{5.69}$$

where the second equation follows from Eq. (5.66)[4]. One can also define a "normalized" version for σ_R:

$$\tilde{\sigma}_R = \sigma_R/\sigma_0. \tag{5.70}$$

From Eq. (5.69) we see that a negative $\sigma_A(\omega)$ (which is proportional to the absorption spectra) would guarantee a negative σ_R. Although in a two-level system, (like in Fig. 4.2), the absorption spectra is negative (gain-like) only in a small range of frequency space, in a three-level system the spectra can exhibit gain over the entire frequency range.[86] For example, we have plotted in Fig. 5.7 the absorption and emission spectra for a V system. Note that in Fig. 5.7, the transition $1 \leftrightarrow 2$ is clearly inverted and the spectra show gain for all frequencies. Although in Fig. 5.7(b), transition $1 \leftrightarrow 3$ is absorptive over some frequency range, detailed quantitative calculation shows that the integrated absorption cross section σ_R is negative for $1 \leftrightarrow 3$ ($\tilde{\sigma}_{R_1} = -4.2 \times 10^{-4}$). Of course, even if the integral does not produce a negative

[4]Ref. [58] used the scattering cross section for the driving field σ_{L_2} in place of $\sigma_{A_2}(\Omega_2)$ in the first term of Eq. (5.69).

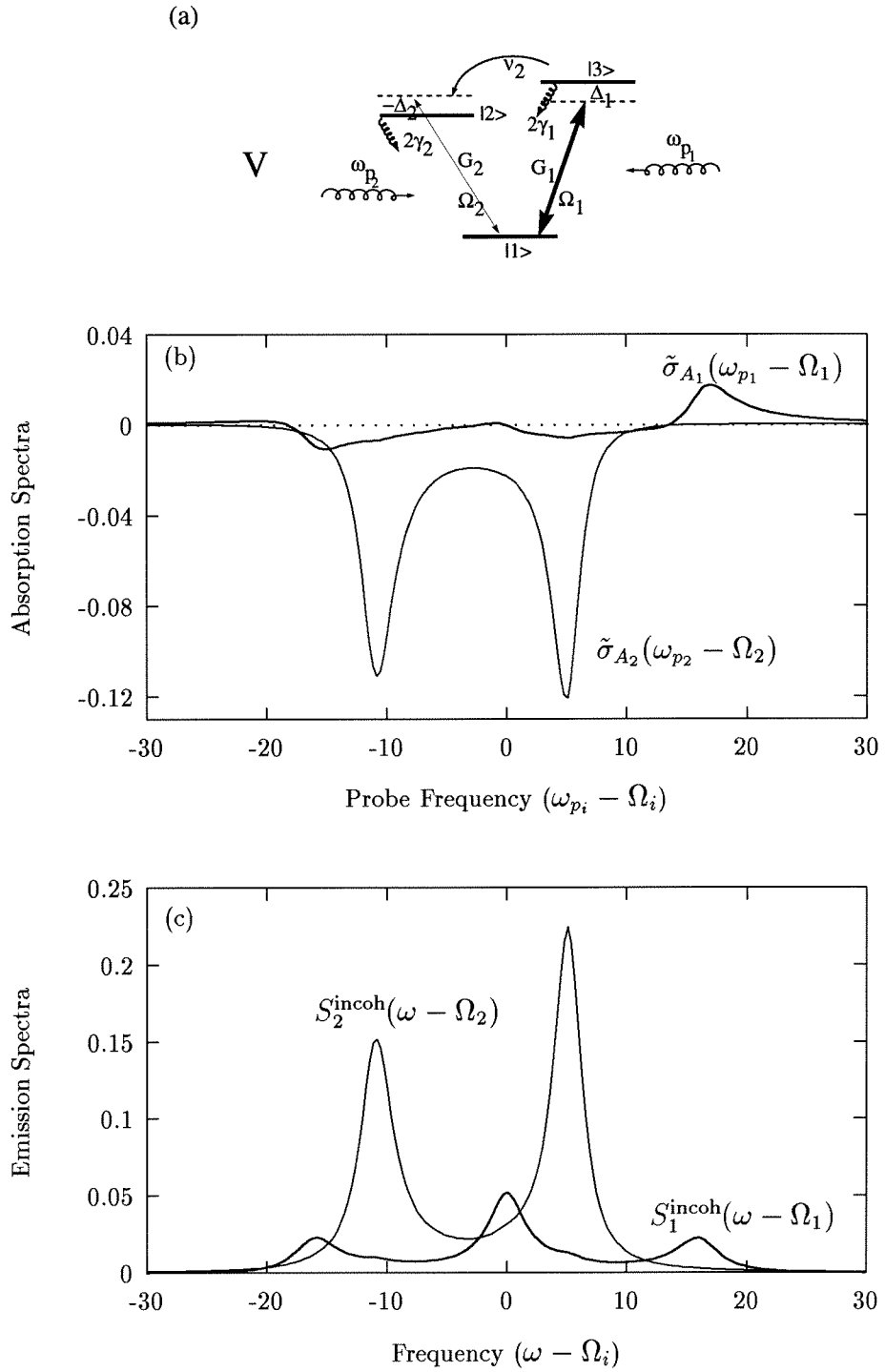

Figure 5.7: Absorption [(b)] and (incoherent part of the) emission [(c)] spectra for a V system with parameters $G_1 = 8$, $G_2 = 1$, $\Delta_1 = 2$, $\Delta_2 = -2$, $\gamma_1 = \gamma_2 = 0.5$, $\nu_1 = 0$ and $\nu_2 = 3$. The negative values for absorption spectra in (b) correspond to gain. The integration of the absorption spectra [Eq. (5.68)] yields $\tilde{\sigma}_{R_1} = -4.2 \times 10^{-4}$ and $\tilde{\sigma}_{R_2} = -3.1 \times 10^{-2}$.

value, the fluorescence from transition $1 \leftrightarrow 2$ would dominate that of transition $1 \leftrightarrow 3$ both as regards to the rate of spontaneous emission (population of 2 greater than population 3 and $\nu_2 > 2\gamma_1$) and as regards to the magnitude of the absorption cross section ($|\tilde{\sigma}_{A_2}| \gg |\tilde{\sigma}_{A_1}|$). Hence the accompanying negative radiation pressure ($\tilde{\sigma}_{R_2} = -3.1 \times 10^{-2}$) in a dense sample should lead to an attractive force which might be employed for optical implosion.[87] Also note that the MOT associated with the levels in Fig. 5.7(a) could operate predominantly by stimulated absorption on the $1 \leftrightarrow 3$ transition and stimulated emission on the $2 \leftrightarrow 1$ transition, with a reduced role for spontaneous emission on these transitions and consequently with the potential for reduced temperature.

Such encouraging characteristics not withstanding, the V system identified here is hard to realize in the experiment because the selection rule of the dipole transition would prevent the simultaneous dipole coupling between the ground state and the two excited states while maintaining an appreciable transfer rate ν_2 between the excited states at the same time. But unfortunately, in the V system shown in Fig. 5.7(a), the population inversion between $1 \leftrightarrow 2$ comes principally from such an artificial rate. (Note, however, that population inversion is not a necessary condition for a negative σ_R since we will prove later that σ_R can be less than zero even for a two-level atom for appropriate detunings and Rabi frequencies [Fig. 5.11(b)].) Fortunately, the two-photon transition between levels $6S_{1/2}$ and $6D_{5/2}$ in Cs atom offers an opportunity to overcome the dipole selection rule. The population transfer rate ν_2 between the excited states then comes from the dipole transition between $6D_{5/2}$ and $6P_{3/2}$, which has a wavelength of 917.5 nm. The generalization of our theory to incorporate two-photon transition is currently underway.[101]

The $6S_{1/2} \leftrightarrow 6P_{3/2} \leftrightarrow 6D_{5/2}$ transition scheme should not be unfamiliar to us because we have already encountered this system in Chapter 1 when we introduced the single-atom laser. There it was configured as a Λ system with $6D_{5/2}$ being the common level. To illustrate the versatility of this system, we will see it again in the next subsection as a Ξ system. For now, let us conclude this subsection by pointing out that the negative absorption spectra in Fig. 5.7 are also present in the Ξ system,

(at least between one set of energy levels,) as shown in Fig. 5.8(b). Although the transition $1 \leftrightarrow 2$ is absorptive, with its integrated cross section for rescattered light $\tilde{\sigma}_{R_2} = +2.26 \times 10^{-2}$, as we will explain in the next subsection, the ratio σ_R/σ_L between the integrated cross section σ_R and the linear absorption cross section for the driving field σ_L is a more relevant quantity in measuring the mechanical force. Such a ratio is larger in amplitude for the $1 \leftrightarrow 3$ transition ($\sigma_{R_1}/\sigma_{L_1} = -2.22$, with $\tilde{\sigma}_{R_1} = -1.25 \times 10^{-2}$) than in $1 \leftrightarrow 2$ transition ($\sigma_{R_2}/\sigma_{L_2} = +1.47$).

5.9.4 Radiation Pressure and Attenuation Force in Two- and Three-Level Systems

The Ξ system introduced by the end of the previous subsection is one step closer to experimental reality, but the driving fields there were exactly on resonance with the atomic transition ($\Delta_1 = \Delta_2 = 0$). To provide the viscous damping force and the spatial restoring force for cooling and trapping, one needs to tune the laser away from the atomic resonance to produce an imbalance in atomic absorption. A more realistic configuration is shown in Fig. 5.9(a), where a Ξ system with $\Delta_1 = 0$, $\Delta_2 = -2$, and $\gamma_2 = 2\gamma_1 = 1$ is sketched. Such a system can be realized in Cs atom, with transition $2 \leftrightarrow 1$ being the D_2 transition $6S_{1/2} \leftrightarrow 6P_{3/2}$ and level 3 being $6D_{5/2}$, having spontaneous emission rate (into $6P_{3/2}$ of wavelength 917.5 nm, cf. Fig. 2.7) 15.2×10^6 sec^{-1}, roughly half that of $6P_{3/2} \leftrightarrow 6S_{1/2}$. Although we have set $\nu_1 = 0$, a nonzero population transfer from ground state to the excited state $6D_{5/2}$ can be realized via two-photon transition (wavelength 883.7 nm)[36] to enhance population inversion. This level scheme is a reasonably faithful realization of the model shown in Fig. 5.9(a) with one caveat being that it is possible for the $6D$ state to decay to the $7P$ state, although this transition has a branching ratio of only 4×10^{-3} due to the small energy spacing (the wavelength for the $6D_{5/2} \rightarrow 7P_{3/2}$ transition is about 15 μm.) However, at the high densities that we envisage, superfluorescent processes may well become important.[102] We will show that although the integrated absorption cross section σ_R becomes negative only for one set of transition, the interplay of radiation

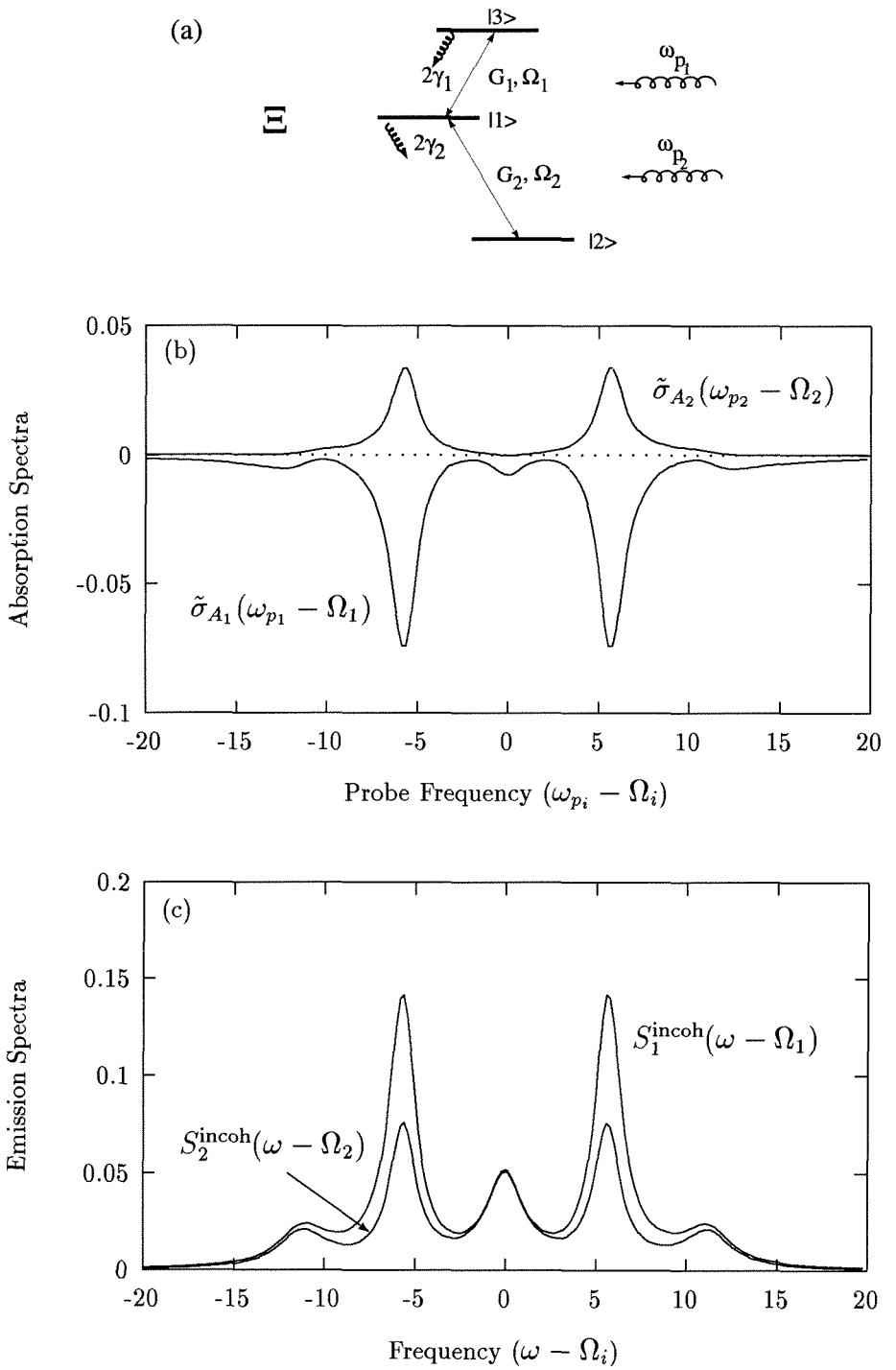

Figure 5.8: Absorption [(b)] and (incoherent part of the) emission [(c)] spectra for a Ξ system with parameters $G_1 = 4$, $G_2 = 4$, $\Delta_1 = \Delta_2 = 0$, $\gamma_1 = 0.5$, $\gamma_2 = 1$ and $\nu_1 = \nu_2 = 0$. The negative values for absorption spectra in (b) correspond to gain. The integration of the absorption spectra [Eq. (5.68)] yields $\tilde{\sigma}_{R_1} = -1.25 \times 10^{-2}$, $\tilde{\sigma}_{R_2} = +2.26 \times 10^{-2}$ and $\sigma_{R_1}/\sigma_{L_1} = -2.22$, $\sigma_{R_2}/\sigma_{L_2} = +1.47$.

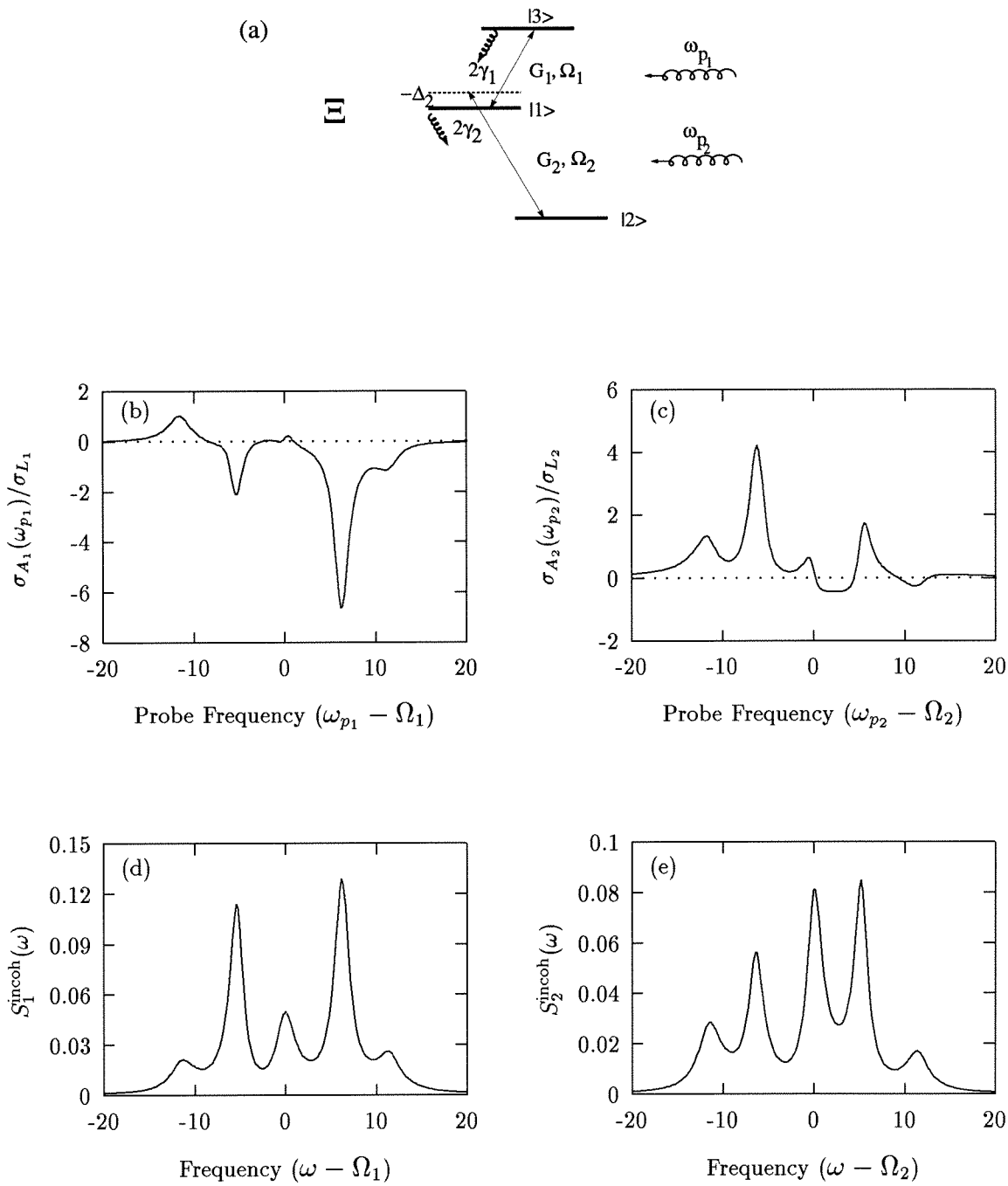

Figure 5.9: Absorption (b,c) and (incoherent part part of the) emission spectra (d,e) for a Ξ system with parameters $G_1 = 4$, $G_2 = 4$, $\Delta_1 = 0$, $\Delta_2 = -2$, $\gamma_1 = 0.5$, $\gamma_2 = 1$ and $\nu_1 = \nu_2 = 0$. Negative values of absorption spectra in (b) and (c) correspond to gain. Note that the absorption spectra are normalized to σ_L instead of σ_0. The integration of the absorption spectra [Eq. (5.68)] gives $\sigma_{R_1}/\sigma_{L_1} = -1.6$ and $\sigma_{R_2}/\sigma_{L_2} = 0.77$.

pressure and attenuation still provides a net compressive force for both transitions, while maintaining favorite conditions for trapping.

To be more quantitative let us first analyze in detail the forces acting on a dense sample under intense radiation. In the previous subsection we have already seen that this can be divided into three parts, the trapping force, the attenuation force, and the radiation pressure force. This simple and naïve division is justified by the result of a more detailed and rigorous investigation based on the Fokker-Planck equation of an N-atom system including their center-of-mass motion.[100] Besides the trapping force, which we described in Section 2.1, there are two more forces resulting from the interaction between the atoms, the first of which being the radiation pressure force we introduced earlier. Refer to the settings in Fig. 5.6(a), we assume that atom 1 is under illumination of laser beam with intensity I, and the scattering cross section for this field is σ_L. Note that σ_L is different than the frequency-resolved cross section for a weak probe beam $\sigma_A(\omega_p)$ that we previously introduced. The cross section σ_L here only involves the steady-state solution of the density matrix and has the simple form

$$\sigma_L = \sigma_0 \,\mathrm{Im}\left(\frac{\gamma_\perp \rho_{\mathrm{eg}}}{G}\right) \tag{5.71a}$$

$$= \frac{G}{\gamma_\perp} \frac{1}{1 + 2G^2/\gamma_\perp^2 + \Delta^2/\gamma_\perp^2}, \tag{5.71b}$$

for a two-level system. For a three-level system, Eq. (5.71a) still holds, but ρ_{eg} is replaced by the appropriate density matrix elements for three-level systems. The scattered light by atom 1 has intensity $I_{\mathrm{rad}} = \sigma_L I/4\pi d^2$ at the position of atom 2 a distance d away. The radiation pressure force then has the form $F_R = I_{\mathrm{rad}}\sigma_R/c$. If we extend this argument for two atoms to an arbitrary distribution of atoms in three dimension, in analogy to Gauss's law of electrostatics (assuming an incident photon is unlikely to scatter more than twice), then the radiation pressure force can be written as:[58]

$$\nabla \cdot \mathbf{F}_R = \frac{\sigma_R \sigma_L I n(\mathbf{r})}{c}, \tag{5.72}$$

where n is the number density of the trap.

Another force present in a collection of atoms is the attenuation force[87] caused by atomic absorption of the laser photons. This is easiest derived in one-dimension where the intensity of the laser is attenuated by an amount $e^{-n\sigma_L l}$ after propagation of a distance l. If the atom is illuminated by two counter propagating beams with intensity I outside the sample, then inside the sample the intensity of the beams are not balanced because they propagate through different lengths of the sample. For example, at a distance x from the center of the sample having radius R, the beam propagating from left to right is attenuated by $e^{-n\sigma_L(R+x)}$ and the beam from right to left by $e^{-n\sigma_L(R-x)}$ [Fig. 5.6(c)]. Then the attenuation force which is proportional to the intensity imbalance has the form[87]

$$\nabla \cdot \mathbf{F}_A = -\sigma_L^2 In/c, \tag{5.73}$$

for $n\sigma_L R \ll 1$.

From Eqs. (5.72) and (5.73) we see that the attenuation force is always compressive (restoring force) while the radiation pressure force could be attractive or repulsive depending on the sign of the cross section for scattered light σ_R. In an atomic sample these two forces act together, (in addition to the Zeeman-shift restoring force), it is the sum of these two forces which governs the combined effect of the collective behavior:

$$\nabla \cdot (\mathbf{F}_R + \mathbf{F}_A) = -\sigma_L^2 \left(1 - \frac{\sigma_R}{\sigma_L}\right) \frac{In}{c}. \tag{5.74}$$

The key point here is then the term $\sigma_L^2(1 - \sigma_R/\sigma_L)$. In particular, if $\sigma_R/\sigma_L > 1$, then the combination of radiation pressure and optical attenuation is repulsive and acts to counterbalance the basic Zeeman-shift trapping force. In this case, the trap size grows as more atoms are added in such a way as to keep the density approximately constant.[58] On the other hand, if $\sigma_R/\sigma_L < 1$, then the combination of radiation pressure and optical attenuation gives rises to a force that tends to compress the trap and acts in concert with the Zeeman-shift force. Possible equilibrium trap configurations have not been calculated for this case. However, note that this

circumstance harbors the potential for instability (and "optical implosion") since as the trap size diminishes, the density goes up and the compressive force ($\mathbf{F}_R + \mathbf{F}_A$) rises, which acts to increase the density still further, and so on. In Ref. [87] Dalibard presented an analysis based upon a Fokker-Planck equation for such a scenario, albeit in the absence of the contributions of $\mathbf{F}_R$ and the Zeeman-shift trapping force. Even in the absence of such a runaway solution, the trap size should diminish dramatically for $\sigma_R/\sigma_L < 1$, since positive radiation pressure causes the diameter of our MOT to be more than 10-fold larger than expected based upon the Zeeman-shift (spring-constant) trapping potential and the measured temperature.

The essential question then becomes whether or not it is possible to have $\sigma_R/\sigma_L < 1$ while at the same time maintaining conditions suitable for trapping. To answer this question we come back to the three-level Ξ system illustrated in Fig. 5.9(a). We assume that the two transitions are driven by independent fields of Rabi frequencies (G_1, G_2) and with detunings (Δ_1, Δ_2). For each of the transitions $1 \leftrightarrow 2$ and $1 \leftrightarrow 3$, we have calculated the probe cross section $\sigma_A(\omega_p)$ and fluorescent spectrum $S^{\text{total}}(\omega)$, with examples from this theoretical work displayed in Fig. 5.9(b)-(e). Figs. 5.9(b) and (d) is a result for $(\sigma_{A_1}(\omega_{p_1})/\sigma_{L_1},\ S_1^{\text{incoh}}(\omega))$ for the $1 \leftrightarrow 3$ upper transition. Note that unlike in previous cases we have normalized $\sigma_A(\omega_p)$ to σ_L instead of σ_0, since the quantity of interest here is the ratio σ_R/σ_L. Also note that $\sigma_{A_1} < 0$ over large intervals in Fig. 5.9(b). The integration of $\sigma_{A_1}(\omega)/\sigma_{L_1}$ against $S_1^{\text{incoh}}(\omega)$ in Fig. 5.9(d) (including the elastic component) yields $\sigma_{R_1}/\sigma_{L_1} = -1.6$. On the other hand, Figs. 5.9(c) and (e) give corresponding results for $(\sigma_{A_2}(\omega_{p_2})/\sigma_{L_2},\ S_2^{\text{incoh}}(\omega))$ for the $1 \leftrightarrow 2$ lower transition. Although in Fig. 5.9(c) $\sigma_{A_2} > 0$ over most of the frequency range, nonetheless we find that the integration of the probe spectrum $\sigma_{A_2}(\omega_{p_2})/\sigma_{L_2}$ against the emission spectrum for this transition $S_2^{\text{total}}(\omega)$ whose incoherent part is displayed in Fig. 5.9(e) yields the result $\sigma_{R_2}/\sigma_{L_2} = 0.77 < 1$. Thus for the conditions represented in Fig. 5.9, the stage is set for "negative" radiation pressure associated with the $1 \leftrightarrow 3$ transition ($\sigma_{R_1} < 0$) to assert its influence and to compress the sample, while at the same time $\sigma_{R_2}/\sigma_{L_2} < 1$ so that the lower transition has a net compression in the interplay of radiation pressure and attenuation.

Although our attention has centered on the quantities (σ_A/σ_L, S^{total}), one must of course also consider the steady-state trapping forces associated with the distribution of atomic population. To indicate that the scenario presented in Fig. 5.9 is consistent with the basic notion of a MOT for the three-level Ξ system at least a pedestrian level, we present in Fig. 5.10 the results of our calculation for the variation of the atomic absorption $\tilde{\alpha}_i$ versus detuning Δ_i. Here $\tilde{\alpha}_i$ is proportional to the absorptive component of the atomic polarization ($\tilde{\rho}_{31}$ and $\tilde{\rho}_{12}$) and is normalized so as to represent a cross section (in units of $\sigma_0 = (3/2\pi)\lambda_i^2$). For Fig. 5.10, the detunings are varied with $\Delta_1 + \Delta_2 = -2$ with the operating point corresponding to Fig. 5.9 indicated by an arrow in each case (i.e., $\Delta_2 = -2$, $\Delta_1 = 0$). For a single pair of counter-propagating beams (e.g., $1 \leftrightarrow 2$ beam with $\mathbf{k}_2$ along $-x$ and $3 \leftrightarrow 1$ beam with $\mathbf{k}_1$ along $+x$) an atom of velocity v experiences a radiation pressure force from each beam that tends to damp its motion, precisely as in optical molasses. Similar comments apply to the Zeeman-shift trapping force. So it seems possible to find in the multidimensional space of laser detunings and intensities suitably robust regions in which the various trapping forces are globally compatible. As pointed out in Ref. [14] (and earlier in Section 5.9.3 associated with the discussion of Fig. 5.7), one could identify level schemes and excitation conditions so that a MOT operates predominantly in a cyclic fashion with stimulated absorption on one transition and stimulated emission on another, with the requisite decay (or "arrow of time") provided by a mechanism of low momentum transfer as compared to $\hbar\mathbf{k}$ for the trapping lasers.

As might be guessed, the factor $(\sigma_R/\sigma_L - 1)$ could become negative even for a two-level atom. Moreover, a glance at Fig. 5.11(b), which plots σ_R/σ_L versus Rabi frequency G for a two-level atom having different detunings Δ, shows that σ_R/σ_L itself can become negative (for $\Delta \lesssim 0.5$) for sufficiently large intensity ($G \gtrsim 1$). Although this surprising result is indeed counter-intuitive and lacks physical interpretation at the present time (except for the *ad hoc* explanation that at low detuning and large intensity, the emission spectrum has a distribution such that it favors the negative part of the absorption spectrum), it violates no physical law that we have investigated. It is more surprising then, that the effects we are predicting have not been previously

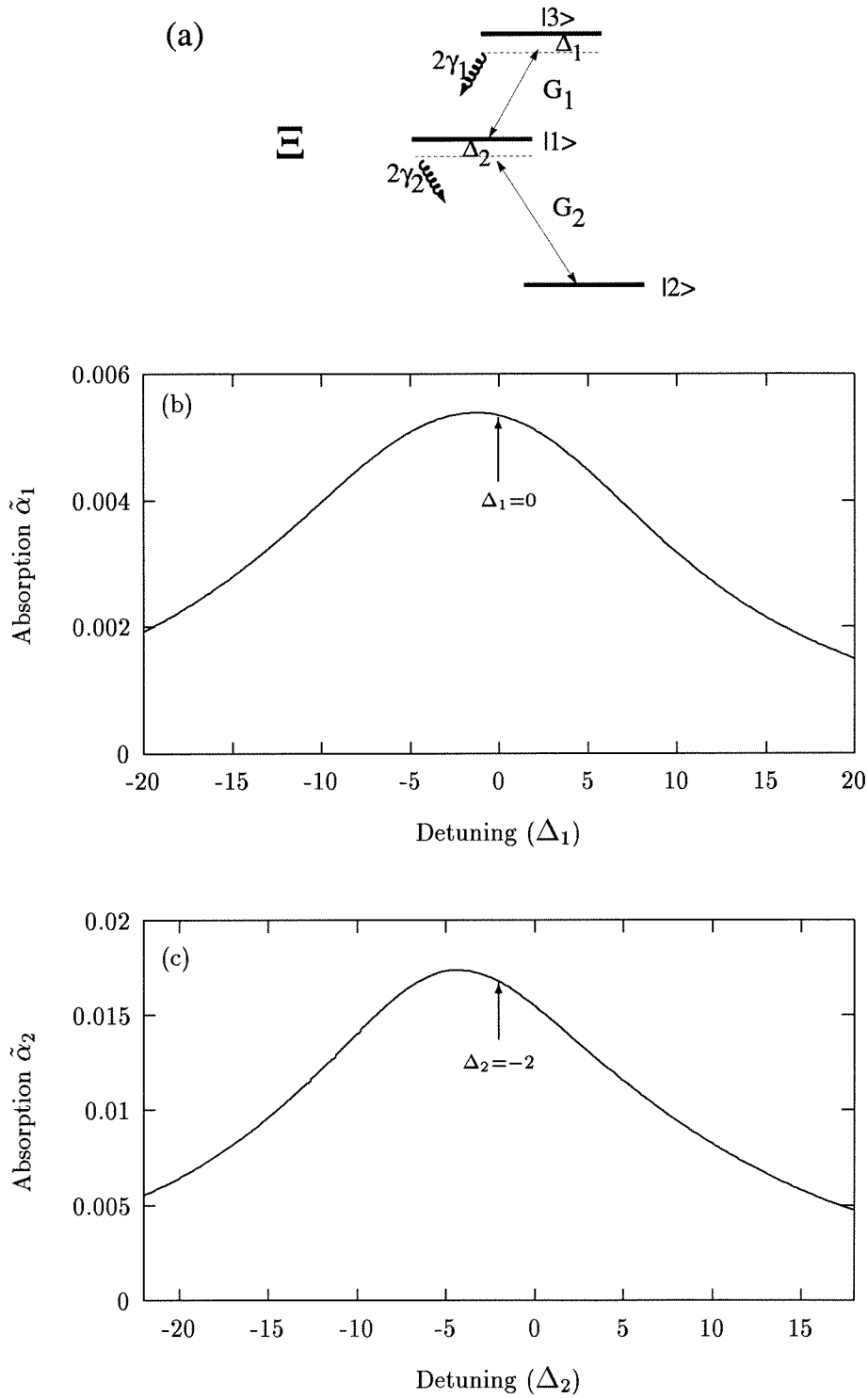

Figure 5.10: Absorption $\tilde{\alpha}_1$ for the upper $3 \leftrightarrow 1$ (b) and $\tilde{\alpha}_2$ for the lower $1 \leftrightarrow 2$ (c) transitions of the Ξ system displayed in (a). The detunings are varied with $\Delta_1 + \Delta_2 = -2$; the arrows mark the detunings for which Fig. 5.9 is plotted. Other parameters are as in Fig. 5.9, i.e., $G_1 = 4$, $G_2 = 4$, $\gamma_1 = 0.5$, $\gamma_2 = 1$, and $\nu_1 = \nu_2 = 0$.

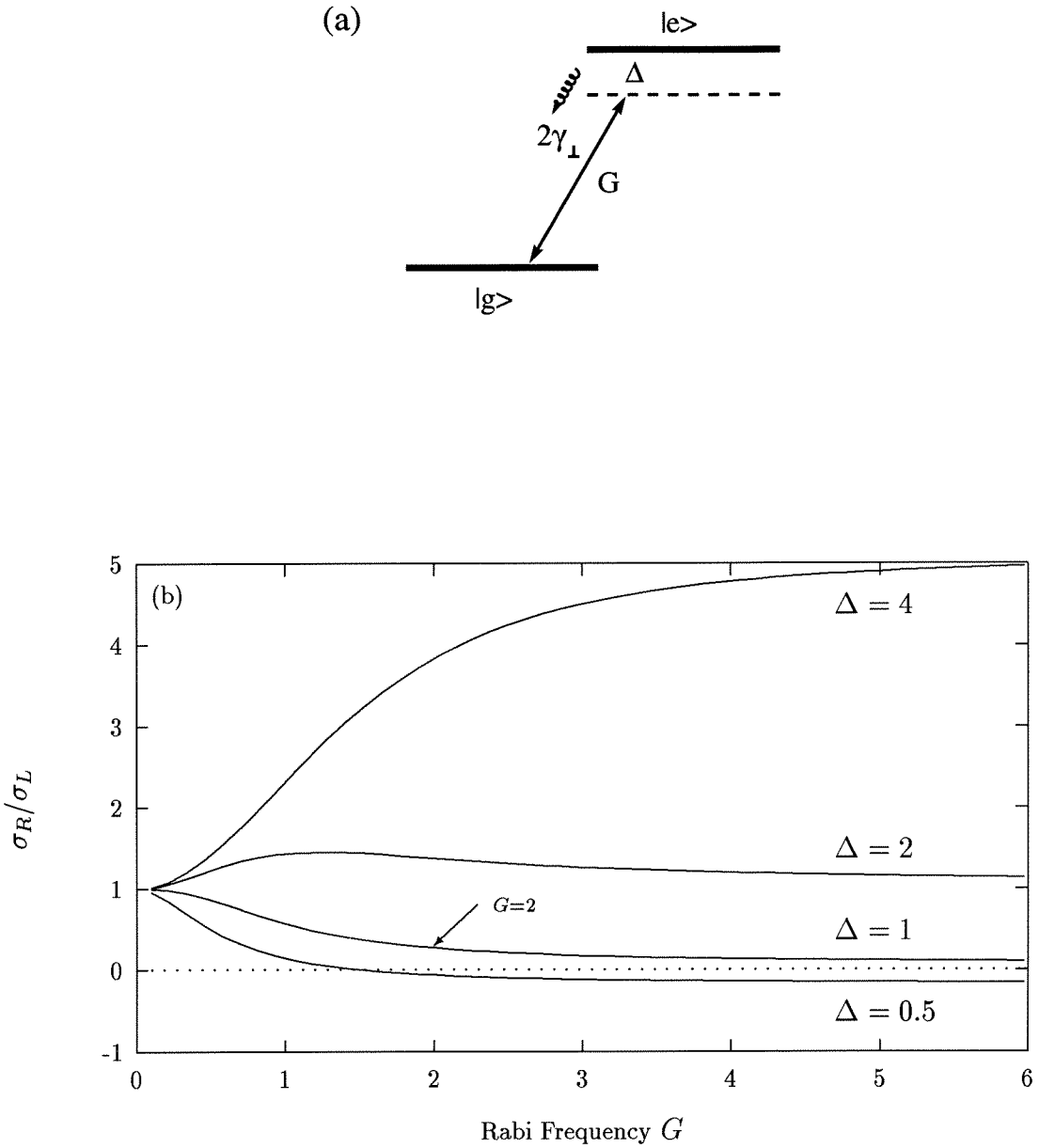

Figure 5.11: The integrated absorption cross section for scattered light σ_R/σ_L versus Rabi frequency G for a two-level system with different detunings Δ. The spontaneous emission rate is set to be $2\gamma_\perp = 1$. $\sigma_R/\sigma_L < 0$ corresponds to negative radiation pressure, while $0 < \sigma_R/\sigma_L < 1$ corresponds to a compressive force for the combination of the attenuation force and the (positive) radiation pressure force. For details see text.

observed. Two comments are relevant in this regard. The first is that our results for σ_R/σ_L must be averaged over an appropriate distribution of fields within the trap. For example, for $2\gamma_\perp = 1$, $\Delta = 1$ and $G = 2$ (corresponding to the point marked by the arrow in Fig. 5.11(b), the same (over simplified) averaging as in Ref. [58] yields $\bar{\sigma}_R/\bar{\sigma}_L = 0.49$ whereas this value is 0.27 for the unaveraged case. Note that for the work in Ref. [58], $\bar{\sigma}_R/\bar{\sigma}_L \approx 1.3$, which is a ratio that led to dramatic changes of trap morphology. Similarly the results in Ref. [56] for much larger trapping beams and intensities lead to substantial increases in the number of trapped atoms without corresponding increases in the density of the trapped sample. Hence it seems clear that radiation pressure and optical attenuation do play important roles in previous work (including our own) as specified by $\sigma_R/\sigma_L > 1$. The second comment concerning the prediction $\sigma_R/\sigma_L > 1$ for MOT is that we and others typically operate the trap with much larger detunings than the naïve expectation $\Delta = 1$ (one half linewidth of red detuning). Indeed, for small red detunings ($\Delta \simeq 1 - 2$) we observe that the steady-state trap fluorescence drops precipitously, presumably due to a radical decrease in filling efficiency.[58, 56] We speculate that the consequence of this reduced trapping efficiency for small detuning is that the strongly density dependent effects associated with radiation pressure and optical attenuation become inoperative due to the low *steady-state* density. To circumvent this difficulty of small steady-state density for small Δ, we have monitored the transient response of a trap which is first filled with large detuning ($\Delta = 3.2$ corresponding to 8 MHz red detuning in Cs) and then stepped to a small detuning ($\Delta = 1.2$ or 3 MHz for Cs). The choice of these particular detunings is based on Fig. 5.12(a), which indicates that the combined effect of the attenuation force and radiation pressure force should change from repulsive ($\Delta = 8$ MHz, $\nabla \cdot (\mathbf{F}_A + \mathbf{F}_R) > 0.$) to attractive ($\Delta = 3$ MHz, $\nabla \cdot (\mathbf{F}_A + \mathbf{F}_R) < 0$). Fig. 5.12(b) is the fluorescence distribution along a horizontal line across the trap, measured by a CCD camera before and immediately after (less than the trap's escape time) switching. From Fig. 5.12(b) we see that the peak height of the trap's fluorescence increased to 1.7 times of that before switching while the width of the distribution is reduced to 60%, consistent with the prediction [from Fig. 5.12(a)] that

(a)

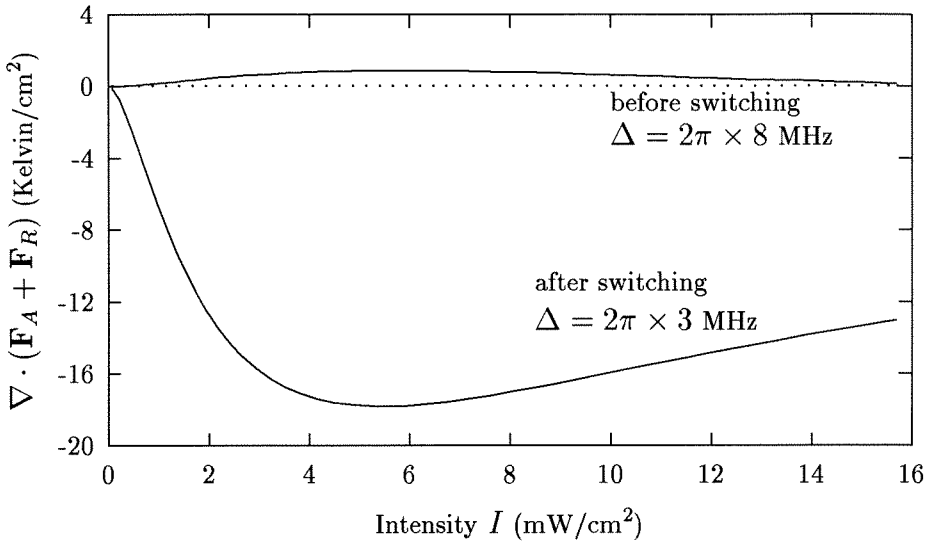

(b)

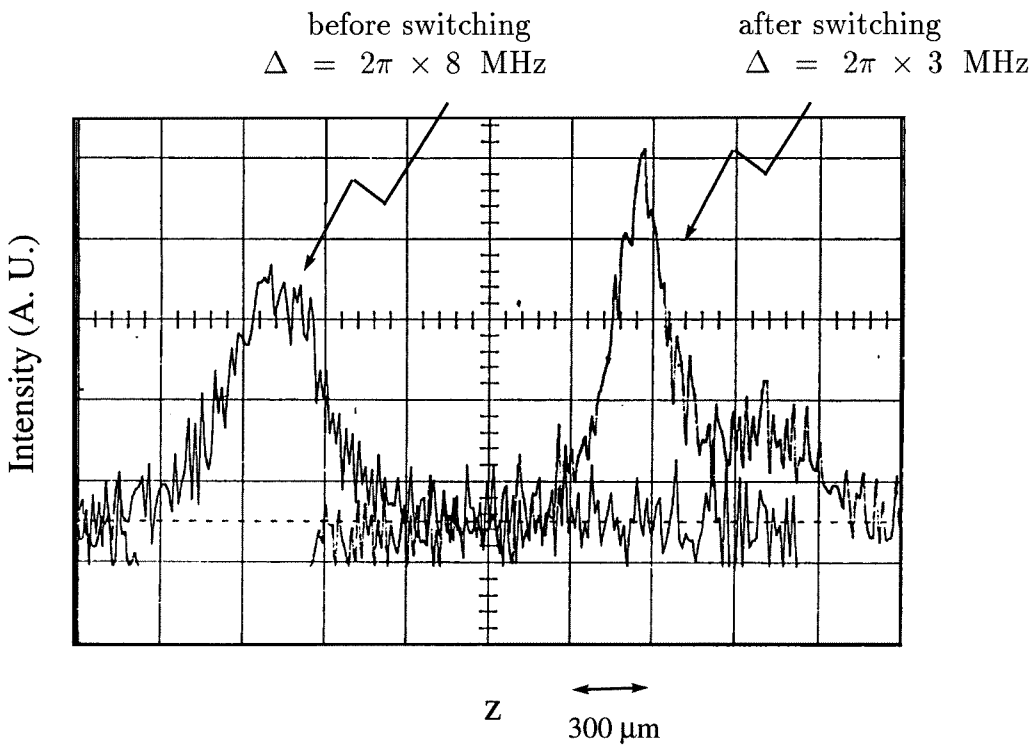

Figure 5.12: The fluorescence profile for a trap before and after switching of the detuning. (a) The calculated divergence of the sum of the radiation pressure force and the attenuation force. A negative value indicates compressive force. (b) The fluorescence profile along the z direction (perpendicular to the line of sight). The trace is obtained by expanding the output of a CCD camera on a digital oscilloscope.

such a switch in detuning should compress the trap. Note that for the total trapping intensity ($I = 16$ mW/cm^2) we are operating at, the spring constant of the trapping potential is actually slightly decreased after the switching of the detuning. So in the absence of a compressive agent, the size of the trap should increase rather than decrease. Although in our initial result no optical implosion like that predicted in Ref. [87] is observed, it is at least worthwhile to make further investigations proceeding along this line.

Chapter 6 Summary

In this thesis we have investigated some general properties of optical processes in a sample consisting of laser cooled and trapped atoms. In the first part (Chapter 3), we have presented a simple model for the number of atoms contained in a magneto-optical trap and described an experiment based on such a model to trap a single atom. In the experiment we have recorded the photon flux of the fluorescent light emitted by such a trap containing only small number of atoms. In these traces we have found discrete steps suggesting trapping of a single atom and have compared the duration and size of the jumps to values predicted by simple models. While there is a quantitative disagreement between theory and experiment as to the absolute magnitude of the individual jumps, other evidence from the experiment strongly supports the conclusion that we have observed the trapping of individual neutral atoms. Straightforward improvements in the optical system (for enhanced signal-to-noise ratio) and in background pressure (for increased trap lifetime) should lead to a relatively stable sample consisting of a single trapped neutral atom for a variety of future applications.

While the first part of this thesis focuses on the isolation of a single atom, in the second part the collective behavior of the atoms in the trap plays an important role. We began by the description of a non-linear spectroscopy experiment of trapped atoms (Chapter 4), in which narrow resonances in the probe absorption spectra have been found, in contradiction with the standard two-level theory and its various extensions and modifications. To explain this contradiction, and also in hope to discover new avenues leading to improved trapping schemes, in Chapter 5 we have derived the formulae and performed numerical calculations for absorption and emission spectra of three-level Λ, Ξ and V systems by using quantum regression theorem in Laplace space. In particular, absorption spectra of a three-level Λ system, which show narrow gains and absorptions at the frequency of the driving field having width comparable to

ground state splitting, agrees qualitatively with the experimental spectra measured for our trap. In addition, a three-level system also shows new interesting features which is rare or not present in a two-level system. One such feature concerns the cross section for scattered radiation, whose sign could be inverted if the absorption spectra exhibit gain over a significant range of frequency space. Such a reversal of sign dramatically changes the effect of radiation pressure, which is usually positive and repulsive for a two-level atom. Detailed investigation including the attenuation force shows that the combined effect of radiation pressure force and attenuation force could be compressive even for a two-level system. Initial results in the experiment confirms this prediction and further study is worthwhile.

As stated at the outset, this work represents some initial effort to reach our goal of investigating non-classical effects in single-atom systems. If, because of the work presented in this thesis, we are one step closer to this goal, then this work is well worth the effort.

Appendix A Fortran Code for Calculating Λ Spectra (Ag.f)

```
      complex LRdc(8,8),LC(8,8),Ldc(8,8),Li(8,8),M(8,8)
      complex Mi(8,8),N(8,8)
      complex IRdc(8),IC(8),Idc(8),Fdc(8),NI(8)
      complex i,G2
      complex S1,S2,A1,A2
      real gm1,gm2,G1,v1,v2,dp,dp1,dp2,dph
      character*2 fn
      character*25 f1,f2,f3,f4,f5
      i=(0,1)

      open(4,file="Ag.data/AgNumber")
      read(4,*)n1
      n1=n1+1
      rewind 4
      write(4,*)n1
      close(4)

      encode(2,11,fn) n1
11    format(I2)
      f1="Ag.data/S1."//fn
      f2="Ag.data/S2."//fn
      f3="Ag.data/Par."//fn
      f4="Ag.data/A1."//fn
      f5="Ag.data/A2."//fn
```

```
open(4,file=f4)
open(5,file=f5)
open(2,file=f1)
open(3,file=f2)

open(1,file="A.in")
read(1,*)gm2,gm1,d2,d1,G2,G1,v2,v1,dp1,dp2,dph
close(1)

open(7,file=f3)
write(7,*)"gm2=", gm2,"    gm1=", gm1
write(7,*)"d2=",d2, "    d1=",d1
write(7,*)"G2=",G2, "    G1=", G1
write(7,*)"v2=",v2,"    v1=", v1
write(7,*)"dp1=",dp1,"    dp2=",dp2,"    dph=",dph
close(7)


LRdc(1,1)=-2*gm1-2*gm2
LRdc(1,2)=i*conjg(G2)
LRdc(1,3)=i*G1
LRdc(1,4)=-i*G2
LRdc(1,7)=-i*G1
LRdc(2,1)=i*G2
LRdc(2,2)=-gm1-gm2-i*d2
LRdc(2,5)=-i*G2
LRdc(2,8)=-i*G1
LRdc(3,1)=2*i*G1
LRdc(3,3)=-gm1-gm2-i*d1
LRdc(3,5)=i*G1
```

```
LRdc(3,6)=-i*G2
LRdc(4,1)=-i*conjg(G2)
LRdc(4,4)=-gm1-gm2+i*d2
LRdc(4,5)=i*conjg(G2)
LRdc(4,6)=i*G1
LRdc(5,1)=2*gm2
LRdc(5,2)=-i*conjg(G2)
LRdc(5,4)=i*G2
LRdc(6,3)=-i*conjg(G2)
LRdc(6,4)=i*G1
LRdc(6,6)=-i*d1+i*d2
LRdc(7,1)=-2*i*G1
LRdc(7,5)=-i*G1
LRdc(7,7)=-gm1-gm2+i*d1
LRdc(7,8)=i*conjg(G2)
LRdc(8,2)=-i*G1
LRdc(8,7)=i*G2
LRdc(8,8)=i*(-d2+d1)
LC(2,2)=-v1/2
LC(4,4)=-v1/2
LC(3,3)=-v2/2
LC(7,7)=-v2/2
LC(6,6)=-(v1+v2)/2
LC(8,8)=-(v1+v2)/2
LC(5,1)=-v2
LC(5,5)=-v1-v2
IRdc(3)=-i*G1
IRdc(7)=i*G1
IC(5)=v2
```

```
      do 10 j=1,8
      Idc(j)=(IRdc(j)+IC(j))
      do 10 k=1,8
      Ldc(j,k)=LRdc(j,k)+LC(j,k)
10    M(j,k)=Ldc(j,k)
      call inverse(Ldc,Li)
      call mul(Li,Idc,Fdc)

      do 40,dp=-dp1,dp2,dph
C      (dp=w(probe)-w(pump))
      do 20 j=1,8
20    M(j,j)=Ldc(j,j)-i*dp
      call inverse(M,Mi)
      call MatrixMul(Li,Mi,N)
      call mul(N,Idc,NI)
      S1=Mi(7,7)*Fdc(1)+Mi(7,8)*Fdc(2)+NI(7)*Fdc(3)
      S2=Mi(4,4)*Fdc(1)+Mi(4,5)*Fdc(2)+Mi(4,6)*Fdc(3)+NI(4)*Fdc(2)
      A1=Mi(7,8)*Fdc(2)-Mi(7,1)*Fdc(3)-Mi(7,4)*Fdc(6)-Mi(7,7)*
     &  (-1-2*Fdc(1)-Fdc(5))
      A2=Mi(4,4)*Fdc(1)+Mi(4,5)*Fdc(2)+Mi(4,6)*Fdc(3)-Mi(4,1)*
     &  Fdc(2)-Mi(4,4)*Fdc(5)-Mi(4,7)*Fdc(8)

C     Note:
C     M=Ldc-i*(w(probe)-w(pump))
C     Fdc="+"Inverse(Ldc)*Idc, notice Fdc is minus Phi(dc) defined
C     conventionally
      write(4,*) dp,-real(A1)*gm1
      write(5,*) dp,-real(A2)*gm2
      write(3,*) dp,real(S2)
40    write(2,*) dp,real(S1)
```

```
      close(2)
      close(3)
      close(4)
      close(5)
      write(*,*)"Data written in Ag.data/A,S*.",fn

      stop
      end

      subroutine inverse(b,ainv)
      complex a(8,8),ainv(8,8),c,b(8,8)
      do 1 j=1,8
      do 1 k=1,8
      a(j,k)=b(j,k)
1     ainv(j,k)=0
      do 5 j=1,8
5     ainv(j,j)=1
      do 40 j=1,7
      if (a(j,j).ne.0) goto 15
      do 10 k=j+1,8
      if (a(k,j).eq.0) goto 10
      do 10 l=1,8
      c=a(k,l)
      a(k,l)=a(j,l)
      a(j,l)=c
      c=ainv(k,l)
      ainv(k,l)=ainv(j,l)
      ainv(j,l)=c
10    continue
15    c=a(j,j)
```

```
      do 30 l=1,8
      ainv(j,l)=ainv(j,l)/c
30    a(j,l)=a(j,l)/c
      do 40 k=j+1,8
      c=a(k,j)
      do 40 l=1,8
      ainv(k,l)=ainv(k,l)-c*ainv(j,l)
40    a(k,l)=a(k,l)-c*a(j,l)
      do 100 l=1,8
      ainv(8,l)=ainv(8,l)/a(8,8)
100   a(8,l)=a(8,l)/a(8,8)
      do 50 j=7,1,-1
      do 50 k=j+1,8
      c=a(j,k)
      do 50 l=1,8
      ainv(j,l)=ainv(j,l)-c*ainv(k,l)
50    a(j,l)=a(j,l)-c*a(k,l)
      return
      end

      subroutine mul(a,b,c)
      complex a(8,8),b(8),c(8)
      do 10 j=1,8
      c(j)=0
      do 10 l=1,8
10    c(j)=c(j)+a(j,l)*b(l)
      return
      end

      subroutine MatrixMul(a,b,c)
```

```
      complex a(8,8),b(8,8),c(8,8)
      do 10 j=1,8
      do 10 k=1,8
      c(j,k)=0
      do 10 l=1,8
10    c(j,k)=c(j,k)+a(j,l)*b(l,k)
      return
      end
```

Bibliography

[1] See, for example, *Laser Cooling and Trapping of Atoms*, S. Chu and C. Wieman, eds. [J. Opt. Soc. Am. B **6,** 2020-2278 (1989)]; See also W. D. Phillips, J. V. Prodan, and H. J. Metcalf, J. Opt. Soc. Am. B **2,** 1751 (1985), and references therein. For a more recent review, see H. Metcalf, and P. van der Straten, Phys. Rep. **244,** 204 (1994).

[2] E. L. Raab, M. Prentiss, A. Cable, S. Chu, and D. E. Pritchard, Phys. Rev. Lett. **59,** 2631 (1987).

[3] C. Monroe, W. Swann, H. Robinson, and C. Wieman, Phys. Rev. Lett. **65,** 1571 (1990).

[4] A. M. Steane and C. J. Foot, Europhys. Lett. **14,** 231 (1991).

[5] A. Cable, M. Prentiss and N. P. Bigelow, Opt. Lett. **15,** 507 (1990).

[6] W. Neuhauser, M. Hohenstatt, P. E. Toschek, and H. Dehmelt, Phys. Rev. A **22,** 1137 (1980); D. J. Wineland and W. M. Itano, Phys. Lett. **82A,** 75 (1981); W. Nagourney, G. Janik, and H. Dehmelt, Proc. Natl. Acad. Sci. (USA) **80,** 643 (1983).

[7] W. Nagourney, J. Sandberg, H. Dehmelt, Phys. Rev. Lett. **56,** 2797 (1986); T. Sauter, W. Neuhauser, R. Blatt, P. E. Toschek, Phys. Rev. Lett. **57,** 1696 (1986); J. C. Bergquist, R. G. Hulet, W. M. Itano, and D. J. Wineland, Phys. Rev. Lett. **57,** 1699 (1986).

[8] F. Diedrich and H. Walther, Phys. Rev. Lett. **58,** 203 (1987).

[9] F. Diedrich, J. C. Bergquist, W. M. Itano, and D. J. Wineland, Phys. Rev. Lett. **62,** 403 (1989).

[10] W. E. Moerner and L. Kador, Phys. Rev. Lett. **62,** 2535 (1989); M. Orrit and J. Bernard, Phys. Rev. Lett. **65,** 2716 (1990).

[11] E. Betzig and R. J. Chichester, Science **262,** 1422 (1993).

[12] K. G. Libbrecht, private communication.

[13] Z. Hu and H. J. Kimble, Opt. Lett. **19,** 1888 (1994).

[14] J. W. R. Tabosa, G. Chen, Z. Hu, R. B. Lee, and H. J. Kimble, Phys. Rev. Lett. **66,** 3245 (1991).

[15] For an overview, see H. J. Kimble, in *Proceedings of XI International Laser Spectroscopy Conference*, L. Bloomfield, T. Gallagher, and D. Larson, eds. (American Institute of Physics, New York, 1993), p. 340.

[16] E. S. Polzik, J. Carri, and H. J. Kimble, Phys. Rev. Lett. **68,** 3020 (1992); E. S. Polzik, J. Carri, and H. J. Kimble, Appl. Phys. B **55,** 279 (1992).

[17] G. Rempe, R. J. Thompson, R. J. Brecha, W. D. Lee, and H. J. Kimble, Phys. Rev. Lett. **67,** 1727 (1991).

[18] R. J. Thompson, G. Rempe, and H. J. Kimble, Phys. Rev. Lett. **68,** 1132 (1992); M. G. Raizen, R. J. Thompson, R. J. Brecha, H. J. Kimble, and H. J. Carmichael, Phys. Rev. Lett. **63,** 240 (1989).

[19] C. W. Gardiner, Phys. Rev. Lett. **56,** 1917 (1986).

[20] R. Vyas and S. Singh, Phys. Rev. A **45,** 8095 (1992).

[21] J. D. Miller, R. A. Cline, and D. J. Heinzen, Phys. Rev. A **47,** R4567 (1993).

[22] D. Meschede, H. Walther, and G. Müller, Phys. Rev. Lett. **54,** 551 (1985).

[23] For an overview, see H. J. Kimble, in *Cavity Q.E.D., Advances in Atomic, Molecular, and Optical Physics, Supplement 2*, P. Berman ed. (Academic, New York, 1994), p. 203.

[24] Q. A. Turchette, R. J. Thompson, and H. J. Kimble, Appl. Phys. B **60** S1 (1995).

[25] F. Shimizu, K. Shimizu, and H. Takuma, Opt. Lett. **16,** 339 (1991).

[26] C. Chesman, E. G. Lima, F. A. M. de Oliveira, S. S. Vianna, and J. W. R. Tabosa, Opt. Lett. **19,** 1237 (1994).

[27] M. A. Kasevich, E. Riis, S. Chu, and R. G. Devoe, Phys. Rev. Lett. **63,** 612 (1989).

[28] T. Pellizzari and H. Ritsch, Phys. Rev. Lett. **72,** 3973 (1994).

[29] G. Grynberg, E. Giacobino and F. Biraben, Opt. Commun. **36,** 403 (1981).

[30] H. Ritsch, M. A. M. Marte, and P. Zoller, Europhys. Lett. **19** 7 (1992); H. Ritsch and M. A. M. Marte, Phys. Rev. A **47,** 2354 (1993); K. J. Schernthanner and H. Ritsch, Phys. Rev. A **49,** 4126 (1994).

[31] D. J. Heinzen and D. J. Wineland, Phys. Rev. A **42,** 2977 (1990).

[32] R. Graham, J. Mod. Opt. **34,** 873 (1987).

[33] V. B. Braginsky, Y. I. Vorontsov, and K. S. Thorne, Science **209,** 547 (1980).

[34] *Squeezed States of the Electromagnetic Field*, eds. H. J. Kimble and D. F. Walls, J. Opt. Soc. Am. B **4,** 1450-1741 (1987).

[35] H. Mabuchi and H. J. Kimble, Opt. Lett. **19,** 749 (1994).

[36] N. Ph. Georgiades, E. S. Polzik, and H. J. Kimble, Opt. Lett. **19** 1474 (1994).

[37] L. Hilico, C. Fabre, and E. Giacobino, Europhys. Lett. **18,** 685 (1992).

[38] T. W. Hänsch and A. L. Schawlow, Opt. Commun. **13,** 68 (1975).

[39] D. J. Wineland and H. Dehmelt, Bull. Am. Phys. Soc. **20,** 637 (1975).

[40] D. J. Wineland and W. M. Itano, Phys. Rev. A **20,** 1521 (1979).

[41] V. S. Letokhov and V. G. Minogin, Phys. Rep. **73,** 1 (1981).

[42] Y. Castin, H. Wallis and J. Dalibard, J. Opt. Soc. Am. B **6,** 2046 (1989).

[43] W. Neuhauser, M. Hohenstatt, P. Toschek, and H. Dehmelt, Phys. Rev. Lett. **41,** 233 (1978).

[44] D. J. Wineland, R. E. Drullinger, and F. L. Walls, Phys. Rev. Lett. **40,** 1639 (1978).

[45] S. Chu, L. Hollberg, J. E. Bjorkholm, A. Cable, and A. Ashkin, Phys. Rev. Lett. **55,** 48 (1985).

[46] A. L. Migdall, J. V. Prodan, W. D. Phillips, T. H. Bergeman, and H. J. Metcalf, Phys. Rev. Lett. **54,** 2596 (1985); V. S. Bagnato, G. P. Lafyatis, A. G. Martin, E. L. Raab, R. N. Ahmadbitar, and D. E. Pritchard, Phys. Rev. Lett. **58,** 2194 (1987).

[47] S. Chu, J. E. Bjorkholm, A. Ashkin, and A. Cable, Phys. Rev. Lett. **57,** 314 (1986).

[48] J. Dalibard and C. Cohen-Tannoudji, J. Opt. Soc. Am. B **6,** 2023 (1989).

[49] P. D. Lett, R. N. Watts, C. I. Westbrook, W. D. Phillips, P. L. Gould, and H. J. Metcalf, Phys. Rev. Lett. **61,** 169 (1988).

[50] M. Kasevich and S. Chu, Phys. Rev. Lett. **69,** 1741 (1992).

[51] J. M. Doyle, J. C. Sandberg, I. A. Yu, C. L. Cesar, D. Kleppner, and T. J. Greytak, Phys. Rev. Lett. **67,** 603 (1991).

[52] C. C. Agosta, I. F. Silvera, H. T. C. Stoof, and B. J. Verhaar, Phys. Rev. Lett. **62,** 2361 (1989).

[53] Z. Y. Zhao, I. F. Silvera, and M. Reynolds, J. Low. Temp. Phys. **89,** 703 (1992).

[54] R. J. C. Spreeuw, C. Gerz, L. S. Goldner, W. D. Phillips, S. L. Rolsten, C. I. Westbrook, M. W. Reynolds, and I. F. Silvera, Phys. Rev. Lett. **72,** 3162 (1994).

[55] E. A. Cornell, C. Monroe, and C. E. Wieman, Phys. Rev. Lett. **67,** 2439 (1991).

[56] K. E. Gibble, S. Kasapi, and S. Chu, Opt. Lett. **17,** 526 (1992).

[57] M. Prentiss, A. Cable, J. E. Bjorkholm, S. Chu, E. L. Raab, and D. E. Pritchard, Opt. Lett. **13,** 452 (1988); L. Marcassa, V. Bagnato, Y. Wang, C. Tsao, J. Weiner, O. Dulieu, Y. B. Band, and P. S. Julienne, Phys. Rev. A **47,** R4563 (1993).

[58] T. Walker, D. Sesko, and C. Wieman, Phys. Rev. Lett. **64,** 408 (1990); D. W. Sesko, T. G. Walker, and C. E. Wieman, J. Opt. Soc. Am. B **8,** 946 (1991).

[59] W. Ketterle, K. B. Davis, M. A. Joffe, A. Martin, and D. E. Pritchard, Phys. Rev. Lett. **70,** 2253 (1993).

[60] N. P. Bigelow and M. G. Prentiss, Phys. Rev. Lett. **65,** 29 (1990).

[61] P. L. Moulton, J. Opt. Soc. Am. B **3,** 125 (1986).

[62] J. L. Hall, L. Hollberg, T. Baer, and H. G. Robinson, Appl. Phys. Lett. **39,** 680 (1981).

[63] G. C. Bjorklund, Opt. Lett. **5,** 15 (1980).

[64] R. W. P. Drever, J. L. Hall, F. V. Kowalski, J. Hough, G. M. Ford, A. J. Munley, and H. Ward, Appl. Phys. B **31,** 97 (1983).

[65] R. J. Thompson, Ph.D. thesis, Univ. of Texas (1994) (unpublished).

[66] T. Bergeman, G. Erez, and H. J. Metcalf, Phys. Rev. A **35,** 1535 (1987).

[67] K. G. Libbrecht and J. L. Hall, Rev. Sci. Inst. **64,** 2133 (1993).

[68] Circulation of National Bureau of Standard 467, *Atomic Energy Levels*, Vol. 3.

[69] R. J. Cook and H. J. Kimble, Phys. Rev. Lett. **54,** 1023 (1985); H. J. Kimble, R. J. Cook and A. L. Wells, Phys. Rev. A **34,** 3190 (1986).

[70] K. Lindquist, M. Stephens, and C. Wieman, Phys. Rev. A **46,** 4082 (1992).

[71] *Metals Handbook*, Vol. 2, prepared by ASM International Handbook Committee.

[72] M. Succi, R. Canino, and B. Ferrario, Vaccum **35,** 579 (1985).

[73] J. P. Gordon and A. Ashkin, Phys. Rev. A **21,** 1606 (1980).

[74] J. Dalibard and C. Cohen-Tannoudji, J. Opt. Soc. Am. B **2,** 1707 (1985).

[75] B. R. Mollow, Phys. Rev. A **5,** 2217 (1972); B. R. Mollow, Phys. Rev. **188,** 1969 (1969).

[76] See, for example, C. Cohen-Tannoudji, J. Dupont-Roc, G. Grynberg, in *Atom-Photon Interactions*, John Wiley & Sons, Inc. 1992.

[77] R. W. Boyd, M. G. Raymer, P. Narum, and D. J. Harter, Phys. Rev. A **24,** 411 (1981); G. S. Agarwal, Phys. Rev. A **19,** 923 (1979).

[78] G. Khitrova, P. R. Berman and M. Sargent III, J. Opt. Soc. Am. B **5,** 160 (1988); M. Sargent III, D. A. Holm, and M. S. Zubairy, Phys. Rev. A **31,** 3112 (1985); S. Stenholm, D. A. Holm, and M. Sargent III, Phys. Rev. A **31,** 3124 (1985); D. A. Holm, M. Sargent III, and L. M. Hoffer, Phys. Rev. A **32,** 963 (1985); D. A. Holm, M. Sargent III, and S. Stenholm, J. Opt. Soc. Am. B **2,** 1456 (1985).

[79] M. L. Citron, H. R. Gray, C. W. Gabel, and C. R. Stroud Jr., Phys. Rev. A **16,** 1507 (1977); F. Y. Wu, S. Ezekiel, M. Ducloy, and B. R. Mollow, Phys. Rev. Lett. **38,** 1077 (1977); S. Haroche and F. Hartmann, Phys. Rev. A **6,** 1280 (1972).

[80] Y. Shevy, Phys. Rev. A **41,** 5229 (1990).

[81] A. D. Wilson-Gordon and H. Friedmann, Opt. Lett. **14,** 390 (1989).

[82] (a) P. R. Berman, D. G. Steel, G. Khitrova, and J. Liu, Phys. Rev. A **38,** 252 (1988); (b) P. R. Berman, Phys. Rev. A **43,** 1470 (1991).

[83] C. Cohen-Tannoudji and S. Reynaud, J. Phys. B **10,** 345 (1977); for its application to three-level systems, see also *ibid* 365 (1977); *ibid* 2311 (1977).

[84] D. Grison, B. Lounis, C. Salomon, J. Y. Courtois, and G. Grynberg, Europhys. Lett. **15,** 149 (1991).

[85] B. Gao, Phys. Rev. A **49,** 3391 (1994).

[86] L. M. Narducci, M. O. Scully, G. -L. Oppo, P. Ru, and J. R. Tredicce, Phys. Rev. A **42,** 1630 (1990); A. S. Manka, H. M. Doss, L. M. Narducci, P. Ru, and G. -L. Oppo, Phys. Rev. A **43,** 3748 (1991).

[87] J. Dalibard, Opt. Commun. **68,** 203 (1988).

[88] P. S. Jessen, C. Gerz, P. D. Lett, W. D. Phillips, S. L. Rolston, R. J. C. Spreeuw, and C. I. Westbrook, Phys. Rev. Lett. **69,** 49 (1992).

[89] P. Verkerk, B. Lounis, C. Salomon, C. Cohen-Tannoudji, J. Y. Courtois, and G. Grynberg, Phys. Rev. Lett. **68,** 3861 (1992); B. Lounis, P. Verkerk, J. Y. Courtois, C. Salomon, and G. Grynberg, Europhys. Lett. **21,** 13 (1993); G. Grynberg, B. Lounis, P. Verkerk, J. Y. Courtois, and C. Salomon, Phys. Rev. Lett. **70,** 2249 (1993).

[90] S. Reynaud, C. Fabre, E. Giacobino, and A. Heidmann, Phys. Rev. A **40,** 1440 (1989).

[91] R. M. Whitley and C. R. Stroud, Jr., Phys. Rev. A **14,** 1498 (1976); C. Cohen-Tannoudji and S. Reynaud, J. Phys. B **10,** 2311 (1977).

[92] M. O. Scully, S. Y. Zhu, and A. Gavrielides, Phys. Rev. Lett. **62,** 2813 (1989).

[93] M. G. Prentiss, N. P. Bigelow, M. S. Shahriar, and P. R. Hemmer, Opt. Lett. **16,** 1695 (1991).

[94] A. S. Parkins, P. Marte, P. Zoller, O. Carnal, and H. J. Kimble, Phys. Rev. A **51,** 1578 (1995).

[95] J. Javanainen, Phys. Rev. Lett. **64,** 519 (1990); N. P. Bigelow and M. Prentiss, Opt. Lett. **15,** 1479 (1990).

[96] M. Lax, Phys. Rev. **129,** 2342 (1963).

[97] S. H. Autler and C. H. Townes, Phys. Rev. **100,** 703 (1955).

[98] D. J. Gauthier, Y. Zhu, and T. W. Mossberg, Phys. Rev. Lett. **66,** 2460 (1991).

[99] G. Orriols, Nuovo Cimento **53B,** 1 (1979).

[100] K. Ellinger, J. Cooper, and P. Zoller, Phys. Rev. A **49,** 3909 (1994).

[101] N. Ph. Georgiades, private communication.

[102] *Cooperative Effects in Matter and Radiation*, eds. C. M. Bowden, D. W. Howgate, and H. R. Robl (Plenum Press, NY, 1977), and references therein.